ENGINEERED CELLULOSE NANOMATERIAL SYSTEMS FOR BIOMASS UPGRADING CATALYSIS

A Dissertation
Presented to
The Academic Faculty

by

Nathan Chase Ellebracht

In Partial Fulfillment
of the Requirements for the Degree
Doctor of Philosophy in the
School of Chemical & Biomolecular Engineering

Georgia Institute of Technology
August 2019

ENGINEERED CELLULOSE NANOMATERIAL SYSTEMS FOR BIOMASS UPGRADING CATALYSIS

Approved by:

Dr. Christopher W. Jones, Advisor
School of Chemical & Biomolecular Engineering
Georgia Institute of Technology

Dr. Meisha L. Shofner
School of Materials Science and Engineering
Georgia Institute of Technology

Dr. Elsa Reichmanis
School of Chemical & Biomolecular Engineering
Georgia Institute of Technology

Dr. Robert J. Moon
School of Materials Science and Engineering
Georgia Institute of Technology

Dr. J. Carson Meredith
School of Chemical & Biomolecular Engineering
Georgia Institute of Technology

Date Approved: May 15, 2019

To my loving and inspiring parents

ACKNOWLEDGMENTS

First and foremost, I must recognize the limitless support, bountiful opportunity, genuine encouragement, and never-ending inspiration from my parents, April and Ed. I'd also like to recognize that without the persistent challenge and drive born out of my life alongside my dear and competitive brother, Alex, I may not be where I am today.

I must thank my research advisor, Dr. Chris Jones, for his guidance and patient support. Throughout this journey, he encouraged and reinforced me as a scientist even in my times of greatest doubt. His trust and understanding, I do believe, come from a place far deeper than a Birkman pairwise evaluation (although data never hurt).

I am grateful to those who welcomed me into the cellulose/RBI communities. Dr. Robert Moon helped bring about CN@GT and the Student Committee and never hesitated to share a word of kind advice. Dr. Chris Luettgen is an inordinately kind and caring mentor, and he is where he should be, working with students. And of course, my surrogate group at anything Nano: Dr. Emily Cranston and the Crannies: Kevin, Steph, and Mike.

I'm nothing if not thorough, and I am obliged to acknowledge the great number of colleagues and friends have impacted my life through my PhD and made this wild journey what it is. Simon Pang for mentoring me as a scientist, being a shining example of a careful, curious, capable, and driven scientist, and for being my bike bud; Judy Xie for being far better an undergrad and friend than I ever could have hoped for; Eric Moschetta for his mentorship and endless discussions; Li-Chen Lee for her cheer that lifted everyone up; Caroline Hoyt for her own limitless positivity, groundedness, and sweet music; Taylor

Sulmonetti for giving me a home and my first meal in Atlanta, for dogs, and for just being a great guy; Chunjae Yoo for his abundant selflessness, remarkable handiness, and all-around capability; Michele Sarazen for her sharpness, balance, drive, inimitable thoughtfulness, and for bringing a little Berkeley with her to Atlanta; Miles Sakwa-Novak for being the global maximum of muscle times intelligence, but really for being a great example of scientific curiosity, how to ask the important questions, and demonstrating how to analyze data to extract real meaning; Adam Holewinski for his intellectual drive, microwaved enchiladas, neutron expertise, and persistent smirk; Akshay Korde for accepting the mantle of safety officer, listening to my pointless observations, and sharing his belVitas; Steph Didas for passing on the Berkeley desk, always keeping it cool, and holding the group together; Kong Wong for getting me through grad school and doing everything with me; Jason Lee (and Mark Conley) for sprints and much needed doses of chill; Jeff, Christine, Christa, and Mark (again) for loving food and board games; Alex Brittain for being a great friend who left too soon and for being the only one who understands what it is, truly, to love paper; and Thomas Kwok and Bailey Risteen for surviving RBI and everything related together.

Finally, I need to thank Eryn for helping me understand what really matters in life; my valued friends of old Dawei, Youngjun, Armaan, and Brandon for holding me to the highest standards, putting me in my place, and sticking together as we generally stumble through life; Raina for her support, keeping me dancing, and being a model of selflessness and hard work; Kavan, Ted, and Siddarth for getting me, keeping me sharp, and helping drive me to love science; and last, all the cats in my life, past and present, but most importantly my two Ms.

TABLE OF CONTENTS

LIST OF TABLES

acetone. Selectivity was evaluated after 4 h of reaction by ^{1}H NMR analysis of a crude mixture of the reaction products

LIST OF FIGURES

LIST OF SYMBOLS AND ABBREVIATIONS

3D	Three-dimensional
4NB	4-nitrobenzaldehyde
AC	Aldol condensation
AGU	Anhydroglucopyranose
APS	3-aminopropyltriethoxysilane
BET	Brunauer–Emmett–Teller
CBD	Cellulose binding domain
CMC	Carboxymethylcellulose
CNC	Cellulose nanocrystal
CNF	Cellulose nanofibril
CNM	Cellulose nanomaterial
DAP	1,3-diaminopropane
DI	De-ionized
DLS	Dynamic light scattering
DMB	1,4-dimethoxybenzene
DMSO	Dimethylsulfoxide
EA	Elemental analysis
EDA	Ethylenediamine
EDC	1-ethyl-3-(3-(dimethylamino)-propyl)carbodiimide hydrochloride
EtOAc	Ethyl acetate
EWG	Electron withdrawing group
FDU	Fudan University

FID	Flame ionization detector
FPL	Forest Products Laboratory
FTIR, FT–IR	Fourier transform infrared
Furf	Furfural
GC	Gas chromatography
HMDA	Hexamethylenediamine
HMF	Hydroxymethylfurfural
HT	Hydrothermal
LN2	Liquid nitrogen
MeCN	Acetonitrile
MFC	Microfibrillated cellulose
MNP	Metal nanoparticle
MOF	Metal organic framework
NHS	*n*-hydroxysuccinimide
NMR	Nuclear magnetic resonance
NMWL	Nominal molecular weight limit
NP	Nanoparticle
PEI	Poly(ethyleneimine)
PrA	Propylamine
SBA-15, SBA	Santa Barbara Amorphous (mesoporous silica)
SE	Sulfate half-ester
SEM	Scanning electron microscopy
STY	Site time yield
tBA	*tert*-butyl alcohol
TBSP	*t*-butyl 2-methyl-3-(triethoxysilyl)-propanoate

TEMPO	(2,2,6,6-tetramethylpiperidin-1-yl)-oxyl
TFA	Trifluoroacetic acid
TGA	Thermogravimetric analysis
TOCNF	TEMPO-oxidized cellulose nanofibril
TOMFC	TEMPO-oxidized microfibrillated cellulose
TPA	Terephthalaldehyde
UF	Ultrafiltration
UV	Ultraviolet
XDA	*p*-xylylenediamine
XRD	X-ray diffraction

SUMMARY

Cellulose nanomaterials (CNMs) are a class of advanced bioproducts being investigated in a range of scientific, commercial, and industrial applications. As the push for renewable and biodegradable bioderived materials grows, CNMs are well positioned to take hold as a new, high-value product of the forestry, pulp, and paper industries. They are the elementary building blocks of cellulose, which is the primary structural component of biomass and the most abundant biopolymer on earth. They exist and have remarkable uses in a nearly incomparable number of forms: as liquid crystals, hydrogels, foams, films, aerogels, and composite additives. The fibril-like structures, high specific strength, and hydroxyl-rich surfaces of these semi-crystalline nanomaterials afford them many of their unique properties. With such versatility, they have been investigated in a truly broad array of applications, including barriers, composites, industrial fluids, electronics, biomedical engineering, separations, sensing, and catalysis.

Studies of CNMs as catalyst supports have focused on supported metal nanoparticles and primarily in unstructured liquid suspensions. Limitations in thermal and chemical stability restrict the range of catalyst applications possible for CNMs, but their ability to form structured porous materials like aerogels and an expansive suite of chemical modifications offer unique opportunities in catalysis. Co-located organic acid and base surface species on heterogeneous supports, typically studied in silane-modified silicas, can function as enzyme-inspired cooperatively catalytic active sites. The overarching aim of this dissertation is to expand the capabilities of cellulose nanomaterials as catalysts,

specifically toward the field of heterogeneous organocatalysis, and to investigate potential advantages of alternative supports in this area.

The first chapter of this thesis provides detailed background into the motivation for this work and relevant scientific literature. The properties and form of cellulose nanomaterials are described, and the broad array of CNM functionalization methods to date are summarized. The formation of hydrogels and aerogels of or including CNMs is introduced, and a subset of the innumerable applications to which CNMs have been applied is detailed. This introduction documents at length the current applications of CNMs in catalysis and provides a healthy background to the field of heterogeneous organocatalysis.

The first research aim, presented in Chapter 2, is an initial demonstration of acid–base cooperative catalysis with functionalized CNMs, specifically cellulose nanocrystals. In this chapter, a rational multi-step chemical functionalization approach utilizing TEMPO-mediated oxidation and subsequent EDC amide coupling with alkyl diamines is developed. The surface chemistry of these materials is qualitatively and quantitatively characterized by FT–IR spectroscopy, conductometric titration, and elemental analysis. CNC acid–base catalysts are demonstrated as catalysts for the test aldol condensation reaction of 4-nitrobenzaldehyde and acetone, initially poorly in disadvantageous reaction solvents and then remarkably well with a new catalyst processing approach. Reaction rates are correlated with amine content, indicating that reactions are proceeding by the expected base-controlled mechanism. Finally, the size of the alkyl diamine is optimized, where shorter or longer functional groups are severely limited in catalysis by accessibility and cross-linking, respectively.

Chapter 3 details the second and most expansive research aim of this thesis. Building upon the initial catalyst design of Chapter 2, a rigorous study of each aspect of the CNC catalyst surface chemistry is performed. Sulfate half-esters, carboxylic acids, and primary amines are quantitatively varied and evaluated for their effects on aldol condensation catalysis. While sulfate half-esters are not beneficial, the catalytic activity is controlled by both the carboxylic acid and amine contents. Base site-specific activity is strongly correlated with acid/base ratio, indicating that cooperative acid availability influences active site function. This, along with a molecular level analysis of the CNC crystal structure and resulting spatial arrangement of surface functionality, contributed to a complete picture of the acid–base catalytic activity. These CNC catalysts were also utilized for upgrading aldol condensation reactions of biomass-derived furfural with good activity and selectivity. Finally, analogous state-of-the-art aminosilica catalysts were synthesized for direct comparison, and their activities and selectivities were surpassed by those of optimized CNCs.

The third research aim, found in Chapter 4, utilizes this acid–base functionalization framework to develop porous solid cellulose nanofibril aerogel catalysts. Chemical (oxidation) and mechanical (homogenization) methods are used to produce highly disperse CNFs from a microfibrillated cellulose feedstock. Acid–base CNF aerogels are produced by CNF modification with previously developed acid–base chemistry, networking by ice-templating, and cross-linking with small molecules prior to freeze-drying. These and polymer-cross-linked CNF aerogels are synthesized and tested. Suspension solvent strongly affects aerogel pore structure, and aerogels are found to be stable in organic solvents. Homogeneous and aerogel acid–base CNF catalysts are demonstrated as effective

catalysts for the aldol condensation but suffer from surface area and mass transfer limitations.

The thesis is concluded with a reiteration of the primary findings and suggestions for future research directions in Chapter 5. The knowledge gained from these studies with CNMs helps open new research directions and applications for this promising material class and provides an important perspective on the effects of order and proximity in supported organocatalysis.

CHAPTER 1. INTRODUCTION

1.1 Motivation and Inspiration

The development and progression of cellulose nanomaterials (CNMs), in many ways, have followed the trends one might expect from an exciting and "emergent" scientific technology.[1] Despite being a relatively old nanomaterial, as it was first reported in 1949,[2] within the research and academic world there has been a boom of publications since the early 2000s that has led to a truly impressive breadth of potential applications being investigated. What sets CNMs apart from other booming or previously "boomed" technologies like, for example, metal organic frameworks, graphene, carbon nanotubes, etc, is the unique intersection of cellulose nanomaterials as renewable, naturally produced materials with fascinating capabilities as truly high functioning advanced materials,[3,4] and which already physically exist within the massively scaled infrastructures of the forestry and pulp industries—it is just a matter of getting them out and, of course, finding someone to buy them.

Two of the more important factors which contributed to the notable delay in the boom of CNM research and development are the shifting markets within a generally mature and traditional pulp and paper industry,[5,6] coinciding with increased societal digitization, and the general self-awareness of oil and gas resource utilization and the related imbalance in the carbon cycle which has brought about significant investment into the idea of a biorefinery economy.[5,7–10] CNMs are a potentially high-value (relative) forest product which have may feasibly be produced at scale utilizing much of an existing infrastructure[11] and may serve as cheap, renewable, and biodegradable feedstocks for a variety of existing

advanced material applications as well as novel utilizations harnessing their unique properties.[12–16] Developing scaled production and applications of simpler products within the realm of the biorefinery, like CNMs, will help enable long term adaptation of more complex technologies such as complex fractionation of biomass components as chemical feedstocks.[8,17–20]

Cellulose nanomaterials are the elementary units of the hierarchical structure of cellulose, the primary structural component of biomass. These basic building blocks of cellulose are isolated from a bulk cellulose source, e.g. wood pulp, through mechanical and/or strong chemical treatment.[3] CNMs are low density, semi-crystalline materials which have, by definition, at least one nanoscale dimension (< 100 nm). Their structure and chemistry afford them a suite of impressive properties, including incredibly high specific strength, the ability to form flexible films for barrier applications or as substrates, unique rheological properties in liquid suspension, facile networking to form hydrogels and aerogels, and more. Many of their scaled applications directly take advantage of these properties for light-weighted composites, advanced barriers and packaging, and fluid properties in industrial and consumer products. As in any technological research boom, though, new applications and research directions have been demonstrated at a wild rate, including examples in electronics, biomedical engineering, separations, sensing, and catalysis.

The work presented in this thesis pushes the boundary in CNM applications by developing a new research direction for these materials: heterogeneous organocatalysis. This field of catalysis is itself younger than cellulose nanomaterials, primarily developing since the mid-2000s, and it seeks to expand the toolbox of catalysis at the intersection of

heterogeneous, homogeneous, and biocatalysis.[21,22] These enzyme-inspired solid catalyst materials incorporating complex organic active sites have almost uniquely been developed supported on inorganic silicates.[23] Interest in new CNM applications, their advantageous properties like chemical functionalizability and facile aerogel formation, and the basic similarity of hydroxyl-rich surface chemistry between silica and CNMs inspired this new research direction. As is not uncommonly the case with new research directions for CNMs, this fascinating material ultimately performed better than could have been expected but entirely not how we may have predicted.

1.2 Cellulose Nanomaterials

1.2.1 Production and Structure of Cellulose Nanomaterials

Cellulose nanomaterials may be derived from an array of biomass sources including woody and agricultural biomass, as well as bacteria and tunicate.[24,25] Generally, cellulose nanomaterials are classified into two categories: cellulose nanocrystals (CNCs) and cellulose nanofibrils (CNFs). Cellulose nanocrystals, the first CNM to be isolated and discovered,[2] are rod-like structures of linear cellulose polymers packed into highly stable and crystalline phases. CNCs have a very high aspect ratio and are typically 5–10 nm in width and 100–500 nm in length (Figure 1.1). The shape and crystal structure depends on the source.[3] CNCs are produced through strong acid hydrolysis of pretreated cellulose, typically with concentrated sulfuric acid, which dissolves the majority amorphous regions of cellulose leaving behind only the crystalline subunits. Once purified and isolated, CNCs form stable aqueous suspensions or gels that can be concentrated up to ~ 10 wt%.[3]

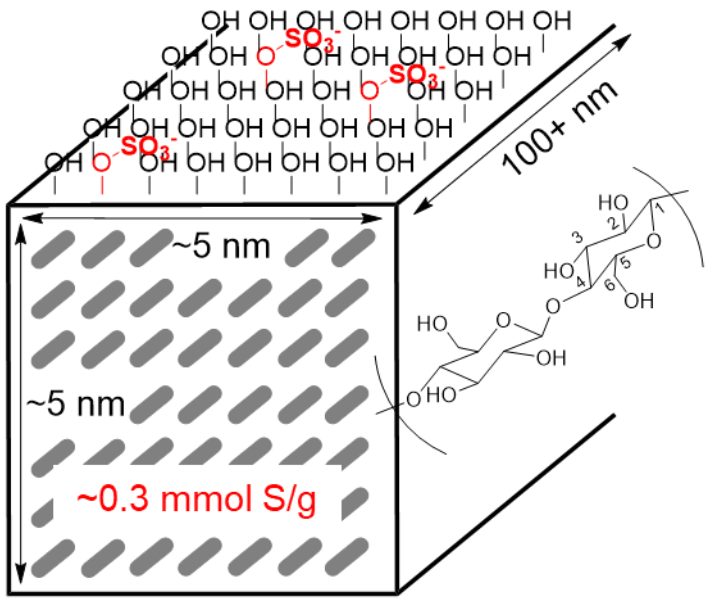

Figure 1.1 – Simplified schematic of a cross-section and surface chemistry of a cellulose nanocrystal produced by sulfuric acid hydrolysis.

In cellulose, these crystalline regions are bundled into larger fibrils held together by amorphous cellulose. These larger bundles are in turn packed into larger and larger fibril structures, ultimately forming large micron or millimeter scale fibers which are the characteristic components of paper. Cellulose nanofibrils, nominally discovered in 1983,[26] are bundled fibrils composed of amorphous and crystalline cellulose but whose widths are still in the nano-scale. CNFs are produced primarily with mechanical treatment, commonly in conjunction with some moderate chemical treatment. CNFs regularly have lengths up to 1 or more µm and have diameters 1–10 times those of CNCs, depending on the type of chemical and mechanical treatment and extent of delamination.[3,13,27] By avoiding the strong acid treatment and complicated processing required to produce CNCs, the manufacture of CNFs is typically more economical.[13]

CNFs are often produced through TEMPO-mediated oxidation of a cellulose source in conjunction with mechanical treatment. TEMPO-mediated oxidation is a cornerstone of CNM production and research—this moderated hypochlorite oxidation selectively carboxylates only one (C6) of the three free hydroxyl groups of the anhydroglucopyranose (AGU) monomer of cellulose. This chemical treatment, developed by Isogai and coworkers,[28] introduces a controlled degree of surface charge which greatly reduces the energy requires to fibrillate and disperse cellulose. The surface charge of TEMPO-oxidized CNFs or sulfuric acid-derived CNCs is necessary in order to maintain dispersed suspensions of these nanomaterials.[3,28] The pre-eminent problem with CNMs is their tendency to irreversibly agglomerate upon drying and difficulty in fully dispersing individual crystals or fibrils. TEMPO-mediated oxidation allows for facile dispersion of individualized nanofibrils with cross-sections of individual cellulose crystals but with flexibility afforded by lengths over 1 μm. In addition, the carboxylate chemistry introduced to the CNM surfaces by TEMPO oxidation opens up an array of functionalization chemistries, discussed further in the following section.[29,30]

While all forms of cellulose nanomaterials have been used in a broad array of applications, different types of CNMs may drastically differ in their properties and function. An additional grand challenge in the field of CNMs is the lack of uniformity across sources and production methods. Biomass source, chemical and mechanical treatment, processing, and storage affect the particle size distribution, dispersion, crystallinity, and chemistry of CNMs.[3] While some sources researchers in academia have used research-scale producers of CNMs like the Forest Products Laboratory to normalize materials, still many more produce their own CNMs from everything from filter paper to

microcrystalline cellulose to wood pulp. This lack of standardization is one of the major roadblocks to commercialization and scaled application.[11,31]

1.2.2 Chemical Functionalization of Cellulose Nanomaterials

Cellulose nanomaterials have hydroxyl-rich surface chemistry defined by the cellulose polymer building blocks of which they are composed. The AGU monomer of cellulose contains three free hydroxyl groups—termed C2, C3, and C6—which may be surface active and chemically accessible (Figure 1.1).[3,14] The crystal structure of cellulose Iβ, the native crystal structure of woody biomass, is such that either the C2 and C3 or just the C6 hydroxyl are oriented outward from and accessible on the CNM surface. Along a linear cellulose polymer, alternating monomers have the C2+C3 hydroxyls or the C6 hydroxyl exposed on the CNM surface.[14,29,30] This interesting structure, as well as differences in hydrogen bonding and reactivity of each of these hydroxyl groups, are key factors in understanding and manipulating CNM surface chemistry.

Surface functionalization of CNMs has most broadly been used to hydrophobized or increase compatibility of CNMs with polymers or other materials for composite applications.[16] However, the accessible hydroxyl functionality of CNMs has led to an incredible breadth of functionalization chemistries which have been investigated and widely reviewed. A non-exhaustive list of surface functionalization approaches includes etherification with epoxides, esterification with acid anhydrides, urethane modification with isocyanates, silane grafting by condensation, amide coupling with TEMPO-derived carboxylates, and more.[29,30,32,33]

Surface modification may be generally divided into three categories, any of which may utilize one or more of the chemical modification methods from this vast toolbox. These categories are high degree of substitution reactions with small molecules,[34,35] low degree of substitution reactions including grafting polymers or enzymes to or growing polymers from CNM surfaces,[36–38] and utilizing CNMs as a physical and chemical support for metal nanoparticles.[39–41] Functionalization can occur in liquid suspensions of CNMs or by gas-phase modification of dried CNM structures like aerogels or films. This versatile spectrum of chemical modifications is a central reason for which CNMs have been used in such diverse applications.

1.2.3 Cellulose Nanomaterials in Hydrogels and Aerogels

CNMs are not only advantageous from the perspective of chemical functionalizability, but by the types of structures and materials they can form. CNM films are one of these interesting forms, as they exhibit impressive barrier properties[42] and may be fully transparent, but film formation is not a particularly unique feature. As mentioned, CNMs may be well dispersed as individual crystals or fibers in liquid suspensions with, for example, appropriate surface charge, but they exhibit very strong physical interactions due to their hydrogen bonding when dried or agglomerated. This strong non-covalent bonding, along with the high aspect ratio and flexibility of especially CNFs, gives rise to CNMs' ability to readily form hydrogels and aerogels.[43]

Hydrogel networks form when CNMs are forced by some means to physically come into contact in suspension. Control of charged states by pH,[44] dissolved gases like CO_2,[45] incorporation of metal ions,[46] and other approaches can drive network formation by

reducing repulsive interactions which are requisite for stable dispersions. Simply forcing agglomeration itself will not lead to hydrogel formation, as hydrogelation requires a finely dispersed but interconnected network.[43] Cellulose nanocrystals, because of their shorter lengths and greater rigidity, form hydrogels less readily and require higher concentrations.[47] Chemical cross-linking with polymers[48] or small molecules[49,50] may also assist in the formation of stable CNM hydrogel networks.

Arguably the most common approach to hydrogel and network formation in cellulose nanomaterials is ice-templating by freezing.[43,51,52] As a suspension of CNMs is frozen, growing ice crystals force suspended particles together into smaller and smaller liquid pockets. Once frozen, the CNMs are forced into a physical network by exclusion from the ice crystals as they nucleate and grow. Freeze-thawing, where a suspension is frozen and then thawed, can produce stable hydrogel networks after the solvent has returned to the liquid phase.[52] The rate of freezing affects the extent of ice crystal nucleation, which in turn determines the networking and pore structure of ice-templated hydrogels.[53] Directional freezing can produce tunable anisotropic pore structures by controlling the direction of ice crystal growth.[54,55]

The usual purpose hydrogel formation in CNMs is to ultimately freeze-dry the resulting network. Freeze-drying and supercritical drying of CNM and dissolved cellulose suspensions have been widely utilized to form solid cellulose aerogels and foams.[43,56–58] Cellulose aerogels are ultra-lightweight (typically < 30 mg cm^{-3}), highly porous (often > 99.7%),[59–61] and have tunable structure,[55,62] surface area,[51,63] and mechanical properties.[64] The structure of the resulting aerogel depends heavily on factors such as the fiber size distribution, the suspension concentration, particle dispersion, solvent, and freezing rates.

Generally, suspensions of 0.1 to 4 wt% CNMs are freeze-dried from water, but the processing conditions and specifics vary greatly depending on the context and application. As with hydrogelation, CNC aerogels require higher concentrations to form the robust networks necessary to produce good aerogels. Poorly networked suspensions will constrict or collapse upon freeze-drying, whereas well-formed hydrogels will generally produce aerogels of the size and shape of the liquid suspension and hydrogel from which they were derived.

CNM suspensions of moderate concentration and dispersion will generally form highly porous honeycomb-like structures with thin walls of compressed CNM.[43] As mentioned, the structure depends directly on the means of network formation, and ice-templating from solvents other than water changes the resulting aerogel. Freeze-drying from *tert*-butyl alcohol and cosolvent mixtures with water can lead to smaller aerogel pore sizes.[51,65,66] A frequently desired property of CNM aerogels is reversible mechanical compressibility, which has been achieved in fibrillated[64] and crystalline[50] cellulose with fiber alignment and chemical cross-linking. Some aerogels are reversibly compressible under hydrated conditions, i.e. when swelled with a solvent, but not in dry conditions.[51] Without careful design, CNM aerogels will generally irreversibly collapse with mechanical compression.

1.2.4 Applications of Cellulose Nanomaterials

Cellulose nanomaterials have been utilized in a very wide variety of applications and in various physical forms. As homogeneous additives, CNCs have been used to increase the strength and therefore lightweight cement pastes[67] as well as a number of

polymers including poly(lactic acid), poly(caprolactone), poly(propylene), poly(styrene), poly(ethylene), poly(vinyl alcohol), poly(methyl methacrylate), and more.[16,68] As neat films or additives in polymer films for barrier applications, cellulose nanomaterials have been shown to have very low water and oxygen permeability.[42,69,70] Neat films of CNMs often suffer from poor mechanical properties, but incorporating a thin CNM layer on a more mechanically robust film[69] can greatly improve water and oxygen barrier properties while improving mechanical stability. Additionally, well-dispersed CNMs are transparent as neat films and may not add haze to polymer composite films. The combination of cellulose nanocrystals and chitin nanofibers films has been shown to greatly enhance barrier properties when spray-coated on poly(lactic acid) films.[71] CNM additives to bentonite- and mud-based drilling fluids for use in the oil and gas industry have improved rheological properties, filtration, and temperature stability at relatively low additive quantities.[72–74]

Beyond uses in films or as homogeneous additives, hydrogels and aerogels of or incorporating CNMs have a distinct but broad range of applications.[43,75,76] CNMs have shown promise as being broadly bio-compatible and non-toxic[77] which has led to investigations in many biomedical applications. CNM-strengthened hydrogels are attractive for drug delivery and wound healing materials given their bio-compatibility, high porosity, and tunable properties.[78,79] The scope of hydrogel applications is eclipsed by the versatility of aerogels as a functional and tunable porous solid substrate. Like hydrogels, aerogels have been broadly used in biomedical applications like tissue engineering and drug delivery.[76] CNM aerogels do not degrade under physiological conditions, retain their mechanical properties, are chemically stable, and can adhere and allow for the growth of

new cells and tissue. For example, CNM aerogels have been favorably compared to collagen meniscal implants and meniscus tissue harvested from pigs in terms of mechanical properties.[80]

CNM aerogels have also been used in electronics applications, for example having been demonstrated as supercapacitors by coating or incorporating MoS_2 and graphene oxide[81] or carbon nanotubes.[82] Hydrophobized CNM aerogels have been produced by functionalization with methyltrimethoxysilane,[83] diphenyl diisocyanates,[84] and other chemical modifications for efficient separations of oil and water. Encapsulation of metal organic framework (MOF) particles in aerogel networks[85,86] as well as cross-linking with poly(ethyleneimine)[87] have been used for separations of adsorptive separations of heavy metals like Cr(VI) and fluorescent dyes like Rhodamine B. Finally, suspensions and aerogels of metal-functionalized CNMs have been used in a variety of catalysis applications, which will be expanded upon in the following section.

1.3 Cellulose Nanomaterials in Catalysis Applications

Catalysis is a niche but expanding application area for cellulose nanomaterials. As briefly described in the earlier discussion of CNM functionalization, these materials have been used to support a variety of metal nanoparticles (MNPs) including Pd, Au, Ag, Ni, Ru, Pt, CuO, Fe_3O_4, CdS, TiO_2, and various bimetallic alloys.[88] CNMs were initially demonstrated in their ability to support MNPs in 2003 by Woodward and coworkers[89] for fuel cell applications, but it was not until the late 2000s that applications in catalysis began to take hold. Generally, metal precursors are reduced by an external reducing agent like $NaBH_4$ in homogeneous suspensions of CNMs, and the MNPs are preferentially stabilized

with the surface chemistry of CNMs. Often, TEMPO-oxidized CNMs are utilized as supports as the carboxylate surface chemistry assists in stabilizing the MNPs.[90,91] Highly disperse MNPs are readily supported in CNMs, in part due to the limiting size of the CNM particles themselves, and typically are ~ 5–20 nm in size.[88] Very high surface area (> 200 $nm^2\ g^{-1}$) and activity (TOF = 3168 h^{-1}) composite catalysts were achieved by coating CNCs in a melamine-formaldehyde porous polymer and dispersing Pd NPs in this network.[92] These various MNPs catalysts are commonly tested as catalysts with simple test reactions in homogeneous suspensions, often in water, like reduction, addition, and coupling reactions.[41,93,94]

Cellulose nanocrystals with monodisperse Pd NPs (~ 4 nm) were used as catalysts for the hydrogenation of phenol in water with H_2 and for the Heck coupling reaction of styrene and iodobenzene.[41] These highly disperse Pd NPs performed similarly or better than Pd supported on carbon or alumina. Amidoxime-functionalized bacterial cellulose supported Au nanoparticles between 10–30 nm, depending on mass loading, and was utilized for the most common test reaction of CNM catalysts—reduction of 4-nitrophenol.[93] A fluid column containing these bacterial cellulose catalysts was used for continuous reduction in flow and was showed stable activity for more than two months. Not before discussed in this introduction, CNC crystallites have a long-range slight chiral twist in their structure.[3] This chiral twist has been harnessed to achieve partial enantiomeric selectivity in CNC-supported Pd catalysts for the hydrogenation of prochiral ketones.[95] Enantiomeric catalytic selectivity was also demonstrated with cellulose-supported Rh NPs for asymmetric 1,4-addition addition reactions.[94]

These and other examples of CNM-supported MNP catalysts have generally shown versatility in metal support and good catalyst stability with minimal metal leaching. The test reactions with which these catalysts have been used are performed in liquid phase reaction mixtures. Homogeneously dispersed CNMs, while they may be effective catalyst supports such that they can support highly disperse metal nanoparticles, are not ideal candidates for heterogeneously catalyzed reactions. Other classical porous supports like carbons and aluminas may be easier to separate, more thermally stable, and have greater surface areas. The chiral nature of CNMs has been shown to induce partial enantiomeric selectivity, but this has not been demonstrated to the extent that would be industrially useful. Simply put, the scientific interest in CNMs in supporting metal catalysts generally surpasses their industrial relevance or feasibility. Still, their advantages in facile reduction, metal dispersion, biodegradability, water stability, and potentially low cost make them interesting substrates for catalysis.

Homogeneous CNMs may not look much like industrially relevant heterogeneous catalysts, which are typically highly porous solid particles. However, the highly porous aerogel structures readily formed by CNMs are potentially more industrially relevant as solid catalysts or functional materials. Despite the fairly significant number of CNM-supported metal catalyst publications, there are few examples of solid CNM aerogel catalysts. CNM aerogels as supports for metal particles were first demonstrated by Kuga and coworkers,[96] but they did not go as far as to demonstrate these materials as catalysts. Since then, a small array of studies has shown CNM aerogels as solid catalysts. Au nanoparticles were reduced on a CNM aerogel with $NaBH_4$, yielding a 192 $m^2\ g^{-1}$ aerogel catalyst with rod-like Au particles around 80 nm in length.[97] This catalyst was used for

room temperature styrene epoxidation with high activity and selectivity. CNFs were modified by Ag NPs via hydrothermal synthesis after non-covalent association of Ag precursors with unmodified CNF.[98] In this case, the Ag NPs (~ 30 nm) were produced before aerogel production through freeze-drying, unlike the Au catalyst above. These Ag-functionalized aerogels were used to sense and degrade organic dyes like Rhodamine B. An aerogel produced from dissolved cellulose cross-linked with a polyacrylamide was coated with CuS by a liquid phase synthesis with $CuCl_2$ and Na_2S. The hexagonal covellite CuS was used to photochemically degrade Methylene Blue, another organic dye.[99] Finally, a polydopamine- and silane-cross-linked CNF aerogel was used to support highly disperse (2.5 nm) Pd NPs. This relatively low surface area aerogel (10 m^2 g^{-1}) was used for the Suzuki and Heck cross-coupling reactions with high yields and recyclability.[100] These few examples represent a promising direction for CNMs as 3D-structured porous solid catalysts.

The overwhelming majority of CNMs as catalyst supports in literature are as substrates for metal catalysts. However, as detailed earlier, CNMs have highly functionalizable surfaces which may be chemically modified with a vast array of methods and chemistries. While some classic heterogeneous catalyst supports may have surface chemistries amenable to chemical functionalization, like silane grafting in silica,[101] the possibilities in chemical modification of CNMs is more broad. This allows for potential catalyst applications of CNMs which may be orthogonal to those possible with porous oxides or carbon. For example, tyrosinase enzymes were covalently immobilized onto paper substrates (chemically identical to CNMs) using a diamine and glutaraldehyde cross-

linking approach.[102] The supported enzyme showed improved activity for the degradation of phenols as compared to the homogeneous form.

The native or modified surface chemistries of CNMs and similar polysaccharide biomaterials have been utilized in several examples for their catalytic function. The hydroxyl and sulfate half-ester surface chemistry of CNCs has been demonstrated to have weak, non-specific hydrolytic function.[103,104] More intentionally, the carboxylic acid-decorated surface of TEMPO-oxidized CNFs was utilized as a heterogeneous acid catalyst for simple acetal hydrolysis.[105] Further work from this group used the acidic CNF in tandem with a homogeneous proline catalyst to perform acid–base cooperative aldol condensations of 4-nitrobenzaldehyde and acetone.[106] In these examples, chemically modified CNMs were utilized as simple acid catalysts, but these works relate to the possibility of more complex CNM modification for organocatalytic functionality.

1.4 Supported Organocatalysis

1.4.1 Homogeneous Organocatalysis

Organocatalysis is a remarkably young field, developing in the early 2000s, which investigates most generally any non-metal catalyst. This relatively new area of study gathers inspiration from the catalytic action of many enzymes, in which several (commonly three, referred to as a catalytic triad) amino acid moieties of various organic functionality work in unison to bind and catalyze a reaction of a particular substrate with exquisite specificity and selectivity.[107] Early organocatalysis studies emphasized the chirality of amine-containing small molecules to perform enantioselective addition reactions.[108] Similar to enzyme catalysis, many examples of organocatalysis utilized acids, bases, and

other hydrogen bonding chemistries to activate bonds and manipulate energetic states of reactive substrates. In homogeneous catalysis, however, acid and base chemistries readily quench, and replicating the multi-functional nature of enzyme active sites is challenging with small organic molecules. Proline, urea, and other small molecules which could exhibit multiple hydrogen bonding interactions with a substrate were initially promising in attempts to replicate the action of enzymes, but building additional complexity in synthesized small molecules is challenging (Figure 1.2).[21,108] In order to better replicate and carefully design a multi-functional organocatalytic system, researchers quickly moved to functionalize solid substrates.[21]

urea *L*-proline

Figure 1.2 – Urea and *L*-proline, early homogeneous organocatalysts.

1.4.2 History and Development of Heterogeneous Organocatalysis

The advent of heterogeneous organocatalytic systems came soon after in the mid-2000s, first described in 2005 by Lin and coworkers with aminosilane-functionalized mesoporous silica.[21] This demonstration utilized bifunctional weak acid and weak base silanes grafted to mesoporous silica, resulting in a heterogeneous catalyst surface decorated with randomly spaced acids and bases, pairs of which could cooperate not unlike homogeneous proline or real acid–base enzymes. Bifunctional acid–base catalysts based on silane-modified silicas exploded as a research topic, with a wide array of combinations of acidic and basic species being incorporated into catalytic materials. Multi-functional

silicas were utilized for cooperatively-catalyzed reactions as well as cascade reactions, where each type of grafted functional group performed a unique step in an overall reaction. By 2008, this burgeoning research area was initially reviewed,[22] with the most persistent challenge in the design of these materials—the spatial arrangement of multiple types of grafted functional groups—already at the fore of discussion. This field has continued to develop in terms of the complexity of materials synthesized as well as the understanding of reactions and mechanisms, with subsequent reviews in 2011[109] and 2016,[110] but there has yet to be real significant deviation from the initially utilized silica substrate.

1.4.3 Heterogeneous Organocatalytic Materials and Reactions

Silica-supported organocatalysts have primarily been synthesized and utilized for and and/or base catalysis.[109] The scope of reactions studied with this class of materials is limited by these chemistries, as especially base catalysis is the most promising type of catalysis to be performed uniquely well by organocatalytic functionality. A commonly implemented cascade test reaction is the acid-catalyzed deacetalization of a dimethoxyacetal to an aldehyde followed by a base-catalyzed reaction of the aldehyde such as the nitroaldol condensation (Henry reaction), Knoevenagel condensation, or aldol condensation reaction (Figure 1.3). Acid-catalyzed Michael addition reactions have also been widely used as test reactions.[109,110] While acid and base cascade reactions are feasible and interesting to evaluate with such bifunctional heterogeneous materials, their investigation is in reality a departure from the initial inspiration for these materials: cooperatively catalyzed enzyme-like reactions. I believe that a significant reasoning for the ample investigations of cascade reactions is related to the core design challenge in

synthesizing bifunctional silica materials, which is the spacing and arrangement of multiple types of functional groups.

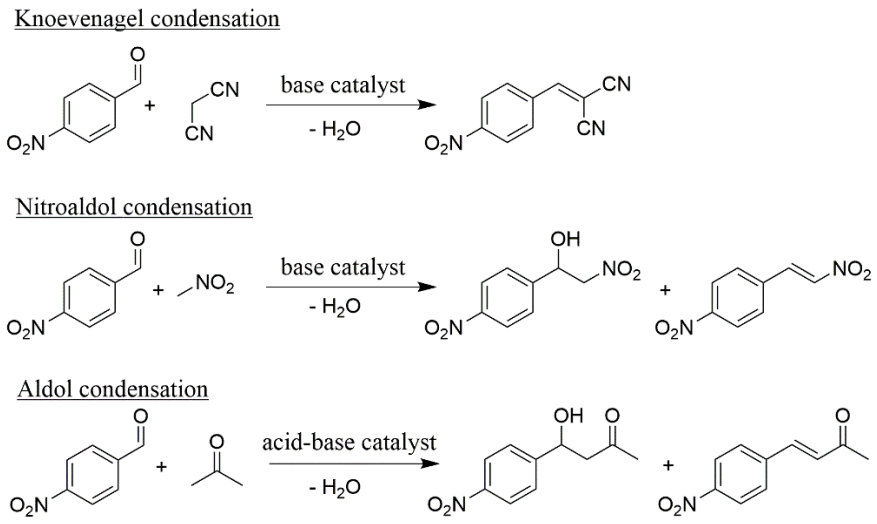

Figure 1.3 – Simplified reaction schemes for common test reactions of acid–base heterogeneous organocatalysts.

A variety of acid, base, and other functional groups have been incorporated into these modified silica materials. These are typically incorporated as organosilanes, which may be grafted onto silica post-synthetically or may be incorporated into the silica framework during synthesis through sol-gel or imprinting. Multifunctionality may be achieved by similar methods, but this opens up additional synthetic approaches. Multiple organosilanes may be co-grafted, sequentially grafted, co-condensed, etc.[109,111] Organic acid functionalities include sulfonic, phosphoric, and carboxylic acids.[111–116] Organic base functionalities are typically amine-based and may include chiral or achiral alkyl amines and are usually primary or secondary amines.[21,117–119] Brown and coworkers first grafted a chlorine-terminated silane to silica gels which was subsequently substituted with a protected proline group.[118] With subsequent deprotection, their proline-modified silicas (MCM-41 and silica gel) were active for the cooperatively-catalyzed aldol condensation

reaction. Silane-grafted primary and secondary amines have been compared in their catalytic function for the aldol condensation reaction. For aminosilica catalysts, primary amines were found to suffer from substrate inhibition by forming stable Schiff bases with the aldehyde reactant, which prevented their use for forming of the nucleophilic enamine intermediate with acetone.[117] Secondary amines, however, did not significantly form this Schiff base and had increased catalytic activity.

These two examples highlight the aldol condensation reaction, which is most commonly performed in test reactions with 4-nitrobenzaldehyde (4NB) and acetone. This reaction is of particular interest in this material class, because it has been shown to be advantageously catalyzed by the action of a cooperative acid–base site. This well-supported mechanism involves the formation of an enamine intermediate by the reaction of an amine with acetone, followed by the nucleophilic attack of the enamine on the α-carbon of an aldehyde activated by hydrogen bonding with a weak acid (Figure 1.4).[113,117,120] As mentioned earlier, many of the test reactions used to evaluate acid- and/or base-functionalized silica catalysts are catalyzed by an acid *or* a base, but the aldol condensation has a clearly demonstrated promotion by the cooperative action of a proximal acid–base pair.[120] For this reason, in the study of cooperative acid–base organocatalysts, it is a reaction of unique interest and is the primary test reaction used in this thesis for the evaluation of materials of this class.

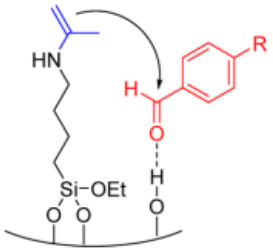

Figure 1.4 – Acid–base cooperatively-catalyzed C–C bond-forming step in aminopropyltriethoxysilane (APS)-functionalized silica organocatalysts.

The through-line in acid–base catalysts investigated for cooperative, not cascade, reactions is the challenge in achieving proximity in acid and base sites. This problem was acknowledged in the first paragraph of the initial publication in this field:[21]

> "Clearly, an important prerequisite for the construction of such a cooperative catalytic system would be the multi-functionalization of a solid support with *control of the relative concentrations and proper spatial arrangements between these functionalized groups.*"

The silica modification approaches of silane grafting and sol-gel synthesis have little to offer in terms of solutions to this challenge.[114,121] Even in mono-functional materials, problems with aminosilane clustering have been discovered even at low silane loadings.[122] Mono-functional materials may achieve good silane dispersion through the use of polar protic grafting solvents,[123] careful control of the silane condensation reaction by moisture control, and the use of bulky protecting groups.[111] Somewhat convoluted multi-step approaches have been attempted in efforts to yield effective relative spacing and positioning of multifunctional organocatalysts, but no direct means of control is achieved.[124–126] Co-grafting of acid and base species without careful control can lead to

site-poisoning acid–base quenching.[111] Importantly, the weakly Brønsted acidic silanols characteristic of silica support surfaces are remarkably effective weak acid cooperative partners for mono-functional aminosilica catalysts (Figure 1.4).[119,120,127] They hydrogen bond and activate aldehydes are in plentiful abundance, they but are not strong enough to poison amine functionality.[128]

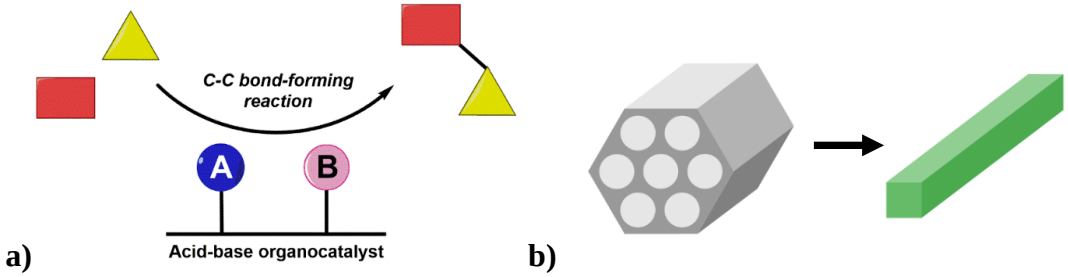

Figure 1.5 – (a) General design goal for acid–base organocatalysts for cooperatively-catalyzed reactions like the aldol condensation. (b) This thesis aims to utilize cellulose nanomaterials (right) as an alternative to the arguably over-studied mesoporous silica supports (left).

1.4.4 Organocatalyst Materials in Non-silica Supports

Although silica-supported catalysts have been the primary focus of organocatalysis literature, there are a number of examples of other material classes with similar function and design goals. Some porous polymers have been designed to incorporate catalyst function,[129] although many are designed as organometallic supports. Structured porous "FDU-type" polymers have been modified by H_2SO_4 treatment to incorporate sulfonic acid functional groups as acid catalysts for condensation and rearrangement reactions.[130] Linear poly(vinyl benzoic acid) polymer catalysts with carboxylic acid functionality were used to catalyst hydroboration reactions in octane.[131] Bifunctional amine and alcohol or carboxylic acid styrene-like block co-polymers were successfully demonstrated as cooperative acid–

base catalysts for the aldol condensation reaction, wherein polymers with balanced incorporation of acid and base sites were the most active.[132] This thesis aims to contribute a new support material to the field of acid–base organocatalysts, cellulose nanomaterials, by synthetically modifying surfaces to incorporate acid and base functionality (Figure 1.6).

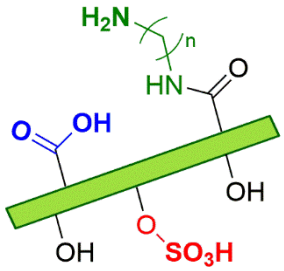

Figure 1.6 – Acid- and base-functionalized cellulose nanocrystal with hydroxyl, carboxylic acid, sulfate half-ester, and primary amine surface chemistry. CNM catalysts such as these are the focus of this thesis.

1.5 Transformations of Biomass-derived Furans

In addition to the utilization of cellulose nanomaterials, a renewable, cellulose-derived material, a minor focus of this thesis is in upgrading reactions of biomass-derived compounds. Generally, biomass may be converted into chemical feedstock molecules by three primary routes including pyrolysis to bio-oils, gasification to syngas, and hydrolysis to saccharide monomers.[133] The research focus of this thesis is organocatalysis, which is relevant to only the third route of biomass utilization, i.e. production and utilization of sugar monomers. Significant effort has been put forth in the processing and upgrading of sugar feedstocks toward high value or platform chemicals, but the high degree of oxygenation or sugars is a significant barrier to their conversion to feedstock chemicals, which are often minimally oxygenated hydrocarbons from petroleum resources.[8,134] Still,

the acid–base chemistries and mild conditions which apply to organocatalysts are relevant to a number of interesting transformations of biomass in this thrust.[135]

Furfural and hydroxymethylfurfural (HMF) are two platform molecules of interest. They are derived from C5 and C6 sugars, respectively, by acid-catalyzed reactions. Sulfonic acid-based heterogeneous organocatalysts have used to convert sugar monomers to furans,[136] like furfural and HMF, as well as to upgrade furans to larger carbon number intermediates by condensation reactions.[115] Only one example in literature has utilized basic heterogeneous organocatalysts in upgrading reactions. Slowing and coworkers performed a cascade reaction of furfuryl alcohol to furfural and subsequent aldol condensation products.[137] The application of organocatalyst materials to transformation of biomass-derived furans is understudied and could impart additional merit to a material class primarily studied with solely demonstrative test reactions (Figure 1.7).

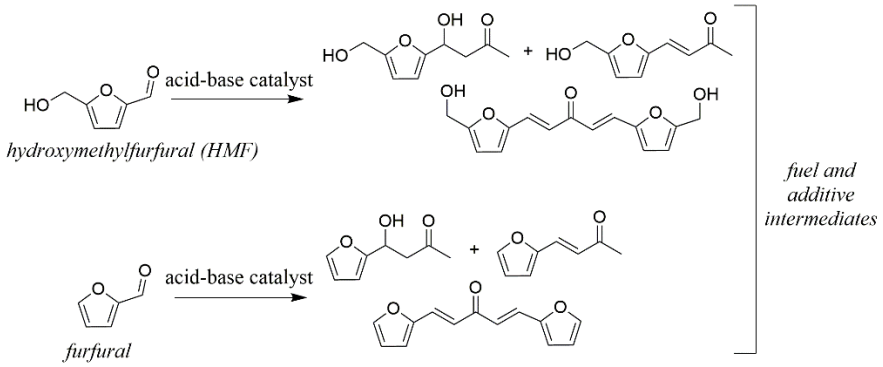

Figure 1.7 – Upgrading routes of HMF and furfural to higher carbon number intermediates of fuels and fuel additives through aldol condensation reactions with acetone.

1.6 Objectives and Impact

1.6.1 Thesis Outlook

Catalyst applications of cellulose nanomaterials have typically relied on supporting metal nanoparticles, an area that has been studied at extraordinary length utilizing long-standing and advantageous porous solid supports. While there are some benefits in this area afforded by the properties of cellulose nanomaterials like facile dispersion, solvent stability, and low leaching, the intersection between the vast knowledge of chemical functionalization of CNMs and the developing field of supported organocatalysis is notably vacant. By utilizing important lessons and understanding the limitations of silica- and polymer-supported organocatalysis, the remarkable chemical control possible with CNM modification may be exploited in the design of a new material class, both for cellulose nanomaterials and heterogeneous organocatalysts. The complex and precise design, which truly next-generation enzyme-inspired synthetic catalysts necessitate, may yet be achieved with cellulosic substrates instead of the nearly ubiquitously utilized silica supports in this field. These possibilities, coupled with the highly understudied field of catalytic CNM aerogels, define the broad goals of this thesis. The work presented herein aims to advance the understanding of cellulose nanomaterials as supports for cooperative organocatalysts, affect change in the limited material design paradigm of supported organocatalysis, and push forward the limited breadth of research into CNM aerogels as advanced catalyst substrates.

1.6.2 Chapter 2 – Acid–base Cooperative Catalyst Design in Cellulose Nanocrystals

This first research objective is to design a rational chemical modification scheme of cellulose nanocrystals to impart acid–base character to their surfaces for aldol condensation catalysis. This chapter lays out a rational synthetic approach based on an initial understanding of CNC surface chemistry and functionalization utilizing relatively simple and previously studied modification steps. A multi-step synthesis involving sulfate half-ester moderation, TEMPO-mediated oxidation, and amide coupling with diamines is developed. Key issues and practical matters like CNC catalyst handling, reaction conditions, and caveats in surface chemistry characterization are addressed. The goal is to lay the groundwork for synthesizing and utilizing this new support class of organocatalysis.

1.6.3 Chapter 3 – Highlighting Advantages of Cellulose Nanocrystals as a New Support Class for Cooperative Organocatalysis

With the synthetic and processing framework developed in Chapter 2, the second research objective is to understand the details of acid–base catalysis with cellulose nanocrystals utilizing this initial design as a starting point. Each aspect of the surface chemistry is probed by quantitatively varying surface species (sulfate half-esters, carboxylic acids, and primary amines). Final questions regarding surface chemistry, like diamine cross-linking, are investigated and addressed. This approach allows for a better picture of how to optimize surface functionalization for acid–base catalysis and which surface species do or do not contribute to catalytic function. The CNC catalysts are applied in an understudied approach to biomass valorization: aldol condensations of furfural with organic base catalysts. Finally, the detailed understanding of these catalysts is used to

compare to and critique the nominally state-of-the art supported organocatalysts based on amine-functionalized silica. A major goal of this chapter, beyond simply optimizing catalyst design, is to more broadly comment on the state of the aminosilica organocatalysis field and the limitations of this "default" catalyst support.

1.6.4 Chapter 4 – Development of Acid–base Cellulose Nanofibril Aerogel Catalysts

The objective of this final research chapter is to develop cellulose nanomaterial-based aerogel catalysts based on the knowledge of catalysis and functionalization established in the previous chapters. Cellulose nanocrystals, while ideal model supports, are inferior to cellulose nano*fibrils* (CNFs) in the production of aerogels. Having optimized the acid–base catalyst functionality in Chapter 3, the primary challenges confronted in this section relate to learning the art of CNM aerogel production and developing a processing approach from the larger-scale microfibrillated cellulose starting material to highly porous and well-defined aerogels. Various synthetic approaches with the goal of high surface area, chemically stable, and catalytically active are implemented. The defining questions addressed in this chapter are the interplay between CNF processing and chemical functionalization catalysis and cross-linking.

CHAPTER 2. DEVELOPMENT OF CELLULOSE NANOMATERIAL-BASED ACID–BASE ORGANOCATALYSTS

Chapter 2 and Appendix A are adapted from a published article. Reprinted by permission from Springer Nature: Springer Nature Cellulose 25: 6495, Amine Functionalization of Cellulose Nanocrystals for Acid–base Organocatalysis: Surface Chemistry, Cross-Linking, and Solvent Effects, Ellebracht, N.C. & Jones, C.W., Copyright 2018. https://doi.org/10.1007/s10570-018-2043-5.[138]

2.1 Introduction

The nature of enzyme catalysis, wherein a binding pocket with a highly specific shape and chemical environment may stabilize a substrate and where multiple carefully positioned amino acids perform a highly selective transformation, represents a lofty ideal in imagining catalysts with high degrees of selectivity and precise function. The field of heterogeneous organocatalysis borrows from this ideal in building, from the bottom up, enzyme-inspired catalysts with specific organic functionalities whose active sites often involve cooperative action of two or more chemical moieties.[21,139,140] To date, a significant portion of heterogeneous organocatalysts studied are supported on inorganic, often highly porous supports like mesoporous silicas. The hydroxyl-rich surfaces of silicas make for facile chemical functionalization through, e.g., silane grafting, by which catalyst active sites based on these grafted chemical species are formed. There is a significant body of work in imparting basic functionalities to silica supports, which, together with co-grafted acid groups or simply with the weakly acidic surface silanols from the support, are tested

for their catalytic function in acid-base catalyzed reactions like the aldol condensation.[22,23,111,121,141–143]

High specific surface areas and hydroxyl-rich surfaces are key characteristics of the silica materials used as catalyst supports. Nanocelluloses, including cellulose nanocrystals (CNCs), are a class of materials that share these key attributes, suggesting their potential as acid-base organocatalyst supports. CNCs, high aspect ratio rods of crystalline-packed linear cellulose polymers with dimensions of 3-10 nm by 100-500 nm, are derived from the most abundant biopolymer on the planet, cellulose, and may be produced from an array of biomass sources.[24,25] This class of materials has the potential to be produced at scale and at low cost and has been studied for innumerable applications due to its interesting properties including high specific strength, rheological behavior, high aspect ratio, high degree of crystallinity, chemically active surfaces, and the ability to form complex structures such as films, foams, hydrogels, and aerogels.[3,24,144–146]

Early industrial applications of nanocelluloses have taken advantage of the bulk and physical properties of CNCs, including uses in composites as a strong, light-weight additive, as rheological modifiers, and in barrier applications.[11,147,148] CNCs have the ability, however, to be a platform for a truly diverse suite of functional materials due to the structures they may form and their chemical functionalizability. There exist a plethora of functionalization chemistries that have been demonstrated for CNCs, widely reported and reviewed,[29,30,32,33] including high density, high degree of substitution reactions like oxidation and esterification with small molecules,[28,35,149] lower density modifications such as grafting large molecules like polymers or enzymes,[36,37] and support-type functionalization where, e.g., metal nanoparticles (MNPs) may be bound to and supported

on CNC surfaces.[39,41,90,93,94,150] The majority of examples of CNCs in catalysis applications to date have been as supports for reduced MNPs catalyzing various test reactions.[39,41,153,88,90,93–95,150–152] Examples include Pd for hydrogenation and Heck coupling reactions,[41] Au for reduction of 4-nitrophenol,[93] and Rh for asymmetric additions to enones and esters.[94] The chiral twist of CNCs has been shown to induce moderate enantiomeric selectivity in hydrogenation of prochiral ketones with Pd patches on CNCs[95] and in weak hydrolysis of amino acids with unmodified CNCs.[103]

Most examples of CNC-based catalysts typically utilize the surface chemistry, often acid functionality from oxidation, to support a catalytically active MNP or tether a macromolecule such as an enzyme, but do not directly utilize the surface for catalysis. Unmodified CNCs[103,104] and TEMPO-oxidized nanofibers[105] have some hydrolytic activity. Base catalysis has been demonstrated with chitin aerogels,[154] and oxidized nanofibers have used as acidic surfaces for combined heterogeneous-homogeneous aldol condensation reactions with homogeneous proline.[106] This study presents CNCs as an alternative support for bifunctional heterogeneous organocatalysis through direct chemical functionalization and utilization of acid and base surface chemistries in cooperative catalytic function. Relatively simple, mild chemical modifications in aqueous-only conditions were used to impart well-defined and appropriately dense surface functionalization. Selective TEMPO oxidation and subsequent amide coupling with diamines produced catalysts with active sites consisting of primary amines and proximal acid content from residual carboxylic acids or native sulfate ester groups. This is an initial demonstration of CNCs in bifunctional heterogeneous organocatalysis wherein the modified CNC surface is the catalyst active site. Acid-based catalyzed aldol condensation

reactions were performed under various reaction conditions, the kinetics of which were analyzed in the context of characterized CNC catalyst surfaces. Issues associated with undesired cross-linking, extents of functionalization, proximity of active sites, and accessibility of surface moieties are presented with insight based on surface species quantification, spectroscopic characterization, and catalytic activity.

2.2 Experimental Section

2.2.1 Materials and Chemicals

Cellulose nanocrystals (CNCs) produced by the Forest Products Laboratory (FPL) were obtained through the University of Maine in concentrated aqueous suspension (ca. 10 wt%). These were produced through concentrated sulfuric acid hydrolysis of wood pulp and contain ~0.9 wt% S. The CNC fibers are specified from the vendor to be 5–20 nm wide and 150–200 nm long. Solvents used include reverse osmosis deionized water as well as research grade acetone (>99%) and acetonitrile (>99%) from Sigma-Aldrich. N-hydroxysuccinimide (NHS, 98%), (2,2,6,6-Tetramethylpiperidin-1-yl)oxyl (TEMPO, 98%), and 1-ethyl-3-(3-dimethylaminopropyl)carbodiimide hydrochloride (EDC, >99%) were purchased from Sigma-Aldrich. Sodium hypochlorite (11-15% available chlorine) was obtained from Alfa Aesar. Alkyl amines used in amide coupling functionalization reactions were obtained from various vendors: ethylenediamine (EDA, 99%), 1,3-diaminopropane (DAP, >99%), and hexamethylenediamine (HMDA, 98%) were purchased from Sigma-Aldrich and propylamine (PrA, >99%) from Acros Organics. For catalysis experiments, 4-nitrobenzaldehyde (4-NB, 98%) from Sigma-Aldrich and 1,4-dimethoxybenzene (DMB, >99%) from TCI were used.

2.2.2 CNC Purification and Storage

Stock CNCs and functionalized CNC samples were stored at 4 °C in aqueous suspension. After each functionalization step, CNCs were purified by dialysis with 3,500 MWCO dialysis tubing against a total volume of deionized (DI) water approximately 300 times that of the suspension being purified or until dialysate pH and conductivity stabilized. In some cases, a Millipore solvent-resistant ultrafiltration cell with 1 kDa NMWL regenerated cellulose UF discs was used to purify and concentrate large volume suspensions of CNCs. The CNC mass fractions of purified and recovered CNC suspensions were determined gravimetrically by freeze-drying known quantities of the aqueous suspensions for 48 h in a Labconco FreeZone lyophilizer. Freeze-dried CNC samples were only used for characterization and wt% determination.

2.2.3 Chemical Functionalization of CNCs

Partial (~50% removal) desulfation of stock CNCs was performed by weak acid hydrolysis with dilute HCl. CNCs were diluted and HCl (aq) was added to achieve a suspension with ~0.5 wt% CNC and 0.05 M HCl. The acidified CNC suspension was magnetically stirred at 80 °C for 24 h, after which it was partially neutralized to pH 3–4 with a NaOH solution. The mixture was purified and concentrated to 2–3 wt% by ultrafiltration.

TEMPO-mediated oxidation procedures were adapted from multiple sources [28,37,155,156] to selectively oxidize accessible C6 hydroxyl groups on the CNC surfaces. Suspensions of either stock or partially desulfated CNCs were diluted to approximately 2 wt%. All following reagent quantities are reported per dry gram of CNC. TEMPO (0.1 g)

was added and allowed to dissolve with magnetic stirring. To this stirred suspension, 1 g of NaBr was added followed by a volume of NaClO solution containing 1.9 g NaClO. Monitored with a pH meter, the pH was adjusted dropwise with 1 N NaOH to between 10 and 11. The opaque orange suspension was stirred at room temperature for 4 h, during which the pH slowly fell and was readjusted to 10–11 several times. To recover the oxidized CNCs, 6 g NaCl was added to flocculate the suspension. The suspension was divided and washed, via centrifugation, decanting, and resuspension, three times with 0.5 M NaCl, twice with 0.1 M HCl to protonate the carboxylic acids, and then resuspended in DI water and dialyzed.

Various small alkyl amines and diamines were coupled to oxidized CNCs under mild conditions via aqueous EDC amide coupling (Figure 2.1). Amide coupling conditions were adapted from various publications.[36,37,44,157] Five molar equivalents of the amine or diamine, relative to available carboxylic acid groups determined by conductometric titration, were added to a stirred 1–2 wt% suspension of oxidized CNCs. Depending on the quantity and base strength of the amine molecules added, the pH of the suspension increased to between 9 and 11. To this mixture, 1.5 equivalents of 1-ethyl-3-(3-dimethylaminopropyl)carbodiimide hydrochloride (EDC) and *n*-hydroxysuccinimide (NHS), dissolved in <1 mL DI H_2O, were added. The pH was then adjusted with 1 N HCl to between 7.5 and 8, and the suspension was sealed and stirred overnight at room temperature. The suspension was then thoroughly dialyzed against DI H_2O to recover the amide-coupled CNCs. Sample naming conventions are as follows: DS50 denotes samples which were initially partially desulfated; COOH refers to oxidized samples prior to amide

coupling; DAP, EDA, HMDA, PrA refer to samples which have been functionalized via amide coupling with the denoted amine molecule.

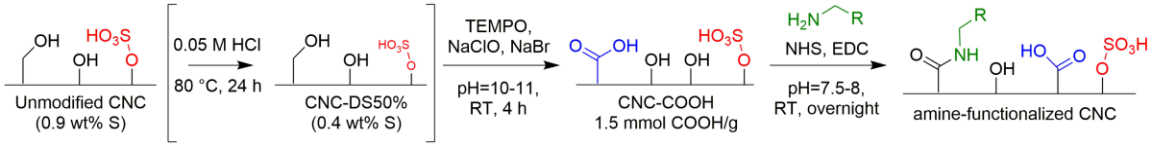

Figure 2.1 – Chemical functionalization scheme for amine-functionalization of cellulose nanocrystals. Each step was performed in aqueous suspension under the conditions described. *R* typically consists of additional alkyl spacing and a pendant primary amine.

2.2.4 Conductometric and pH Titrations

Titrations of CNCs were performed with simultaneous measurement of solution conductivity and pH with a Hanna Instruments benchtop meter. Suspensions of 50 to 100 mg (dry) oxidized CNCs were diluted to 70–100 mL in DI H_2O. The suspensions were brought to just under pH 3 and ~100 µS/cm with small volumes of ~0.5 N HCl (aq). Acidified dilute solutions were stirred and bubbled with N_2 for at least 30 minutes to remove trace dissolved CO_2, present in solution as carbonic acid. Suspensions were subsequently titrated with 0.100 N NaOH to pH >10 while pH and conductivity were monitored and recorded with titrant addition. Reduced volumes were used for titrant additions from pH 4 to 8 during titration of the surface carboxylic acid groups.

2.2.5 Fourier Transform-Infrared Spectroscopy

Fourier transform-infrared (FTIR) transmission spectra were collected under vacuum with a Bruker Vertex 80v FTIR bench. Modified CNC samples were freeze-dried from their neutral, purified form and a few milligrams of each dried sample were ground with 120 mg KBr and pressed into a pellet for transmission measurements. The resulting

spectra were baseline corrected and normalized to the symmetric C–H vibrations at 2900 cm^{-1}.

2.2.6 Elemental Analysis

Combustion elemental analysis for C, H, N, and S content was performed by Atlantic Microlab, Inc. for all freeze-dried samples. After receipt and before analysis, samples were dried by Atlantic under vacuum at 80 °C for 3 h to remove weakly adsorbed ambient water vapor.

2.2.7 Dynamic Light Scattering

Multi-angle DLS experiments for CNC particle size and cross-linking analysis were performed with a custom apparatus using a 688 nm laser light source and an ALV-5000/E digital autocorrelator. Samples for measurement were prepared by dilution to 0.1 wt% or less in DI H_2O and filtration of ~2 mL of the suspension through a 0.22 μm Millipore syringe filter. Light scattering measurements were taken at seven scattering angles (30, 45, 60, 75, 90, 105, 120 °) and the hydrodynamic radii were calculated using a third order cumulant fit of the scattering intensity autocorrelation function.

2.2.8 Catalyzed Aldol Condensation Reactions

Functionalized CNCs were tested for their activity as acid-base catalysts for the aldol condensation of 4-nitrobenzaldehyde with acetone (Figure 2.2). Reactions were carried out in liquid phase with an excess of acetone, which functioned as a co-solvent for the reaction mixtures. CNC catalysts were dispersed in reaction solutions as heterogeneous catalysts, with reactions occurring at their functionalized surfaces. Two approaches to CNC

catalyst processing were used for reaction set-up, one for reactions in water and acetone mixtures and one for acetonitrile (MeCN) and acetone mixtures.

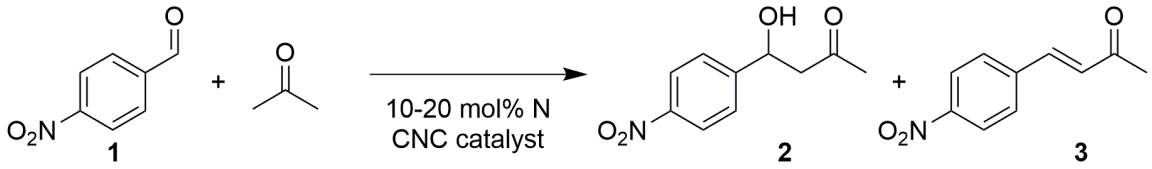

Figure 2.2 – The aldol condensation of 4-nitrobenzaldehyde (4-NB, *1*) with acetone, used as a co-solvent and a reactant in excess. *2* and *3* are the major products formed, however other products including the crossed-aldol adduct of two 4-NB molecules linked by one acetone are formed at low yields.

For water/acetone reaction mixtures, a weighed quantity of a CNC sample in aqueous suspension containing the desired mass of catalyst was combined with 0.5 mL acetone and a small volume of DI H_2O in a 25 mL 2-neck round bottom flask with a magnetic stir bar. If necessary, some aqueous CNC sample solutions were concentrated slightly by evaporation, with stirring at no more than 50 °C, to achieve the required CNC catalyst mass in the desired volume of water. One neck of the reaction flask was attached to a Graham condenser sealed with a rubber septum, and the second neck was also sealed with a rubber septum, through which reaction aliquots were taken. To this pre-reaction catalyst suspension, 1 mL of a stock solution containing 100 mM of 4-nitrobenzaldehyde (4NB, reactant) and 1,4-dimethoxybenzene (DMB, used as an internal standard) was added by syringe, such that the final reaction mixture was 4 mL total and contained 3:5 by volume DI H_2O:acetone as co-solvents. The initial reaction mixture as assembled contained 25 mM 4NB and DMB, 10 or 20 mol% CNC catalyst, and the water/acetone co-solvents. Catalyst mol% was calculated with the standard definition for similar base-containing organocatalyst systems as the ratio of total amine molecules present on the active surfaces to the initial 4NB in the reaction solution. A balloon with a small pressure of N_2 was

attached via needle through the septum atop the condenser to allow for additional headspace for solvent vapor during reactions at elevated temperatures and to prevent over-pressurization. Once assembled, the flask was immersed in an oil bath at 80 °C to begin the reaction. Aliquots of ~50 µL were taken by needle and syringe from the reaction mixture to be analyzed by FID with a Shimadzu 2010 Gas Chromatograph. The initial aliquot was taken from the assembled reaction mixture with stirring prior to temperature elevation, and subsequent aliquots were taken over a 48 h period at 30 min (initial) or 1 h intervals in three time blocks. Reaction aliquots were filtered through a 1–2 cm plug of silica to remove suspended CNC catalyst and then diluted in acetone for GC analysis.

For reactions in non-aqueous mixtures, the second processing approach mentioned above, a solvent exchange was necessary. Generally, a weighed quantity of a dilute aqueous CNC catalyst solution (typically <5 g) was dialyzed against 800 mL of a 50:50 (by volume) mixture of acetonitrile and acetone overnight. The resulting gel with some added solvent were transferred to a centrifuge tube via bulb pipette and spatula. The gel was washed with 50:50 MeCN:acetone twice by centrifuging and decanting and then transferred as a 2 mL mixture with these co-solvents to a round bottom flask as described above. Small CNC gels were transferred with care and to prevent any catalyst losses. As before, the 2-neck reaction flask was fit with a rubber septum and a sealed Graham condenser with a N_2 balloon. The 2 mL CNC, MeCN, and acetone mixture was stirred and immersed in an oil bath at 60 °C and allowed to redisperse at reaction temperature. To this pre-reaction mixture, 2 mL of a 100 mM stock solution of 4-NB and DMB in 50:50 MeCN:acetone was added by syringe. The initial reaction aliquot was taken just after addition of the reactant and internal standard solution, and timepoints were taken as

described above every 30 min for 2 h and subsequently every hour over the 5 h reaction period. The CNC catalyst formed a homogeneous but partially opaque dispersion in the non-aqueous reaction mixture with stirring and heating. The major products formed (**2** and **3**) were isolated by column chromatography, and product selectivities and yields were determined by ^{1}H NMR analysis as described in the supporting information (Table A-1 – Table A-2, Figure A.2 – Figure A.5).

2.3 Results and Discussion

2.3.1 Surface Functionalization of CNCs

A thorough understanding of CNCs as heterogeneous organocatalytic materials requires a well-defined description of their surface chemistry and geometry. Precise determinations of the chemical content and orientation of exposed anhydroglucose units (AGU) of CNC surfaces are available from numerous techniques and studies, but analysis presented herein is based on descriptions from literature.[30,158] The relevant quantitative descriptors, calculated based on crystallographic analysis of the unit cell of packed cellulose chains, are the mass- and surface area- specific densities of the three types of AGU hydroxyl groups. Based on the cross-section width of the FPL CNCs used and the crystallographic structure, the total accessible surface hydroxyl groups is estimated to be 4.3 mmol OH per gram CNC or 5.3 OH per nm^2 CNC surface area. This calculation does not consider the chemistry of either end of the CNC fibers, given the high aspect ratio of these materials, and only describes the surface area along the fiber length. The orientation of the AGU monomers is such that, along a linear polymer chain, the accessible hydroxyl groups per monomer alternate between C2+C3 and C6, for an average of 1.5 OH per AGU.

The hydroxyl density is of importance both in understanding the extent of surface functionalization and in comparison to other heterogeneous acid-base organocatalyst materials.[21–23,111,121,141,142,159] Representative silica supports for organocatalytic moieties, such as mesoporous SBA-15, have silanol densities in the range of 1 to 5 OH per nm^2, quite comparable to the –OH density found on CNC surfaces.

The chemical functionalization approach was designed to achieve geometrically and chemically well-defined active surfaces. The desired catalyst active site for the heterogeneous acid-base catalyzed aldol condensation reaction, as studied in previous works, consists of a nucleophilic base and a proximal weak acid site. The functionalization route begins with the selective TEMPO oxidation of the regularly spaced surface C6 hydroxyl groups, and the resulting carboxylic acid groups were used as attachment points for base-modification through amide coupling reactions with small alkyl diamines. The reactions are performed in aqueous suspensions and do not require complex processing or extreme conditions, preventing CNC degradation and maintaining good dispersion, such that CNC surfaces are highly accessible and high degrees of functionalization are achieved.

Multiple potential catalytically cooperative weak acids exist on the functional CNC surfaces, namely surface hydroxyl groups (primarily C2 and C3 post-oxidation), residual free carboxylic acids, and sulfate esters originating from the H_2SO_4 hydrolysis used to produce the CNCs. To investigate the effect of these sulfate esters on catalyst performance, weak acid hydrolytic partial desulfation before hydroxyl oxidation was used to produce samples with reduced S content. The initial sulfate ester content of purchased FPL CNCs and the extent of desulfation were determined by combustion elemental analysis. The partial desulfation performed with a low concentration of HCl and elevated temperature

removed approximately 50% of the pendant sulfate esters, returning those surface sites to their original hydroxyl form. As desulfation proceeded, the suspension of CNCs became more viscous and somewhat opaque as some flocculation occurred with the decrease in surface charge with sulfate ester removal and an increase of the ionic strength of the suspension with the release of sulfate ions. During subsequent oxidation and amide coupling steps, the total sulfate ester content of CNC samples decreased slightly as more were partially removed. The S content of stock, partially desulfated, and fully functionalized CNC samples are shown in Table 2-1. The stock CNCs had an initial S content of 0.9 wt%, corresponding to 0.28 mmol S/g_{CNC} or mmol $–OSO_3^-/g_{CNC.}$ This is about one sulfate ester group per 10 surface AGU, a relatively small loading compared to the yield of selective TEMPO oxidation, which can yield one –COOH per three total initial surface hydroxyls or per two AGU.

Both stock CNCs and partially desulfated CNCs were selectively oxidized as described in the methods. After recovery and purification, the degree of oxidation was determined through conductometric titration of the oxidized materials (Table 2-1). The total carboxylic acid content was determined by a standard method of analysis, wherein the linear pre- (negative slope) and post- (positive slope) acid titration regions, as well as the period of approximately constant conductivity, were fit with linear regression. The difference in mmol titrant added between the two points of intersection with the approximately constant conductivity line is equivalent to the total quantity of –COOH present on the CNCs. For both stock CNCs and partially desulfated CNCs, approximately complete selective oxidation of the C6 primary hydroxyl groups to –COOH was achieved

as the degrees of oxidation match well with the calculated theoretical quantity of these C6 hydroxyl groups (1.4–1.5 mmol/g_{CNC}).

The final functionalization step was aqueous EDC/NHS amide coupling, which was performed with several diamine molecules, namely DAP (3 C), EDA (2 C), HMDA (6 C), and one monoamine, PrA (3 C; Figure 2.1). DAP materials were synthesized from both full and reduced sulfate ester content samples, while EDA-, HMDA-, and PrA-coupled materials were only synthesized from reduced sulfur starting materials. DAP was chosen as the primary catalyst material based on previous organocatalysis work on mesoporous silicas, where a minimum of three carbon alkyl spacing from surface attachment to active base moiety was required for the necessary flexibility and length to achieve full acid-base cooperativity.[143] Combustion elemental analysis was used to determine, in particular, the total amount of diamine molecules successfully coupled via amide bonds to the CNC surfaces (Table 2-1), as well as the ultimate sulfate ester contents, while FTIR spectra were analyzed to qualitatively confirm the chemical species present after each step. SEM images of functionalized CNCs are shown in Figure A.7.

Table 2-1 – Chemical functionalization results of multi-step CNC functionalization

	$-SO_3^-$ (mmol/g)[a]	**COOH (mmol/g)[b]**	**Coupled Amine Molecules (mmol/g)[a]**	**DS**
CNC-FPL	0.28	-	-	-
CNC-DS50	0.12	-	-	-
CNC-COOH	0.19	1.5	-	-
CNC-DS50-COOH	0.11	1.5	-	-
CNC-DAP	0.18	*0.61*	0.89	0.31
CNC-DS50-DAP	0.094	*0.65*	0.85	0.30
CNC-DS50-EDA	0.11	*0.52*	0.98	0.34
CNC-DS50-HMDA	0.12	*0.63*	0.87	0.30
CNC-DS50-PrA	0.10	*0.04*	1.5	0.51

Sulfate ester content and amine loading are calculated assuming all S and N present are attributable to these functional moieties. Italicized COOH loadings in post-amide coupling materials are upper bounds for residual carboxylic acid content due to the possibility of cross-linking
[a]Sulfate ester and coupled amine molecule loadings determined by combustion elemental analysis
[b]COOH loading determined by conductometric titration (theoretical C6 groups: ~1.5 mmol/g). Residual COOH content of amide-coupled materials (italicized) is calculated assuming one amine or diamine molecule consumes one carboxylic acid to form an amide.

2.3.2 Spectroscopic and DLS Analysis of Functionalization and Cross-linking

Amide coupling reactions performed with small alkyl diamines (DAP, EDA, HMDA) all resulted in very similar loadings of amine molecules (Table 2-1). A theoretical maximum loading based on the reaction scheme and the degree of oxidation, assuming each diamine forms one amide bond with a surface –COOH, would be equivalent to the initial COOH loadings of 1.5 mmol/g. The amine loading was determined by elemental analysis, which yields only an absolute N content and has no information about the nature of the bonds formed. A resulting unknown from this approach is the possibility and extent of cross-linking that may have occurred, in which a diamine molecule forms two amide bonds with surface acids, either between two sites on the same CNC surface (intra-fiber) or forming a bridge between two distinct CNCs (inter-fiber). The residual acid content post-oxidation proved difficult to quantify, as the increased complexity of the conductometric titration given the numerous charged surface species and potential ion pairs hindered accurate potentiometric titration analysis. The extent of cross-linking is particularly important for understanding the catalytic activity of these materials, as the proposed active catalyst site involves a nucleophilic free amine, and cross-linked molecules reduce the number of available primary amines as well as decrease the quantity of residual carboxylic acid sites.

Chemical functionalization was qualitatively tracked by FTIR spectroscopy of CNC samples freeze-dried from aqueous suspensions unaltered after purification. Ion exchange was not utilized prior to lyophilization and characterization, resulting in some mixed charged states and potential non-covalent interactions of surface species. The major IR region of interest used to track chemical modification is from 1500–1800 cm^{-1}, as seen in Figure 2, which includes information about carbonyl species like acids and amides, water, and amines. In this region, native FPL and partially desulfated CNCs have a single peak around 1635–1640 cm^{-1}, attributed to adsorbed water.[36,158] Freeze-dried samples, handled under ambient conditions, will rapidly re-adsorb water such that this peak will be present in all samples. In general, the FTIR spectra for corresponding materials synthesized from as-received FPL and partially desulfated CNCs are nearly identical, indicating that partial desulfation does not noticeably affect the functionalization chemistry beyond minor differences in degree of substitution. Partially desulfated samples show a very minor decrease in a peak around 810 cm^{-1}, attributed to the C-O-S bond of sulfate ester groups.[160] All samples have low sulfur content, <1 wt%, and as such associated IR traces are generally insignificant but can be seen in the full IR spectra available in the supporting information (Figure A.6).

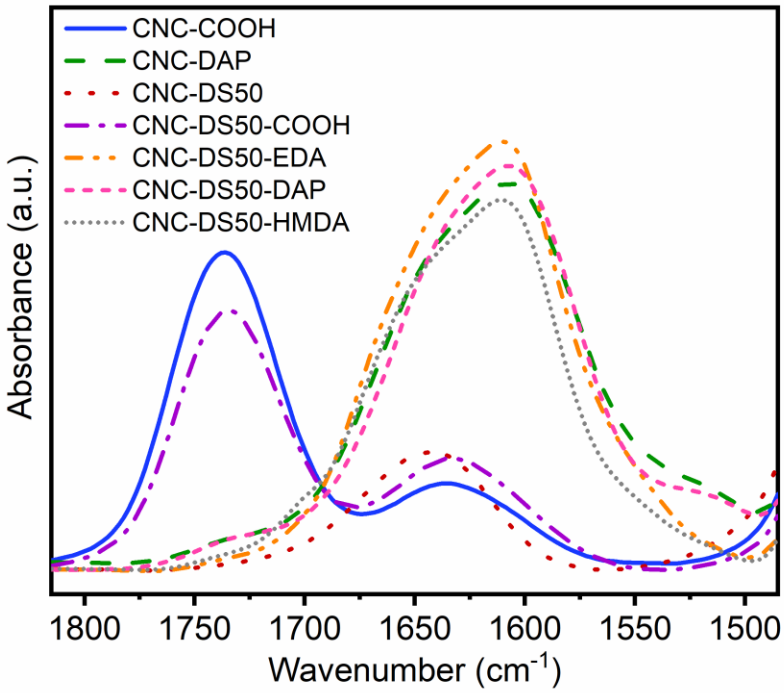

Figure 2.3 – FTIR spectra for functionalized CNC materials in the region of interest for C=O functional IR modes and others related to the surface functionalization like amine bending and adsorbed water. Similar bonding is found in all amide-coupled materials.

TEMPO-mediated oxidation of CNCs and the formation of carboxylic acid species result in a strong C=O IR stretch around 1735–1740 cm^{-1}, associated with the acid form –COOH.[28,36,158] During post-oxidation purification, CNCs are washed with dilute HCl before dialysis, which yields primarily acid form carboxylic acids. Adsorbed water is also present as before. The subsequent amide coupling step introduces multiple new IR modes in the sample spectra and greatly reduces the COOH C=O stretch. This disappearance is primarily attributed to the conversion of surface acids to amides, however it is not an indication of complete disappearance; the post-coupling samples retain residual carboxylic acid functionality, but they are in the COO^- state and are associated with a sodium ion or a proximal charged amine functionality. The COO^- C=O stretch is among several overlapping modes from 1550–1700 cm^{-1}, specifically found around 1605 cm^{-1}. By

acidifying the aqueous suspension of amide-coupled samples, a significant increase in the strong COOH C=O stretch is seen, indicative of residual carboxylic acids. Other peaks present in diamine-functionalized samples include the amide I C=O stretch at 1655–1665 cm^{-1}, N–H bending of free primary amines at ~1600 cm^{-1}, and a small secondary amide II peak around 1535–1540 cm^{-1} visible in some samples.[36,37] DAP, EDA, and HMDA functionalized samples exhibit nearly identical peaks, as they functionally differ only in alkyl chain length, slight degree of substitution differences, and extent of cross-linking.

The spacing and geometry of the CNC surfaces and specifically the proximity of the carboxylic acids are crucial in understanding the possibility of intra-fiber cross-links. As mentioned earlier, along a single linear cellulose polymer on a crystalline cellulose surface, only alternating AGU have exposed C6 hydroxyl groups or, after the selective oxidation procedure, carboxylic acids. The distance between two carboxylic acids on the same linear chain is, based on the surface density of surface hydroxyl groups, greater than 7 Å.[30,158] Based on standard bond angles and lengths, the length of a 1,3-diaminopropane molecule is about 5.7 Å, therefore it is unlikely these surface-to-surface cross-links could occur within a single linear chain. However, adjacent cellulose chains on the CNC surfaces may be close enough such that a single diamine could couple to two acids on the same surface. Depending on the crystallinity and face of the CNC, neighboring chains are spaced by 4–6 Å.[161] There is additional complexity in the orientation, position, and size of the C6 carboxylic acids, so these numbers are only useful in qualitative comparison. Given reasonable proximity and conditions suitable for coupling, however, some intra-fiber cross-linking may be occurring, especially for alkyl diamines with three or more carbon chains (DAP, HMDA).

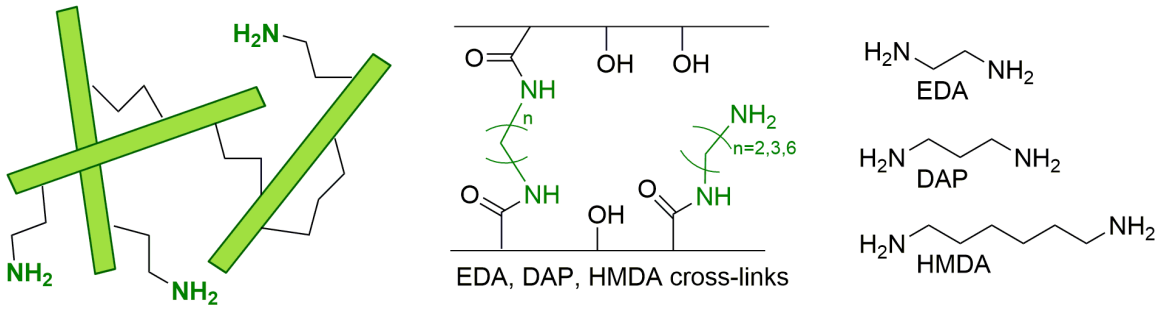

Figure 2.4 – Schematic of proposed possible inter-CNC cross-linking through amide coupling of diamine molecules used for amine-functionalization and cross-linking studies.

Cross-linking is not the only possible explanation as to why the ratio of coupled amine molecules to available acid is less than one; while the aqueous amide coupling reaction is fairly robust and performed under mild conditions, steric accessibility and thermodynamic driving forces could limit the conversion such that there are residual acid groups present on the functionalized CNC surfaces. Diamines bonded to one carboxylic acid may interact non-covalently with another nearby acid through hydrogen bonding, and dense coupling of functional groups could crowd the surface and reduce the likelihood that the relatively high density carboxylic acid groups are fully coupled 1:1 with diamines. Propylamine, a monoamine analog to 1,3-diaminopropane, was coupled to the same oxidized CNC material as DAP and yielded a >0.95 ratio of coupled amine to initial acid. Propylamine is a slightly smaller molecule than DAP, but this near complete conversion would imply that the forces hindering similar 1:1 conversion with DAP are likely electrostatic in nature, in combination with covalent cross-linking effects. The alkyl tail of a coupled propylamine would only contribute a steric effect in reducing the accessibility to and reactivity of free surface carboxylic acid species with additional amines. This material serves as an interesting point of reference for both the extent of reaction and cross-linking

in addition to being, as discussed later, a control catalytic material without primary amine basic sites.

Multi-angle dynamic light scattering was used to investigate the extent of interparticle cross-linking via analysis of solution particle size. The hydrodynamic radius fit from DLS measurements is not necessarily an accurate quantitative metric of absolute cross-linked particle size, but trends in radii can give important information about multi-CNC aggregate sizes. As all materials were treated with identical dispersive processing, i.e. dilution, sonication, and diffusion at ambient conditions, the particle size distributions of cross-linked samples should be indicative of relative degrees of cross-linking. DLS results were compared across all samples synthesized from partially desulfated CNCs to eliminate degree of sulfation as a confounding variable. As seen in Figure 2.5, DAP-coupled CNCs exhibited the largest hydrodynamic radius, followed by nearly equivalent hydrodynamic radii of HMDA- and EDA-coupled CNCs. Diamide-coupled and, therefore, partially cross-linked samples saw up to a five-fold increase in r_h when compared with the partially desulfated CNC starting material. These data are indicative of moderate interparticle cross-linking by means of diamide coupling or electrostatic interactions. Still, the increase in r_h is less than an order of magnitude, meaning that relatively few CNC particles are covalently cross-linked in the average aggregate. A rough calculation indicates that a fully selectively oxidized rectangular CNC of average length would have approximately 5000 carboxylic acids per 5×150 nm face, theoretically a very small portion of which could be needed to form stable interparticle cross-links. Another potential factor in the increased hydrodynamic radii could be a reduction in dispersability leading to particle agglomeration. For the sake of this discussion, it is asserted that the primary factor

controlling particle size distribution is interparticle cross-linking as the pre-measurement dispersive processing should break up weak non-covalent agglomerates.

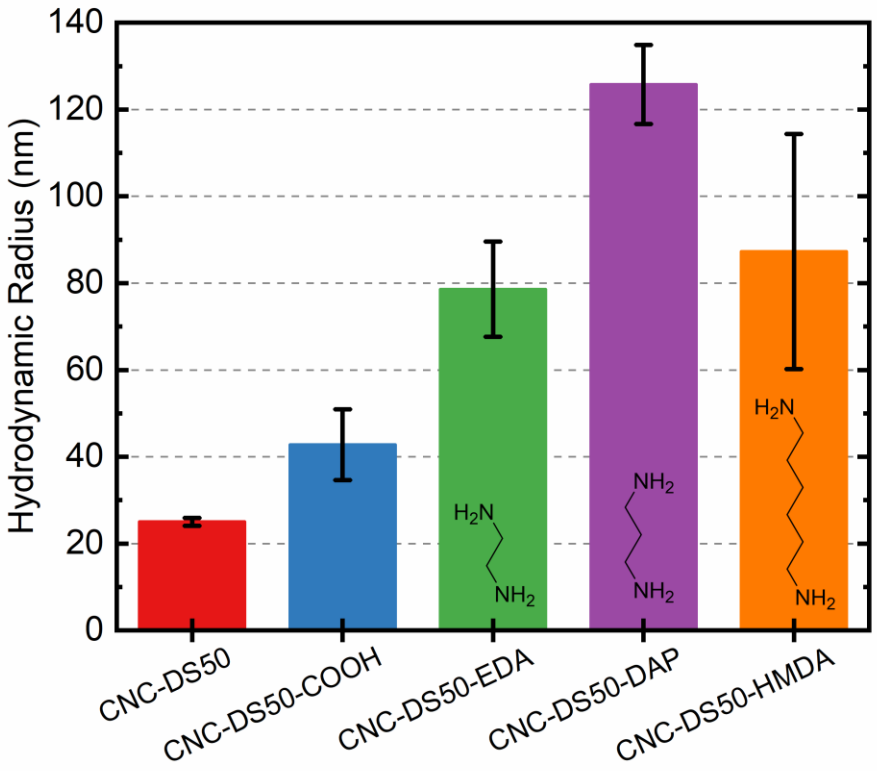

Figure 2.5 – Hydrodynamic radii calculated from multi-angle DLS measurements taken of CNCs across varying states of functionalization demonstrating extent of cross-linking occurring.

The length of the DAP molecule, as discussed above, makes intraparticle cross-linking possible but somewhat rare, as the COOH–COOH spacing is similar in size to the length of DAP. This reduces the likelihood of significant intraparticle cross-links, but the three-carbon diamine length and flexibility are likely sufficient for numerous inter-fiber covalent cross-links to form. This slight selectivity toward inter-fiber links may be the primary factor in the maximum in r_h seen with DAP. Ethylene diamine has only two carbons, which significantly reduces the intra-fiber cross-linking capabilities as the acid–

acid spacing typically exceeds the length of the diamine. The decreased length and flexibility of EDA in comparison to DAP may also, however, decrease the likelihood of inter-fiber links. The final EDA loading of these samples was higher than that seen with the increased size diamines, which could be attributed to the reduced quantities of both inter- and intra-fiber cross-links as well as the reduced steric hindrance of smaller surface functional group. The EDA-coupled CNCs were closer to the theoretical maximum 1:1 diamine:acid coupling as a result. Finally, HMDA-coupled CNCs showed a similar average hydrodynamic radius to EDA, however with a larger distribution of particle sizes. With the increased length and flexibility of a six-carbon spacer between amine molecules, it is more likely to have increased degrees of both intra- and inter-fiber cross-linking. Increasing the likelihood of both types of cross-linking can lead to both smaller (primarily intra-fiber) or larger aggregates (primarily inter-fiber), resulting in the larger particle size range measured. In general, the increased likelihood of intra-fiber cross-links reduces the average particle size, as the possibility of both types would decrease the total number of inter-fiber attachments possible assuming a similar total number of cross-links, as evidenced by the similar diamine loadings in DAP- and HMDA-coupled materials.

2.3.3 CNC Organocatalysts in Aqueous Aldol Condensation Test Reactions

While the details pertaining to the nature of and relative degrees of cross-linking represent important aspects of understanding the chemical content and form of these functionalized CNCs, the catalytic functionality remains dominated by the free primary amines that act as the key functional group in the acid-base catalysis of the aldol condensation reaction. When catalyzed by organic acids and bases, the aldol condensation reaction used here, Figure 2.2, is understood to begin mechanistically with the nucleophilic

attack by a base, in this case a free primary amine, on an activated acetone molecule. The resulting enamine serves as the nucleophile in forming the new C–C bond to an activated aldehyde substrate, here 4-nitrobenzaldehyde. The reaction proceeds through various further steps, but the proximal availability and action of a base and an acid site for enamine generation and substrate activation are key in catalysts with good activity for this reaction.[108,162] Adapting typical reaction conditions from relevant heterogeneous organocatalysis literature, an excess of acetone was used with a moderate concentration (25–50 mM) of the aldehyde substrate and internal standard. The functionalized, partially cross-linked CNCs dispersed in liquid solvent act as heterogeneous catalysts in homogeneous dispersion with a reaction solution. As surface availability is key, preventing agglomeration and maximizing dispersability was a primary concern. It was found that the amine-functionalized CNC materials formed stable dispersions at room temperature in DI H_2O:acetone co-solvent mixtures down to a 3:5 volume ratio. Thus, to minimize agglomeration, this composition was used in reaction experiments. The quality of dispersion and stability were assessed optically, as the co-solvent mixture hindered collection of useful dispersion data by DLS. Water is known to have very low background activity in catalyzing the aldol condensation reaction;[117,163] however, the reaction rates achieved here are in clear excess of this background rate, as seen in Figure 2.6a.

Kinetic experiments under these solvent conditions were performed with unmodified FPL CNCs (control), CNC-DAP, CNC-DS50-DAP, and CNC-DS50-PrA. Preliminary reaction screening with DAP catalysts, expected to be the most active, showed low activity at mild temperatures typically used in this reaction system. Reaction temperature was increased to 80 °C to achieve sufficient reaction rates and each experiment

was run for a total of 48 h. A higher reaction temperature was feasible as the reaction mixture contained a significant amount of water, whose boiling point is well above that of acetone. These reactions were run at 10 and 20 catalyst mol%, calculated based on the total amine molecule loading on the CNCs. Due to the partial cross-linking of these materials, and as catalyst quantities were calculated based on total amine molecule loading, the true quantity of available catalyst sites, theoretically the free primary amines, is likely lower than expected. This effect is relatively minor and is of a similar order for all materials compared, but it does prevent truly precise quantification of site-specific rates. Site-specific rates can be estimated from regression of the low time, approximately linear conversion region. Reaction kinetics data for the water/acetone reaction mixtures are shown in Figure 2.6a.

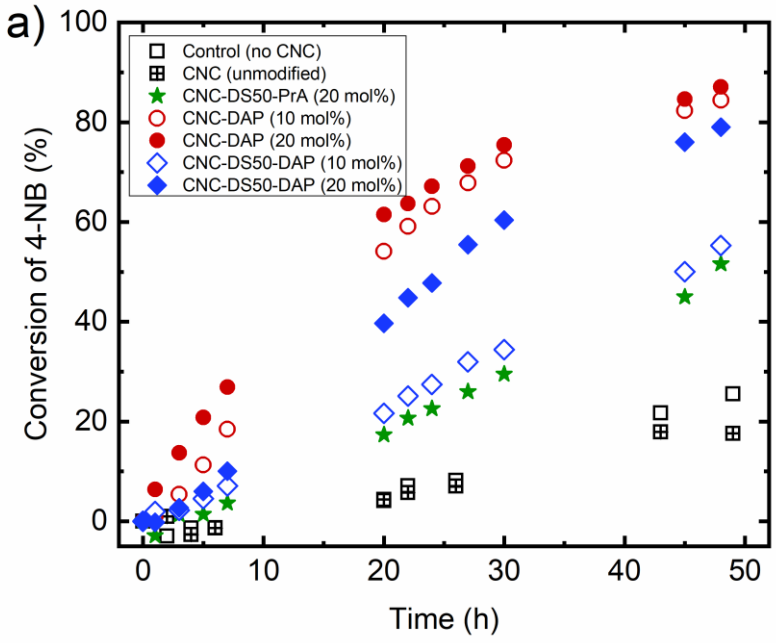

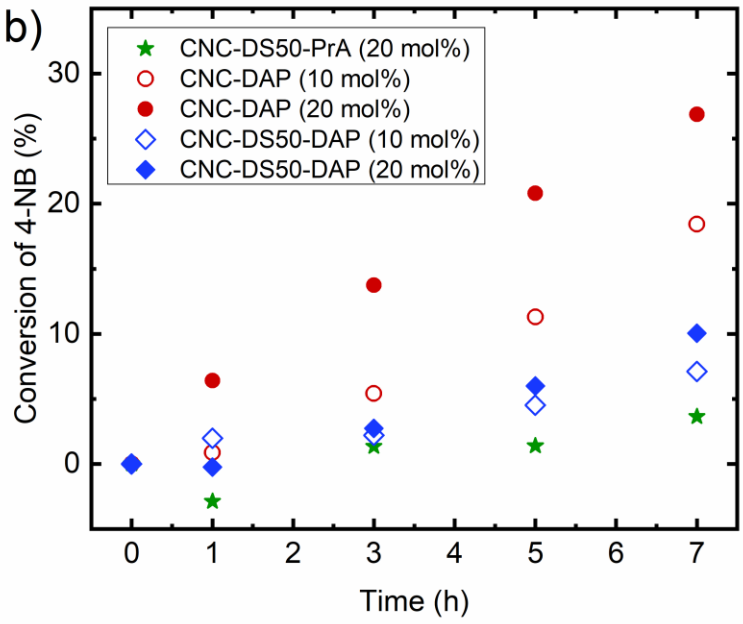

Figure 2.6 – a) Aldol condensation kinetics for DAP-functionalized CNCs as well as various control materials, run at varied catalyst mol% values in 3:5 water:acetone at 80 °C. b) Short time conversion data for catalytically active CNC materials, where initial rates are more clearly differentiable and determined by active site availability and activity.

Despite the relatively slow reaction rates, several important conclusions may be drawn from these data. From kinetic experiments performed with no CNCs in solution, there is indeed a low background reaction rate attributable to the presence of amphiphilic water and the reasonably high reaction temperature, however this background rate is significantly below all rates observed with amine-functionalized CNCs. In the short time region in which the initial reaction rate is quantified, the background rate is effectively negligible. In addition, the rates observed with the addition of unmodified CNCs are consistent with rates with no CNCs present, indicating that unmodified CNCs do not observably catalyze the aldol condensation. Rates sufficient for qualitative and quantitative comparison are measured with DAP and PrA materials. As expected, the initial reaction rates (Table 2-2) approximately doubled in experiments with both DAP catalysts when the

mol% catalyst was doubled from 10 to 20. This serves to verify that the quantity of available catalyst was controlling the observed reaction rates and suggests that the free amines are effective organocatalyst base sites. While some cooperative acidity may be afforded by the presence of water in solution, more likely cooperative partners are the various surface acid species present. The propylamine functionalized sample had above background catalytic function despite lacking free primary amines. The presence of water as an amphiphilic homogeneous species can aid in atypical pathways catalyzed in part with weakly basic surface species like the primary amide of this sample. Supported organocatalyst literature suggests that weaker acids, like weakly acidic silanols on silica surfaces, are sufficient as cooperative acid partners in an acid-base catalyzed aldol condensation mechanism and are even superior to stronger acids like sulfonic and carboxylic acids.[113,143] Residual carboxylic acids, sulfate ester content, and various surface AGU hydroxyls (mainly C2 and C3) are possible cooperative partners for this reaction. The sulfate ester content and therefore the available cooperative acidic functionality of the CNC surfaces was varied with the initial partial desulfation. The DAP catalyst with ~50% reduced S content had catalytic rates approximately half of those observed in DAP catalysts synthesized without desulfation. This could be attributed to this reduction in cooperative acid content, rendering some base sites less effective without proximal acid sites, and/or to a dispersion or solvation effect. The sulfate esters are key in maintaining aqueous dispersion of native CNCs, and partial desulfation may affect the surface accessibility and therefore effective catalyst availability by reducing particle dispersion.

Given that the active catalyst sites are similar between the functionalized CNC materials and, for example, silica-based organocatalysts investigated in literature, it was

somewhat surprising that the observed rates were only modest with the CNC catalysts. There are various contributing factors that may have limited rates. The ratio of base sites to total acid sites (sulfate esters and residual carboxylic acids) is above or close to 1, so cooperative acid availability may be limiting. The highly hydrophilic nature of CNCs may result in preferential solvation with water over acetone, as hydrophilic biomolecules have been shown to develop hydration shells in co-solvent systems with several layers of water immediately surrounding the surface. The dynamics of these hydration shells may additionally be restricted, slowing exchange and motion of solvent particles in this shell.[164–168] The organic substrate, 4-nitrobenzaldehyde, is preferentially dissolved in acetone and poorly miscible with water. As shown in Figure 2.7a, a solvent shell of water could introduce transport limitation into the reaction solution, such that reactant(s) are less likely to reach the reactive surface and active sites. This would indicate that the measured rates are not indicative of the intrinsic active site activity but instead a convolution of the transport limitations and the intrinsic catalytic rate. This is supported by the observed partial immiscibility of some products, including the larger crossed-aldol product, in the final reaction solution. Some phase separation was observed after the 48 h reaction was cooled and no longer stirred, and this small immiscible oily phase supports the existence of imperfect miscibility and phase behavior.

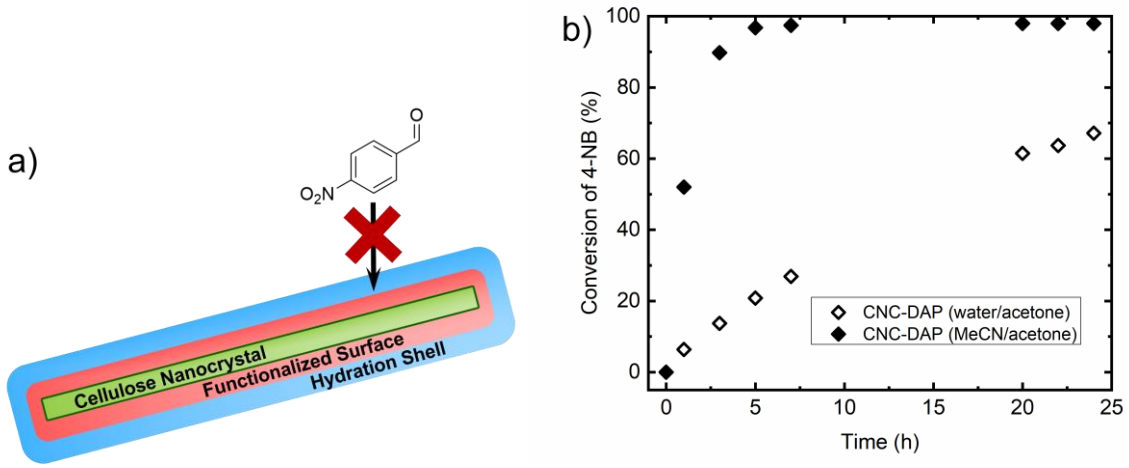

Figure 2.7 – a) Schematic of the proposed preferential solvation issues hindering substrate transport from bulk solution to active catalyst surface when reactions are performed in the presence of significant amounts of water. b) Effect of solvent systems on aldol condensation kinetics catalyzed by CNC-DAP materials. Both reactions were run at 80 °C, 20 mol% catalyst, and 25 mM 4NB reactant.

2.3.4 CNC Processing and Catalyst Rate Analysis in Organic Solvents

CNCs typically form stable suspensions and are best dispersed in water, at least in their native hydrolyzed forms. It has also been shown that small amounts of water can mechanistically improve the rates of the aldol condensation studied by preventing side product formation.[163] Due to the solvation and miscibility effects noted above, however, a significant presence of water in the reaction solutions was detrimental. Fully drying CNCs typically causes irreversible agglomeration, but solvent exchange may be used to adjust solvent without fully drying the samples, passing instead through a gel stage. To ensure a fully miscible reaction solution, the water content of reaction solutions containing CNCs was minimized by a solvent exchange described in the experimental section, yielding an organic-only reaction suspension comprised of 50:50 acetonitrile:acetone by volume. Acetonitrile was chosen as a co-solvent after miscibility screening as it is fairly polar and aprotic, and it has been shown to have negligible effect on aldol condensation reaction rates

when used as a co-solvent with acetone.[163] In addition, it has a boiling point (82 °C) above that of acetone (56 °C), allowing for elevated reaction temperatures. Non-aqueous media for functionalization reactions of CNCs are quite commonly used, and partial agglomeration through solvent exchange or less than perfect dispersion does not necessarily limit surface accessibility at the molecular level. These amine-functionalized CNCs are decorated with fairly polar functionalities, however there is some increased hydrophobic character due to the introduction of small aliphatic diamine molecules on the surface. Despite solvent exchange passing through a gel phase, the ultimate resuspension for reaction forms a stable and visually homogeneous suspension with stirring at elevated (reaction) temperatures. Non-covalent and never-dried minor CNC aggregates could be considered analogous in tortuosity and porosity to other porous heterogeneous catalysts used in liquid-phase reaction systems, which often contain a high degree of meso- and even microporosity. By these justifications, solvent exchange to polar aprotic organic solvent systems for kinetic experiments using CNC catalysts is a reasonable approach that should not introduce extra-catalytic reaction rate limitations.

Table 2-2 – Initial rate data for catalyzed and control aldol condensation reactions in water:acetone (white background) and MeCN:acetone (grey background)

	Mol% catalyst[a]	Temperature (°C)	Initial reaction rate (mM/h)	STY (h^{-1})[a]
CNC-FPL	-	80	0	-
CNC-DS50-PrA	20	80	0.10	0.020
CNC-DAP	10	80	0.67	0.27
CNC-DAP	20	80	0.94	0.19
CNC-DS50-DAP	10	80	0.23	0.093
CNC-DS50-DAP	20	80	0.37	0.075
CNC-DS50-COOH	-	60	0.005	-
CNC-DS50-DAP	10	60	11	2.2
CNC-DS50-EDA	10	60	2.1	0.43
CNC-DS50-HMDA	10	60	2.3	0.46

Initial rates were calculated using the slope of the approximately linear low time region of kinetic data.
[a]Mol% catalyst and site time yield (STY) calculated using total amine molecule content. True mol% may be lower and STY may be greater as free primary amine content is reduced somewhat due to partial cross-linking.

As shown in Figure 2.7b, solvent exchange to an organic solvent mixture and elimination of water improved catalyzed reaction rates at otherwise identical conditions by approximately an order of magnitude. This is due in large part to the removal of various limitations described above, namely related to preferential solvation and transport limitations, as well as potential bulk miscibility issues. Initial demonstrations were performed at 80 °C, but further kinetic experiments were performed at a reduced temperature (60 °C) and mol% catalyst (10). Observed heterogeneous organocatalytic rates with DAP materials are of similar order to those measured for this reaction system on more well-studied silica-supported materials,[121,141,142,163] evidence that comparable catalytic

activity may be achieved with analogous heterogeneous bifunctional active site chemistries supported on CNCs. The CNC catalysts were highly selective for the dehydration product (**3**) of the aldol condensation, as analyzed by ^{1}H NMR of the product mixture (Figure A.5, Table A-1). Up to 88% selectivity to **3** was achieved with the most active catalyst, CNC-DS50-DAP. The CNC catalysts studied here are, additionally, less optimized than well-studied silica-supported organocatalysts, which feature an excess of cooperative weak acid sites and simpler surface chemistry. Surface hydroxyls in silica-supported organocatalysts, with pK_a values between 4 and 9,[111] have been shown to be effective weak acid partners, however the residual surface hydroxyls of CNCs are even weaker acids (pK_a 10–14)[169] and may partially be inaccessible due to their orientation, inflexibility, and hydrogen bonding with other CNC surface or bulk chemistries. The complexity of the CNC surface, which includes free primary amines, some cross-linked diamides, residual carboxylic acid functionality, sulfate esters, and various remaining surface hydroxyls, means there is no single defined active site. The effective active sites based on this surface chemistry likely consist of a free primary amine in proximity to one or more carboxylic acids or sulfate esters, either of which may act as cooperative acids in the proposed catalysis. As such, the catalyst rates are analyzed quantitatively as site time yields (STYs, Table 2-2), which are defined as the initial rate per active site but may include some convolved limitations including base sites lacking proximal cooperative acids, partial cross-linking decreasing free amines, and/or minor transport and are thus not necessarily the intrinsic active site activities.

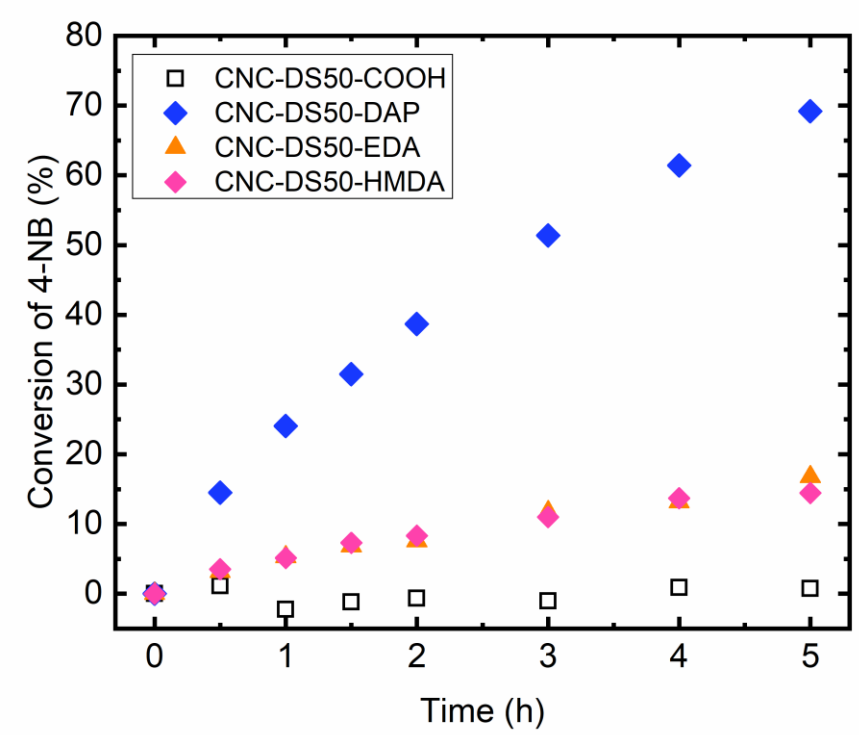

Figure 2.8 – Kinetics of the aldol condensation for various CNC catalyst materials. All reactions were performed in 50:50 MeCN:acetone at 60 °C with 10 mol% catalyst and 50 mM 4-NB.

The catalyzed reaction rates with CNC-DS50-DAP are significantly greater than those achieved with HMDA- or EDA-functionalized CNCs, shown in Figure 2.8. While increased linker length from the surface to the primary amine should not intrinsically reduce catalyst activity, as basicity and nucleophilicity are minimally affected and which has been demonstrated in literature for silica organocatalysts,[111] the observed rate at equal mol% catalyst is quite low with CNC-DS50-HMDA. As discussed above from DLS data, the length and flexibility of HMDA molecules likely leads to significant increases in cross-linking, particularly the extent of intra-fiber links formed. The catalyst loading is calculated from total diamine content, so a significant fraction of cross-linking would reduce the effective mol% of free amine dramatically and therefore the relative reaction rates. CNC-DS50-EDA, which should not have as much of an issue with over-cross-linking, also

exhibits low catalyst activity relative to DAP materials. The shorter linker is likely causing substrate accessibility and base-acid pairing limitations, such that the base sites are effectively more isolated and successful cooperative acid-base interactions are less likely. Linker length limitations have been investigated in silica organocatalysts, wherein a minimum of a three carbon spacer from the surface to active primary amine were necessary to reach a maximum in site-specific activity.[143]

2.4 Conclusions

Cellulose nanocrystals are being investigated in an ever-expanding breadth of applications, and the ability to impart specific physical or chemical function through surface modification is central to their broad usefulness. Utilization of CNCs as catalyst supports is a growing field and advancing CNCs as multifunctional catalysts through direct chemical modification may open new opportunities for CNC applications. Inspired by the growing field of supported organocatalysis, this study is an early demonstration of CNC-supported organocatalysis, specifically with acid-base bifunctional materials. Aqueous-only chemical modification through selective TEMPO oxidation and subsequent EDC amide coupling resulted in CNC catalysts with acid (sulfate esters, carboxylic acids) and base (primary amines) functionality. Sulfate ester content was varied through partial desulfation. Coupling aliphatic diamines of various sizes to oxidized CNCs resulted in varying degrees and types of cross-linking. This demonstrated how the particle size distribution and type of cross-linking may be controlled using linkers of different lengths.

Catalysts were tested for their activity in the acid-base catalyzed C–C bond forming aldol condensation reaction between acetone and 4-nitrobenzaldehyde in two solvent

systems, namely water:acetone mixtures and acetonitrile:acetone mixtures. Reactions performed in water:acetone required high temperatures and long reaction times, but DAP-functionalized CNCs showed clear catalytic activity relative to the background reactions of control experiments. Reduced sulfate ester content reduced catalytic activity. Solvation, miscibility, and transport limitation issues were addressed by solvent exchange to a polar aprotic organic solvent system, with which drastic rate improvements were achieved. DAP-based catalysts had organocatalytic rates on the order of more optimized silica-supported materials from literature and showed high selectivity toward the dehydration aldol product, while EDA and HMDA catalysts had decreased activity, likely hindered by accessibility and cooperativity limitations and excessive cross-linking, respectively. The relatively complex (compared to mesoporous silicas) surface chemistry was nevertheless successful in its function for acid-base cooperative catalysis, and this demonstration of CNCs as alternative supports for bifunctional heterogeneous organocatalysts may lead to opportunities for new application areas for cellulose nanocrystals.

CHAPTER 3. OPTIMIZATION OF CNC CATALYST DESIGN USING SURFACE ORDER TO OUTPERFORM SILICA-SUPPORTED ORGANOCATALYSTS

Chapter 3 and Appendix B are adapted from a published article: Ellebracht, N. C. & Jones, C. W. Optimized Cellulose Nanocrystal Organocatalysts Outperform Silica-Supported Analogues: Cooperativity, Selectivity, and Bifunctionality in Acid–Base Aldol Condensation Reactions. Reproduced with permission from *ACS Catal.* 2019, 9, 4, 3266-3277. https://doi.org/10.1021/acscatal.8b05180.[170]

3.1 Introduction

Organocatalysis in organic chemistry and pharmaceutical synthesis has been substantially developed in recent decades.[107] Organocatalytic transformations toward fine chemicals have often involved enantioselective amine catalysts like proline,[108,171,172] but the breadth of organocatalyst-mediated reactions is rapidly expanding.[173] Heterogeneous organocatalysts allow for immobilization of multiple catalytic species in a single material for cascade and/or cooperative catalysis.[21,112,127] Silane-modified mesoporous silicas are a major class of heterogeneous organocatalysts studied to date and have been developed with a variety of functionalities, commonly utilizing organic acids and bases.[22,23,109] These acid and/or base catalysts have been used for various C–C bond forming reactions including aldol, nitroaldol, and Knoevenagel condensations as well as Michael addition and deacetalization reactions.

The aldol condensation (AC) of an aldehyde with acetone is a common acid–base cooperatively catalyzed test reaction with an established mechanism,[113,117,120] and many aspects of the active site have been investigated. Acid sites, including sulfonic,[112–115] phosphoric,[113,116] and carboxylic acids,[111,113,116] as well as organic bases like chiral[118] and various alkyl[117,119] amines have been incorporated in silica-supported organocatalysts. Weakly Brønsted acidic silanols have been established as effective cooperative acid partners in aminosilica catalysts due to their abundance and insignificant base-poisoning effects.[111,119,127] However, weak acids of greater strength may be more effective in some cases by reducing reaction activation energy, as was shown for butanal self-condensations.[174]

The mild reaction conditions and acid–base chemistries typical of supported organocatalysts are appropriate for certain key transformations of biomass.[135] Upgrading of biomass-derived furfural via aldol condensation with ketones and subsequent hydrodeoxygenation of condensation products has been studied with a number of inorganic heterogeneous catalysts including zeolites, layered hydroxides, mixed oxides, and noble metals.[175–178] Despite their relevance, heterogeneous organocatalysts have been sparsely utilized for transformations of biomass. Acid-catalyzed conversion of sugars to furans[136] and condensations of sugar-derived furans[115] were shown with supported sulfonic acid catalysts. Nelson *et al* utilized a bifunctional Pd and secondary amine mesoporous silica nanoparticle catalyst for a cascade transformation of furfuryl alcohol to furfural and the aldol condensation product, however with low yields of the final product.[137] Supported organocatalysts are promising yet understudied as components of multifunctional catalysts for cascade furfural upgrading reactions.

Spacing and pairing of acid and base species are key in cooperative catalysis. Polar protic grafting solvents, protecting groups, or multistep functionalizations may aid in dispersion of grafted aminosilanes.[123–126] Moderate loadings with neither site-isolated nor overcrowded aminosilanes was determined to be optimal for the Henry reaction.[126] Without appropriate grafting methods, aminosilane clustering may occur even at very low loadings.[122] Dispersion and acid–base site-pairing in multifunctional silica-supported organocatalysts is even more difficult to control.[114,121] Some control over reaction environment has been demonstrated via silica imprinting with protected aminosilanes.[179,180] Random grafting and the amorphous nature of the oxide supports typical of this material class are limiting factors in the design of cooperative active sites.

Cellulose nanocrystals (CNCs) are an emergent class of advanced bioproducts derived from various cellulose sources with the potential to be produced at scale.[181] CNCs are high aspect ratio, high specific surface area rods (100–300 nm in length) of crystalline cellulose with typically rectangular cross sections (5–10 nm widths).[31] The ordered, hydroxyl-rich surfaces of CNCs are readily functionalizable, modification of which has been widely studied and reviewed.[29,30] TEMPO-mediated oxidation, perhaps the most common chemical modification of CNCs, selectively oxidizes the primary (C6) surface hydroxyls to carboxylic acids, which are regularly ordered due to the crystalline nature of cellulose.[28,161]

CNCs have been used as catalyst supports primarily through reduction of noble metal salts into nanoparticles on oxidized surfaces[88] and are studied with test reactions under mild conditions. The slight chiral twist of CNC rods has been shown to promote enantiomeric selectivity in Pd-catalyzed hydrogenation[95] and amino acid hydrolysis.[103]

Several studies have utilized CNCs as direct organocatalysts. Hydrolysis reactions have been performed with unmodified CNCs[103,104] as well as TEMPO-oxidized nanofibers.[105] Kanomata *et al* performed aldol condensations catalyzed by a combined heterogeneous–homogeneous system of oxidized nanofibers and homogeneous proline.[106] More recently, our previous work was an initial demonstration of acid–base bifunctional CNCs as cooperative heterogeneous organocatalysts for AC test reactions.[138]

There is a large body of work refining and probing aspects of aminosilica organocatalyst materials and surface chemistry for C–C bond forming reactions. In contrast, only our prior work explores similar issues on nanocellulose.[138] The present study greatly expands upon the preliminary acid–base CNC organocatalyst design established in our previous work to explore the surface chemistry and structure of CNCs as they pertain to this catalysis. Cellulose nanocrystal-supported catalysts are synthesized by TEMPO-mediated oxidation and subsequent amine functionalization by amide coupling of diamines to a portion of the surface carboxylic acids. Sulfate half-ester, carboxylic acid, and amine surface species are quantitatively varied and characterized in an array of CNC catalysts. Coupling of unprotected diamines as well as monoboc protected diamines is used to probe the effects of diamide formation on active site availability. Catalysts are tested in batch aldol condensation reactions of acetone with a test substrate (4-nitrobenzaldehyde) as well as furfural and compared via activity and selectivity to dehydrated products. Analogous mesoporous SBA-15-supported organocatalysts are synthesized and directly compared the CNC-supported catalysts developed here.

3.2 Materials and Methods

3.2.1 Cellulose Nanocrystal Catalyst Preparation

Cellulose nanocrystal (CNC) acid–base organocatalysts were synthesized by chemical modification of CNCs produced by sulfuric acid hydrolysis and purchased from the University of Maine in concentrated aqueous suspension (~10 wt%). CNCs were generally purified by dialysis against deionized water and stored in aqueous suspension at 4 °C. Cellulose nanocrystals with as-received (~0.9 wt% S), partially removed, or significantly removed sulfate half-ester (SE) content were used as starting materials for catalyst preparation. For partial SE removal, an aqueous suspension of CNC (0.5 wt%) and HCl (50 mM) was magnetically stirred at 80 °C for 24 h. For significant SE removal, a similar suspension with increased HCl (250 mM) was magnetically stirred at 100 °C for 24 h. The cooled suspensions were partially neutralized to pH ~4 with NaOH before purification by dialysis and concentration by ultrafiltration.

These CNCs were subsequently oxidized by an oft-reported procedure[28] mediated by (2,2,6,6-tetramethylpiperidin-1-yl)oxyl (TEMPO) with which low or high extents of oxidation were achieved by varying the NaClO content. To CNC suspensions (2 wt% in H_2O), TEMPO (0.1 g/g_{dry} CNC), NaClO (less oxidation: 0.42; more oxidation: 1.9 g/g_{dry} CNC), and NaBr (1 g/g_{dry} CNC) were added and dissolved with stirring. The mixture was stirred at room temperature for 4 h, during which the pH was continually adjusted to between 10 and 11 with NaOH (1 N) until stabilization. NaCl was then added to flocculate the oxidized CNCs, and the product was washed by centrifugation and decanting (three times with 0.5 M NaCl; two times with 0.1 M HCl; once with DI water) before final

purification by dialysis. Oxidized CNCs were further modified by aqueous amide coupling with 1,3-diaminopropane (DAP, >99%, Sigma-Aldrich) or n-boc-1,3-diaminopropane (bocDAP). The singly protected diamine (bocDAP) was synthesized by previously reported methods (Figure B.1).[182] DAP or bocDAP (five molar equivalents with respect to CNC carboxylic acid content), 1-ethyl-3-(3-(dimethylamino)propyl)carbodiimide hydrochloride (1.5 equiv, >99%, Sigma-Aldrich), and *n*-hydroxysuccinimide (1.5 equiv, 98%, Sigma-Aldrich) were added to suspensions of oxidized CNCs (1–2 wt% in H_2O). The pH was adjusted with HCl to 7.5–8, and the mixture was stirred overnight at room temperature prior to purification. CNCs functionalized with bocDAP were hydrothermally deprotected by stirring aqueous suspensions (0.5 wt%) at 100 °C for 7 h.

3.2.2 SBA-15 Catalyst Preparation

SBA-15 aminosilica catalysts were prepared according to previously reported methods.[111] To synthesize mesoporous SBA-15, pluronic P123 copolymer (24.0 g, Sigma-Aldrich) was dissolved in deionized water (636 mL) and hydrochloric acid (120. mL, 12.1 M). Tetraethylorthosilicate (TEOS, 46.26 g, 98%, Sigma-Aldrich) was added, and the solution was stirred at 40 °C for 20 h. The stir bar was removed, and the temperature was increased to and held at 100 °C for 24 h. The solids were filtered and washed with deionized water (4 L) followed by drying overnight at 75 °C. Finally, the material was calcined (RT to 200 °C at 1.2 °C min^{-1}, 200 °C for 1 h, 200 to 500 °C at 1.2 °C min^{-1}, 550 °C for 12 h, cool to RT) and dried overnight (110 °C, 10 mTorr) before storage or use.

Acid–base aminosilica catalysts were prepared by silane grafting. Dried SBA-15 (1.5 g) was stirred under inert atmosphere (N_2) in toluene (37.5 mL) with the desired silane

(199 mg, 3-aminopropyltriethoxysilane, APS, Gelest) for 24 h. Subsequently, deionized water (30 µL) was added and the mixture was stirred at 80 °C for 24 h followed by filtration and washing with toluene, hexanes, and ethanol. The washed powder was dried overnight (110 °C, 10 mTorr) before storage or use. An aminosilica catalyst incorporating both grafted carboxylic acid and primary amine silanes was also synthesized. A protected acid silane, *t*-butyl 2-methyl-3-(triethoxysilyl)-propanoate (191 mg, TBSP, synthesized as previously reported,[111] Figure B.2), was similarly grafted to bare SBA-15 (1.5 g). APS (110 mg) was subsequently grafted to this intermediate material (1.2 g) with the above approach. The *tert*-butyl protecting group was removed by heating to 270 °C for 12 h under flowing N_2 exhausted through a bubbler. The APS-only catalyst is denoted by SBA-APS, and the dual grafted catalyst is referred to as SBA-COOH-APS.

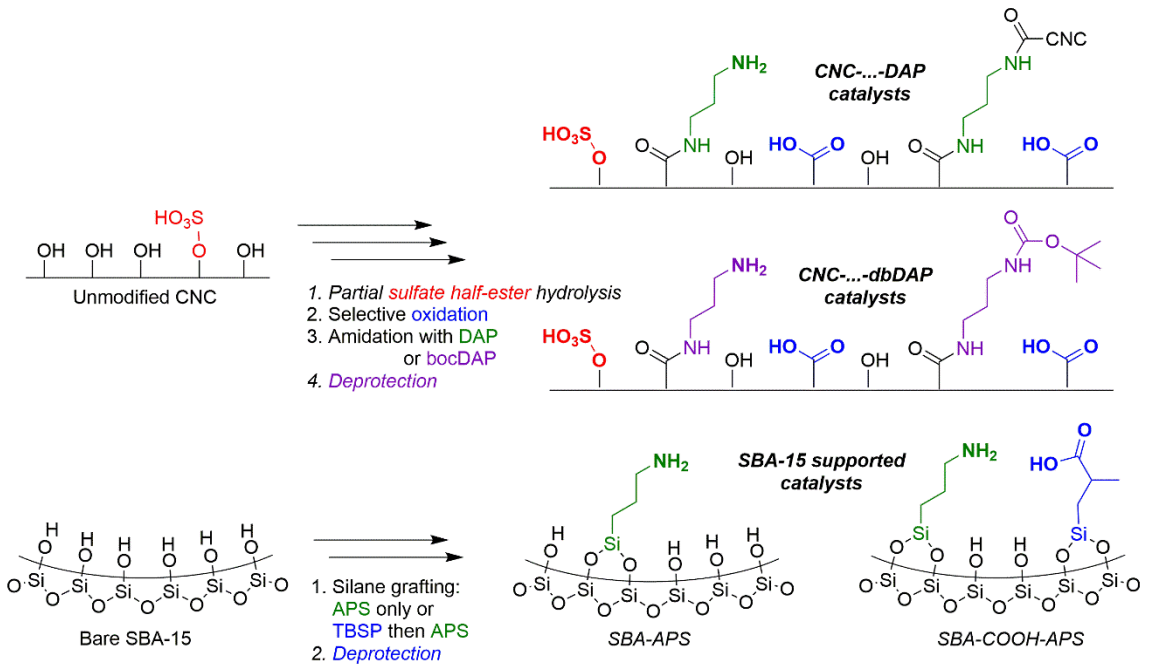

Figure 3.1 – Synthesis scheme for cellulose nanocrystal- and SBA-15-supported acid–base organocatalysts. Partial diamide cross-linking and incomplete deprotection are shown for DAP and bocDAP CNC-based catalysts, respectively; the relative quantities of the surface species shown are not quantitatively accurate. Italicized steps were performed only for a subset of the materials synthesized.

3.2.3 Catalyst Characterization

Freeze-dried CNC materials and silica materials were analyzed by combustion elemental analysis (EA) performed by Atlantic Microlab, Inc. for elemental content (some or all of: C H N S). Conductometric titration was performed to quantify the carboxylic acid content of oxidized CNCs. Simultaneous pH and conductivity measurements were recorded with a Hanna Instruments benchtop meter. Suspensions of CNCs (~0.1 wt%) were acidified (pH ≈ 3), purged with N_2 (30 min), and titrated with NaOH (0.100 N) to pH >10. Acid content was determined from the low slope portion of the conductivity curve around pH 4–8. Freeze-dried CNC and silica samples were pelletized with KBr and characterized by Fourier transform-infrared (FT–IR) transmission spectroscopy with a Nicolet iS10 Spectrometer. BET surface area and pore volume of silica materials were determined from N_2 physisorption isotherms collected with a Micromeritics TriStar II instrument. Thermogravimetric analysis (TGA) was performed with a Netzsch STA409 instrument to determine grafted silane loadings in SBA-15 materials. Powder samples were analyzed during heating from 30 to 900 °C at a ramp rate of 10 °C min^{-1} under combined air (90 sccm) and N_2 (30 sccm) flow. Representative Iβ cellulose crystal structures were generated with the Cellulose-builder toolkit[183] and modified in Jmol.

3.2.4 Aldol Condensation Reactions and Product Analysis

CNC and SBA-15 catalysts were tested in batch aldol condensation reactions of 4-nitrobenzaldehyde or furfural with acetone repeated at least three times. Reactions were performed in condenser-fitted two-neck 25 mL round-bottom flasks with 10 mol % catalyst (calculated for CNC catalysts: active site loading = total diamine content = 1/2 nitrogen

content; for SBA-15 catalysts: active site loading = total amine content = nitrogen content) at 60 °C in 50:50 v%:v% acetone/acetonitrile (4 mL) suspensions containing either 4-nitrobenzaldehyde or furfural as the starting material and 1,4-dimethoxybenzene as an internal standard (all 50 mM). Reactions with furfural were performed under inert (N_2) conditions. CNC catalyst processing was described in a previous work.[138] Briefly, a volume (typically 2–5 mL) of a stored aqueous suspension containing the desired mass of CNC was dialyzed against 50:50 v%:v% acetone/acetonitrile (1 L) overnight. The resulting gel was carefully transferred and washed with this solvent mixture three times before being transferred to a reaction flask in a 3 mL suspension. For silica catalysts, the material was dried overnight (100 °C, 10 mTorr) and combined with 3 mL of the solvent mixture in the flask. The reaction vessel was sealed, purged with N_2 (for reactions of furfural), and heated to 60 °C with stirring before a solution (1 mL) of the starting material and internal standard (200 mM in acetone/acetonitrile) was injected. Aliquots (50–100 µL) were taken via needle at regular intervals and analyzed by flame ionization detector with a Shimadzu gas chromatograph. Reactions were cooled after 6 h and final mixtures were collected by filtration. Collected reaction mixtures were concentrated by rotary evaporation and dissolved in DMSO-d_6 for analysis via ^{1}H NMR with a Bruker Avance III 400 MHz NMR.

3.3 Results and Discussion

3.3.1 CNC Surface Chemistry

The surface functionalization methods used result in CNC surfaces with an array of surface species including: (1) cellulose hydroxyl groups, (2) sulfate half-esters (SEs), (3) carboxylic acids (in the C6 position of anhydroglucopyranose cellulose monomers), and

(4) amide-coupled diamines with free primary amines. An array of cellulose nanocrystal-supported acid–base organocatalysts was synthesized by controlling the quantities of these surface species as well as the type of diamine used for amine functionalization (Figure 3.1). The effects of each on resulting catalytic function were probed by varying aspects of the surface chemistry. The initial quantity of surface hydroxyls is defined by cellulose crystal structure and geometry.[158] Sulfate half-ester and coupled diamine contents of a given material were calculated from S and N wt % from elemental analysis. The carboxylic acid contents of oxidized CNCs were determined prior to amide coupling by conductometric titration.

All surface species originate from the exterior hydroxyl groups of cellulose nanocrystals, initially ~4.3 mmol OH per g_{CNC} for Forest Products Laboratory CNCs with cross-sectional widths of ~5 nm.[30,138,158] Unmodified CNC surfaces are slightly decorated with sulfate half-esters (0.28 mmol g_{CNC}^{-1}) resulting from production by sulfuric acid hydrolysis. Partial and substantial hydrolytic removal of SEs with HCl resulted in 36–41 and 89 % reductions in CNC SE content, respectively, consistent with similar procedures from the literature.[184,185] SEs removed by acid hydrolysis result in an additional free surface hydroxyl but do not substantially change the overall hydroxyl surface content. Substantial CNC flocculation occurred when SEs were nearly entirely removed (CNC-DS), noted by increased suspension viscosity and opacity.

CNC starting materials of various SE contents were oxidized under low or high NaClO conditions, resulting in low (0.9–1.0 mmol COOH g_{CNC}^{-1}) or high (1.3) initial carboxylic acid content (Table 3-1). TEMPO-mediated oxidation selectively oxidizes C6 surface hydroxyl groups, which are regularly spaced due to sample crystallinity.[158,161] The

initial surface coverage of C6 hydroxyls is one-third of the total hydroxyl content, about 1.4 mmol g_{CNC}^{-1}, suggesting approximately complete oxidation of these hydroxyls for "high" oxidation samples. These carboxylic acids serve as the grafting sites for the amine functionality achieved through aqueous EDC amide coupling with diamines which followed oxidation.

Amide coupling was performed with either of two diamines: 1,3-diaminopropane (DAP) and *n*-boc-1,3-diaminopropane (bocDAP). A singly boc-protected diamine was utilized to prevent two-site amide coupling of single diamine molecules, which could reduce free amines and result in CNC cross-linking, an approach that has been employed previously.[44] Our previous work demonstrated effective catalysis with catalysts synthesized similarly with 1,3-diaminopropane and gave evidence of a relatively low degrees of cross-linking.[138] Diamine loadings resulting from amide coupling are shown in Table 3-1. CNC catalysts are denoted by the degree of desulfation of the starting material (none: s; partial: ds; high: DS), the extent of oxidation (low: cooh; high: COOH), and the diamine used for amidation (DAP; deprotected bocDAP: dbDAP). A DAP-functionalized CNC sample was also subjected to the hydrothermal treatment used for deprotection (Section 3.2.1) and is denoted by -HT. Amide coupling typically resulted in diamine loadings of around 0.8 mmol g_{CNC}^{-1} regardless of the quantity of available carboxylic acids or diamine type (DAP or bocDAP) with the exception of the highly desulfated material, for which diamine coupling resulted in 0.52 mmol bocDAP g_{CNC}^{-1}. This limit suggests possible steric or electrostatic prevention of further amidation and a practical limit for functionalization density with these diamines.

Removal of the boc protecting group was achieved with simple hydrothermal processing. Numerous methods for boc deprotection were screened, including TFA, HCl, NaI, trimethylsilyl iodide-catalyzed approaches.[186] Deprotection was primarily tracked by FT–IR spectroscopy. Effective cleavage of the boc carbamate group consistently cleaved some of the amide bonds tethering the diamines to the CNC surfaces as well, leading to a trade-off in deprotection and loss of total amine functionality. The 7 h hydrothermal deprotection approach ultimately utilized removed 30–40 % of the total diamines which liberated additional carboxylic acid groups. The total amine content of the hydrothermally treated DAP-functionalized CNC was also reduced by 30 % (Table 3-1).

Table 3-1 – Quantification of relevant surface species and COOH:NH_2 ratio for the array of CNC catalysts synthesized

sample	sulfate half-esters[a] (mmol g_{CNC}^{-1})	initial COOH[b] (mmol g_{CNC}^{-1})	final COOH[c] (mmol g_{CNC}^{-1})	initial diamine[d] (mmol g_{CNC}^{-1})	final diamine[d] (mmol g_{CNC}^{-1})	COOH:NH_2 ratio[e]
CNC-s (unmodified)	0.28	-	-	-	-	-
CNC-ds	0.17	-	-	-	-	-
CNC-DS	0.03	-	-	-	-	-
CNC-s-cooh-dbDAP	0.22	0.92	0.38	0.76	0.54	0.70
CNC-ds-cooh-dbDAP	0.14	0.93	0.42	0.85	0.51	0.82
CNC-DS-cooh-dbDAP	0.03	1.0	0.57	0.52	0.43	1.3
CNC-ds-COOH-dbDAP	0.12	1.3	0.79	0.90	0.51	1.5
CNC-s-cooh-DAP	0.24	0.95	[0.14]	-	0.80	0.18
CNC-ds-COOH-DAP	0.13	1.3	[0.50]	-	0.80	0.60
CNC-ds-COOH-DAP-HT	0.12	1.3	[0.74]	0.80	0.56	1.3

[a]Sulfate half-ester content is assumed to be equivalent to elemental S content.

[b]Determined by conductometric titration prior to amide coupling.

[c]Residual COOH determined by assuming a 1:1 conversion of COOH to amide surface attachments with total diamine content. This is a maximum residual COOH value for DAP-functionalized materials [in brackets] as some cross-linking would convert two COOH per diamine and further reduce residual acid content.

[d]Total diamine content determined by elemental N content (2 N : 1 diamine). The initial content refers to the loading prior to deprotection or hydrothermal (HT) treatment. If no HT treatment after amidation was performed, no initial loading is listed.

[e]This ratio assumes one free primary amine (NH_2) per surface-coupled diamine. Incomplete deprotection (dbDAP) would reduce the effective free primary amine content and partial cross-linking (DAP) would decrease both residual COOH and free primary amine contents.

Analysis of FT–IR spectra of oxidized and DAP-functionalized CNCs was described in our previous work.[138] Full FT–IR spectra are shown in Figure B.4. Chemical species resulting from oxidation and amidation are particularly evident in the 1500–1800 cm^{-1} spectral range. Numerous IR signals, many overlapping, occur in this range: the carboxylic acid C=O stretch (1735–1740 cm^{-1}), the deprotonated COO^- C=O stretch (1605 cm^{-1}), the amide I C=O stretch (1655–1665 cm^{-1}), N–H bending of primary amines (~1600 cm^{-1}), and secondary amide II peaks (1535–1540 cm^{-1}). Importantly, the carbamate C=O of a boc-protected amine (1685–1695 cm^{-1}) was used to qualitatively track the extent of deprotection (Figure 3.2). With deprotection, this peak as well as the amide II stretch were significantly reduced. However, the 7 h hydrothermal deprotection used for all boc-protected samples resulted in some residual carbamate C=O intensity, qualitatively indicative of incomplete deprotection.

Longer times or increased temperature could more fully remove boc protecting groups but would result in significant losses of total amine content. A previous work utilizing similar functionalization chemistries did not discuss or confirm tethering amide cleavage after deprotection with TFA.[44] FT–IR spectra of deprotected bocDAP catalysts

otherwise closely resemble those of the DAP-functionalized catalysts. Additionally, a reduction in relative intensity of the minor amide II peak after hydrothermal treatment of the DAP catalyst suggests fewer amide bonds are present, possibly attributable to a reduction in cross-linked diamide species. This would indicate that the free primary amine loading is closer to the total amine content in the hydrothermally treated DAP catalyst than in other DAP materials.

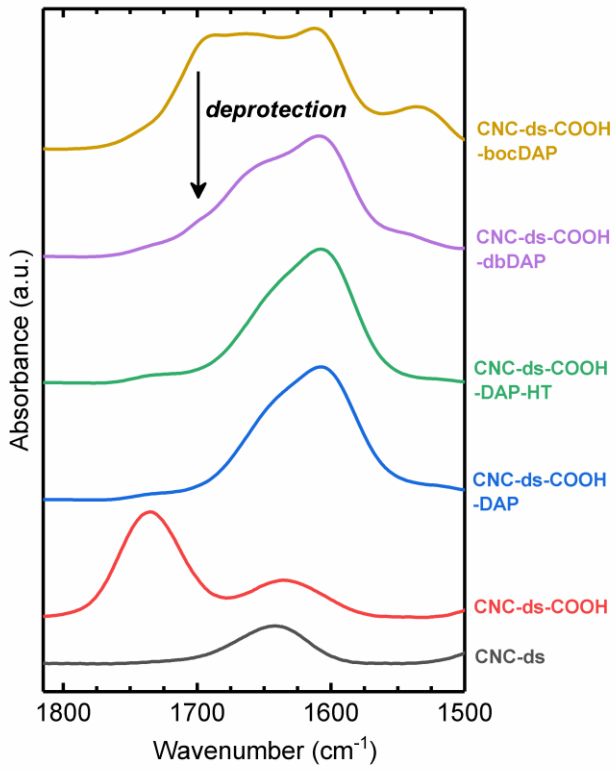

Figure 3.2 – A selected portion of the FT–IR spectra of representative cellulose nanocrystal materials containing important carbonyl and other stretches demonstrating oxidation and functionalization with DAP or bocDAP, as well as subsequent deprotection.

3.3.2 SBA-15 Organocatalyst Characterization

The SBA-15 catalysts used in this work, in particular SBA-APS, have been widely synthesized and studied as catalysts for aldol condensations of 4-nitrobenzaldehyde and

other substrates.[22,23,109,111–113,127] Their inclusion herein is primarily for comparative purposes with CNC catalysts containing similar functional chemistry. Brunauer–Emmett–Teller (BET) surface areas and pore volumes of SBA-15 catalysts and intermediate materials as well as silane loadings are shown in Table 3-2. N_2 physisorption analysis showed the expected type IV isotherms (Figure B.5). Surface areas and pore volumes decreased with each grafting step and increased slightly with deprotection of the carboxylic acid-containing silane.

Thermogravimetric analysis and elemental analysis verified successful grafting of 3-aminopropyltriethoxysilane (APS) and *t*-butyl 2-methyl-3-(triethoxysilyl)-propanoate (Figure B.6). Mass losses from ~200–300 °C are attributed to the removal of the *tert*-butyl protecting group.[111] After thermal deprotection under flowing N_2, there was no mass lost in this temperature range in a subsequent thermal ramp, suggestive of complete deprotection. Final APS and COOH loadings were quantified with elemental analysis (nitrogen) and TGA organic mass losses, respectively (Table 3-2). Silane grafting results were consistent with studies previously reporting these methods.[111] Acid (SBA-COOH-APS) and base (both catalysts) loadings (0.35–0.4 mmol g^{-1}) are of the same order of magnitude as acid and base species in CNC catalysts, but a broader range of loadings and, importantly, acid/base ratios, are found across the CNC materials.

Table 3-2 – Textural properties and quantification of grafted silane species for silica-supported organocatalysts

sample	COOH loading[a] (mmol g^{-1})	NH_2 loading[b] (mmol g^{-1})	COOH:NH_2 ratio	BET surface area[c] (m^2 g^{-1})	Pore volume[c] (cm^3 g^{-1})
SBA-15 bare				805	0.83
SBA-APS		0.35		511	0.70
SBA-TBSP	0.36			648	0.69
SBA-TBSP-APS	0.35	0.38	0.92	423	0.64
SBA-COOH-APS	0.35	0.40	0.88	475	0.68

[a]Quantity of protected (TBSP) or deprotected (COOH) grafted silanes determined by thermogravimetric analysis of mass losses. Mass losses attributed to APS content were accounted for when appropriate.

[b]Primary amine content from grafted APS determined by N elemental analysis.

[c]BET surface area and pore volume calculated from N_2 physisorption data.

The synthetic methods employed were developed to achieve good dispersion of grafted silanes, and the low loadings of aminosilanes in SBA-APS and SBA-COOH-APS are consistent with conditions demonstrated for some degree of site-isolation.[123,125,187] The relative spatial abundance of acid and base species is not directly probed. Initial grafting of TBSP should yield well dispersed silanes due to its relatively bulky and aprotic functional group as well as use of the initial anhydrous stirring step in the synthesis prior to reactive hydrothermal condensation. The dispersion of additional grafted silanes (APS) would be further improved by the sterically bulky and randomly dispersed TBSP grafted first. The random distribution of acidic and basic silanes on the amorphous porous surface of the SBA-15 will be discussed further in the context of these materials' catalytic function. As in the referenced work by Brunelli et al.,[111] FT–IR of the deprotected bifunctional silica-supported catalyst (SBA-COOH-APS) indicates that, despite synthetic efforts for silane dispersion, a significant portion of the carboxylic acids form carboxylates as they are able to interact with nearby primary amines (Figure B.7).

3.3.3 CNC Catalysts in Aldol Condensation Reactions

4-Nitrobenzaldehyde (4NB), a broadly used model aldehyde reactant, as well as furfural (furf), a biomass-derived platform molecule, were studied as aldol condensation (AC) substrates in batch liquid phase reactions (Figure 3.3). Acetonitrile was used as a 1:1 v:v cosolvent with acetone to increase the polarity of the reaction mixture, improve CNC dispersibility, and increase the effective boiling point.[138] Acetonitrile, a polar aprotic organic solvent, has been shown to be have minimal effect on reaction rates in 4NB-AC reactions with heterogeneous organocatalysts.[163] A moderate concentration (50 mM) of the aldehyde substrate was used in reactions with excess acetone and 10 mol % catalyst.

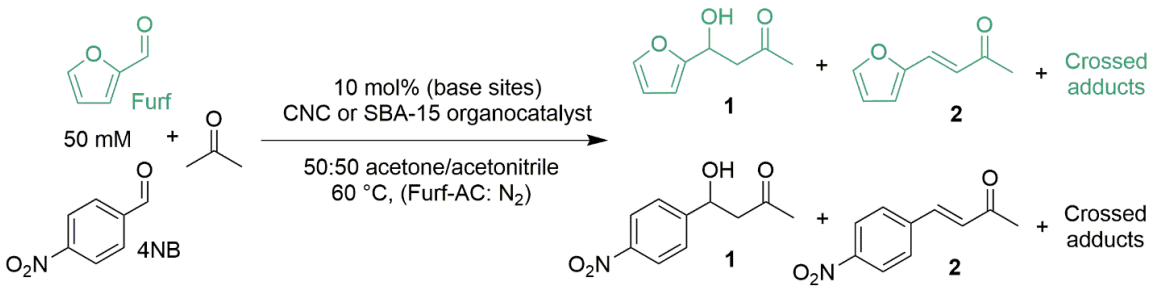

Figure 3.3 – Aldol condensation (AC) reaction scheme of furfural (furf) or 4-nitrobenzaldehyde (4NB) with excess acetone used for catalyst evaluation. The major products of each are the respective aldol (1) and dehydration (2) products while small quantities of crossed aldol adducts and side products were found.

The true availability of free primary amines was not precisely determined, as both synthetic routes, coupling either a diamine (DAP) or a monoboc protected diamine (bocDAP), may result in fewer available primary amines relative to the theoretical quantity (one primary amine per coupled diamine). Some cross-linked diamides may form in the synthesis of DAP catalysts,[138] and incomplete deprotection was evident in deprotected bocDAP (dbDAP) catalysts (Figure 3.1 and Figure 3.2). Catalysts are quantitatively compared by their amine site-specific activity. Due to the ambiguity in exact primary amine

availability, site time yields (STYs) are reported rather than turnover frequencies (TOFs). To calculate STYs, the rate of reaction in the approximately linear low-time reactant conversion (typically 0.5 or 1 h) regime, up to a conversion of 10–20 %, was normalized by the mol % catalyst from the total diamine content. As such, STYs represent a lower bound for site-specific initial rates as the available primary amines would be less than or equal to the theoretical content determined by elemental analysis.

The active site loading is defined only by the amine (base) content, but the aldol condensation is most effectively catalyzed by an acid–base cooperative mechanism (Figure B.8).[113,117,120] Acid–base active sites may consist of an amine species with one or more proximal acids, depending on the material. As propyl-linked primary amines are the base species present in all materials studied herein, the relative catalytic function of reported catalysts is determined primarily by the type, abundance, and positioning of cooperative acid partners. The ratio of free primary amines to the theoretical value used in mol % calculations is another key factor. Surface silanols and grafted carboxylic acids, if present, are the weakly acidic species available in the silica-supported materials. Surface hydroxyls, sulfate half-esters, and carboxylic acids are the acidic species present in CNC-based organocatalysts. The effectiveness of these various acidic species in cooperative catalysis will be discussed in the context of the catalyst series investigated.

CNC catalysts are synthesized and stored as homogeneous suspensions of individual or small agglomerates of CNCs and are not well-defined porous or solid materials like the mesoporous silica organocatalysts routinely studied for this aldol reaction. Reactions were performed in suspensions of CNC particles that were partially agglomerated in the organic cosolvent mixture. The operando CNC agglomerate form and

size are not well-defined, but Mears' criterion and Weisz-Prater parameter calculations based on reasonable assumptions were performed to determine the potential for limiting transport effects. For both CNC and SBA-15 catalysts, external and internal transport limitations were negligible (Table B-1 and Table B-2). Additionally, carboxylated CNC samples, prior to amine functionalization, have no discernible activity for the aldol condensation under the conditions used herein (Figure B.9).

The effect of the extent of initial removal of sulfate half-esters in CNC catalysts on catalytic activity is shown in Figure 3.4. This comparison is made across catalysts that were identically synthesized apart from their SE content. With SE content as the primary differentiator, it was found that the partially desulfated (ds) catalyst had the greatest activity. Sulfate half-esters are more strongly acidic and bulkier than carboxylic acid groups created by hydroxyl oxidation. As partial sulfate removal increased activity, SEs may not be effective participants in aldol condensation catalysis utilizing cooperative proximal acid and base sites. Examples of aminosilica acid–base catalysts for aldol condensations in literature have shown that strong acids are generally less effective cooperative partners.[113] Sulfate half-esters may also interact too strongly with nearby primary amines and act to poison base sites, whereas weaker and more regularly spaced carboxylic acids may not.[121]

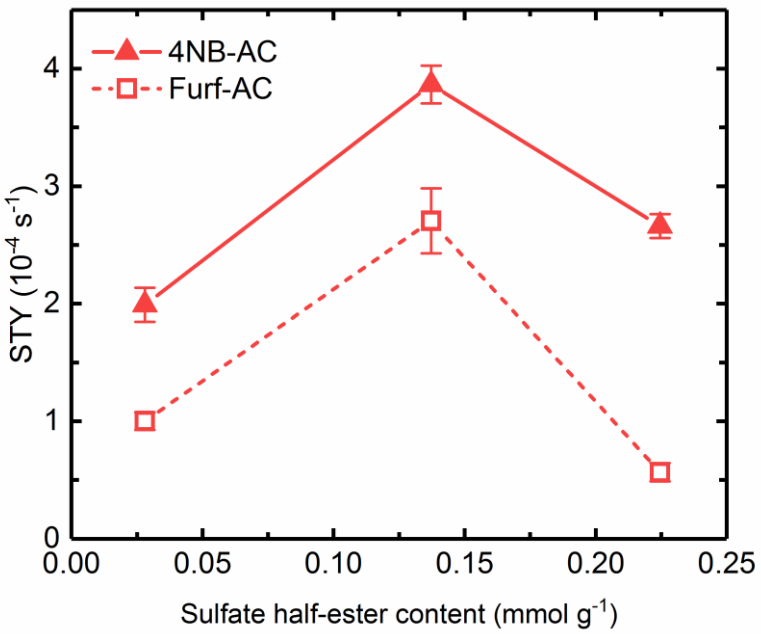

Figure 3.4 – Effect of SE content on initial aldol condensation reaction rates for reactions of 4-nitrobenzaldehyde (4NB) and furfural (furf). The catalysts compared here (CNC-s-, CNC-ds-, CNC-DS-cooh-dbDAP) are similar with respect to surface chemistry characteristics except in SE content (Table 3-1).

However, near-complete removal of SEs does not further increase activity. Sulfate half-esters are known to be critical for CNC dispersion and for maintenance of stable suspensions. As surface charge decreases with SE removal, electrostatic repulsion decreases and CNCs may irreversibly agglomerate, evidence of which was seen in the stark increase in opacity and viscosity after significant desulfation. Dynamic light scattering of CNC starting materials with varying degrees of sulfate half-ester removal as well as the catalysts compared here indicate that significant desulfation causes particle agglomeration (Figure B.10). SE groups may not be effective for catalysis, but their presence may be critical for synthesizing well dispersed and highly accessible CNCs. Notably, the highly desulfated (DS) material resulted in the lowest amide coupling conversion across all CNC materials studied. Given these disparities, highly desulfated catalysts are likely limited by

agglomeration, transport, and/or functionalization, and may not be useful for further fundamental comparisons of surface chemistry effects on catalysis.

CNC catalysts were also synthesized with differing extents of oxidation. Investigations of heterogeneous organocatalytic aldol condensations have shown some base-only activity,[128] however activity is significantly increased by the presence of cooperative weak acids. Proposed mechanisms suggest acids primarily activate relevant carbonyls, like the ketone of acetone or the aldehyde of the, here, limiting reactant (4NB or furf) (Figure B.8). In addition to absolute differences in final carboxylic acid content, significant variation in acid/base ($COOH:NH_2$) ratio is noted across CNC catalysts synthesized (Table 3-1). The cooperative nature of the catalysis suggests that acid-base site pairing is a critical metric. Indeed, this has been studied in aminosilica acid–base catalysts.[128] The site-specific activities of all $COOH/NH_2$ catalysts were thus compared as a function of their $COOH:NH_2$ (acid/base) ratio in Figure 3.5.

Base-normalized activity (STY) was found to be correlated with catalyst acid/base ratio. High SE content was shown above to reduce catalytic activity, and surface hydroxyls are abundant (> 2.5 mmol OH/g) relative to carboxylic acids, which would reduce the strong correlation in activity with COOH content if these hydroxyl groups (pK_a 10–14[169]) were cooperatively effective. As such, this correlation suggests that carboxylic acids are the primary cooperative acid species in the CNC-based catalysts. In addition, DAP-based CNC catalysts are shown to be markedly more active than analogous dbDAP catalysts across a range of acid/base ratios (Figure 3.5). Theoretically, if amidation with DAP resulted in no two-site cross-linking and bocDAP materials were completely deprotected, then the two syntheses would produce identical materials. However, the inferior activity

found in dbDAP catalysts indicates that the issue of incomplete deprotection more significantly reduced active site availability than diamide formation in DAP catalysts (Figure 3.1).

The dbDAP catalysts generally had greater acid/base ratios, as hydrothermal deprotection reduced the total amine loading and liberated additional carboxylic acid groups. However, even at a relatively low acid/base ratio (0.6), CNC-ds-COOH-DAP had greater activity than the best dbDAP catalyst, CNC-ds-COOH-dbDAP, which had an acid/base ratio of 1.5. The extent of diamide formation and reduction in free amine availability may be quite minor, as the CNC cross-linking resulting from similar DAP functionalization studied in our previous work was not significant.[138] Still, both dbDAP and DAP catalysts showed a strong positive correlation in STY with acid/base ratio (Figure 3.5).

The best performing CNC catalyst, CNC-ds-COOH-DAP-HT, combines all the elements found in this study to be beneficial for catalysis. While there were no boc protecting groups to remove, the hydrothermal treatment hydrolyzed some of the amide bonds. This reduced total amine content, increased residual COOH loading, increased the COOH:NH_2 ratio, and likely reduced the number of diamide-coupled DAP molecules. This material also featured partially reduced sulfate half-ester content, shown earlier to be optimal among the conditions tested. These attributes afforded a STY for the aldol condensation of 4NB of $10.\times10^{-4}$ s^{-1}.

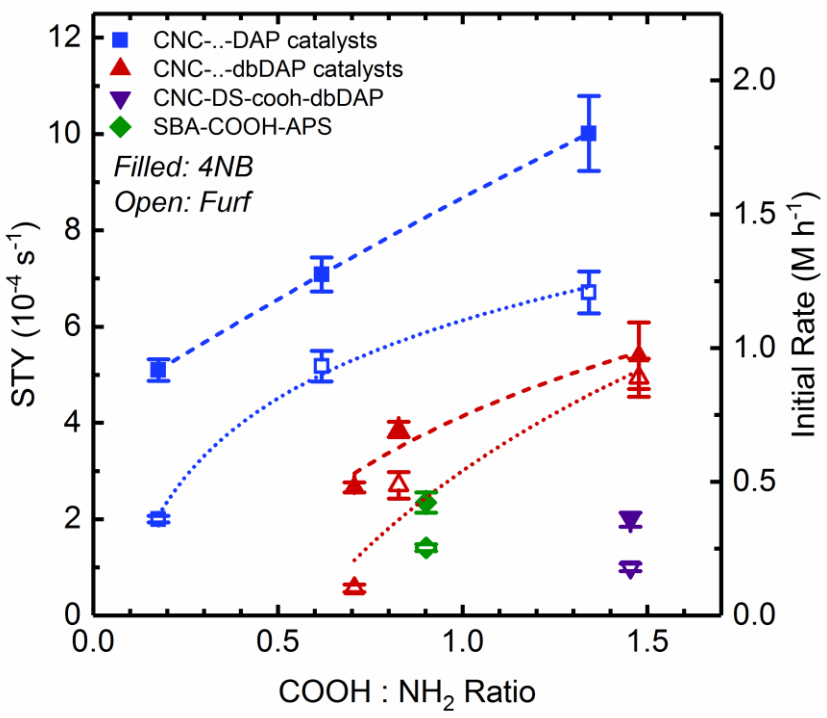

Figure 3.5 – Base site-normalized catalytic activities of COOH-containing acid–base organocatalysts as a function of COOH:NH_2 ratio in aldol condensation reactions of 4NB (filled symbols) or furfural (open symbols) with acetone. Trends in STY with activity are shown for catalyst types (DAP and dbDAP) and each aldehyde substrate. The SBA-15-supported COOH/NH_2 catalyst (SBA-COOH-APS) is included for comparison. The highly desulfated CNC catalyst (purple) is included for reference but does not fit the trend found for the other deprotected bocDAP catalysts (dbDAP, red).

As seen in Figure 3.5, catalytic activity was greater for aldol condensations of 4-nitrobenzaldehyde than for furfural, both with acetone, for almost all catalysts studied. 4NB is often used as a model reactant for AC reactions with acid–base organocatalysts as it is activated by the electron-withdrawing *para* nitro substituent. Furfural is not similarly activated with an EWG substituent. For both substrates, similar trends in activity with catalyst acid/base ratio were found. The catalysts in this study have moderate acid/base ratios, mostly between 0.5 and 1.5. An increase in acid/base ratio would indicate an increased availability of cooperative acidic functionality for base sites. In base-normalized

activity, this increase in acid availability increases the likelihood of a substrate to be activated in the proximity of an active base site. At high enough acid/base ratios, a maximum number of proximal carboxylic acid species for each amine site would be reached and further increasing this ratio would not further increase base-specific activity. The catalysts in this study do not reach this limit, but this effect has been demonstrated in aminosilica organocatalysts.[128]

For randomly spaced and appropriately dense surface functionalization, an acid/base ratio around one would lead to effective site-pairing and cooperativity while maximizing the availability of total acid–base pairs. Representations of an idealized CNC catalyst including acid–base spacing and pairing are shown in Figure 3.6. At very high acid/base ratios, base site-specific activity may reach a maximum but overall catalyst active site loading would be necessarily lower. The highly desulfated catalyst discussed earlier does not fit in the trends that are apparent across the rest of the materials studied (Figure 3.5). This is additional evidence that excessive desulfation introduces confounding catalyst limitations, such as agglomeration, that reduce activity and prevent fundamental investigation of catalyst activity.

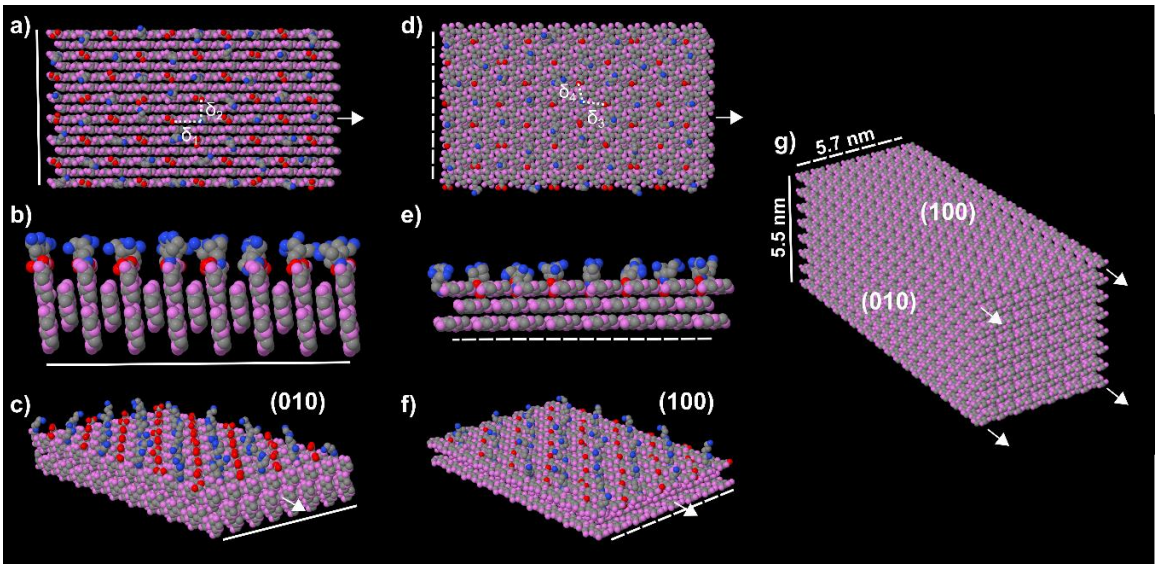

Figure 3.6 – Spatial positioning and structure of carboxylic acid (red) and amine (blue) surface species for the two crystalline faces present in the cellulose Iβ structure of wood-derived cellulose nanocrystals. Oxygen atoms not in carboxylic acid species are shown in pink, and carbon atoms are gray. In all depictions, hydrogen atoms are omitted to reduce clutter, and SE content is omitted for simplicity. Theoretical DAP-functionalized CNC surfaces with complete initial oxidation of C6 hydroxyls, 1:1 COOH:NH_2 ratios, and optimal checkerboard acid–base arrangements are represented. Crystallite widths were chosen to approximate a typical CNC cross-sectional size. Arrows indicate the truncated z-axis of the cellulose crystallite. (a–c) refer to the (010) surfaces and (d–f) to the (100) surfaces. (a,d) Top-down views of the (010) and (100) surfaces, respectively. δ_1 (010) and δ_3 (100) are representative NH_2–COOH distances along a single cellulose chain (intrachain), and δ_2 (010) and δ_4 (100) are representative interchain spacings. Average values for these distances with pseudorandomly oriented acid and base surface species are $\delta_1 = 10.6 \pm 2.2$ Å, $\delta_2 = 8.4 \pm 1.7$ Å, $\delta_3 = 11.0 \pm 2.3$ Å, and $\delta_4 = 9.3 \pm 1.8$ Å. (b,e) Z-axis (into the page) views of the first three layers of the catalyst surface with end functionalities ignored. (c,f) Angled surface perspectives of the two catalyst surfaces. (g) A full crystallite cross-section (z-truncated, omitting chiral twist) of an unfunctionalized CNC.

3.3.4 Product Selectivity and Comparisons Between CNC vs. SBA-15 Organocatalysts

The CNC-based organocatalysts developed in this work were compared to SBA-15-supported aminosilica catalysts with analogous surface chemistry: propyl-linked primary amines and a cooperative weak acid, either surface silanols (SBA-APS) or cografted silanes with a carboxylic acid moiety (SBA-COOH-APS). The SBA-APS

catalyst used is more similar to the current state-of-the-art within this material class,[23,188] but the SBA-COOH-APS catalyst was also included as a more direct analogue in terms of surface chemistry.[111]

Under the reaction conditions used in this study, the best-performing CNC catalyst had slightly greater site-specific activity for the aldol condensations of 4NB and furfural than the well-optimized SBA-APS catalyst (Figure 3.7). As expected from previously reported findings,[111] SBA-COOH-APS demonstrated significantly reduced activity compared to SBA-APS. It has been shown that surface silanols are particularly effective cooperative weak acids in simple aminosilane-functionalized silica-supported organocatalysts.[127] This is due to their low acid strength ($pK_a \approx 4.5–8.5$[111]), which prevents strong poisoning interactions with grafted amines, and to their high relative availability, leading to high acid/base ratios. For isolated grafted aminosilanes on silicate surfaces, they are effectively surrounded by cooperative weak acid sites, maximizing their site-specific activities. However, the referenced work that investigated cografted carboxylic acid silanes[111] concluded that ineffective dispersion and site pairing as well as strong acid–base interactions led to the low activity measured.

The CNC catalysts studied could have suffered from similar limitations as they contain nearly identical acid and base moieties to SBA-COOH-APS. However, base site-specific activities greater than those of site-isolated aminosilanes grafted on SBA-15 (SBA-APS) with plentiful cooperative silanols were achieved. This suggests that effective bifunctional acid–base cooperativity between a carboxylic acid and a primary amine may be possible, but that the synthetic approach and material characteristics of the SBA-15 catalysts hinder this outcome. Moreover, the CNC acid–base catalysts do not appear to

have reached their maximum activity, as the data in Figure 3.5 suggest that further increasing the acid/base ratio could yield additional improvements to site-specific activity. This effective COOH–NH_2 acid–base cooperativity counters the findings of previous studies of aminosilica catalysts concluding that silanols are inherently superior cooperative acids than carboxylic acids.[111,121] This conclusion was also based on AC reactions of the model substrate 4NB and did not consider product selectivity, only catalytic activity calculated from initial rates.

The catalysts were also evaluated for their selectivity to the AC dehydration product (**2**, Figure 3.3) after the 6 h reaction period. Simple aminosilica organocatalysts like SBA-APS typically show low selectivity to the dehydration product, with the major product being the aldol product **1**. CNC catalysts investigated showed high selectivity, typically >80 %, toward the dehydration product in reactions of 4NB and furfural across all materials (Figure 3.7, Table B-3), significantly greater than the selectivities of the SBA-15 catalysts in reactions of 4NB. SBA-APS contains only weakly acidic silanols, while the CNC acid–base catalysts synthesized have a significant surface loading of stronger carboxylic acids ($pK_a \approx 4$). The availability of these stronger acids likely facilitates the acid-catalyzed dehydration of **1** to **2**, leading to the selectivity results observed. In CNC catalysts with poorer activities, with which reactant conversions after 6 h were relatively low, selectivities to **2** remained high. Selectivities were fairly consistent across all CNC materials, despite the wide range of reactant conversions in the 6 h product mixtures for various catalysts. This indicates a rapid dehydration of **1** to **2**, even at low concentrations of the aldol product **1**. Time-resolved reaction selectivity was determined from scaled reactions with the optimized CNC catalyst (CNC-ds-COOH-DAP-HT) and SBA-APS (Figure B.11).

Selectivity to **2** was approximately constant over the 6 h reaction for both materials, indicating that the reaction selectivity is an intrinsic property of the catalyst and reaction environment and not of the reaction time or procession. Even at low initial conversions, the CNC catalyst achieved close to 90 % selectivity supporting the claim of rapid dehydration.

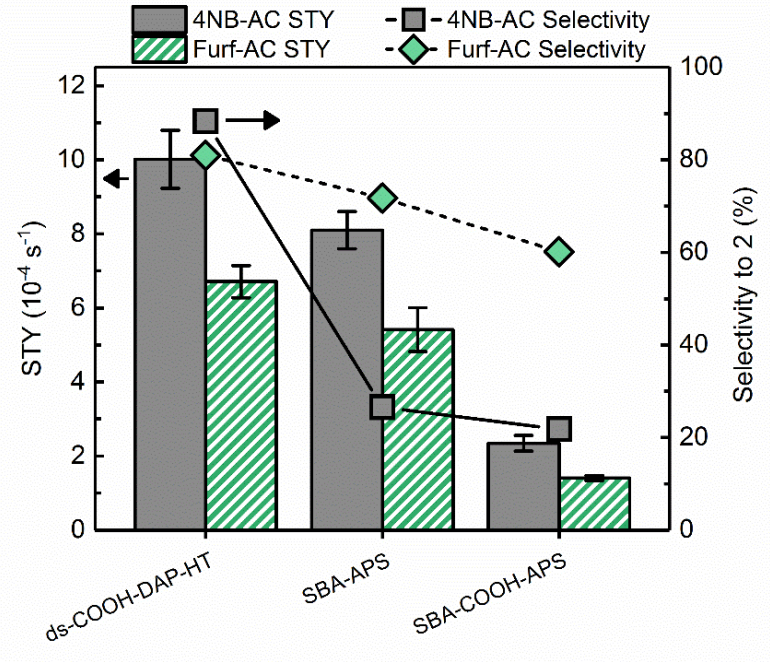

Figure 3.7 – A comparison of the optimized CNC acid–base catalyst with silica-supported analogues by selectivity to the dehydration product and initial rates in aldol condensation reactions of 4NB and furfural.

Despite generally reduced activities for the aldol condensation of furfural relative to 4NB, selectivities to the dehydration product in these reactions were higher than for 4NB. These data suggest that the aldol intermediate **1** of furfural is less stable and more prone to subsequent dehydration. SBA-APS, which lacks the stronger carboxylic acids apparently useful for this step in 4NB-AC reactions, was almost 80% selective to the dehydration product. For applications in biomass valorization, deoxygenation through

dehydration is advantageous in transformations of furfural toward hydrocarbons like fuel additives. As such, improving activity of the initial and crossed-aldol condensation steps is a more important direction for catalyst optimization.

Notably, the selectivity to **2** achieved in 4NB-AC reactions with SBA-COOH-APS was similar to that of SBA-APS, despite the presence of carboxylic acids. This may be due to the strong COOH–NH_2 interactions resulting from random placement and proximity of acid- and base-functional silanes (Figure B.7). At total silane loadings of ~0.8 mmol g^{-1}, grafted silanes will likely not be well isolated due to their spatial density as investigated in other works.[123,126,187] Random grafting and poisoning due to strong acid–base interactions[121] are significant factors in both the low conversion and dehydration activity of SBA-COOH-APS. The CNC-based catalysts presented also incorporate carboxylic acids and primary amines, but they are capable of effective cooperative catalysis as demonstrated by their competitive activity and high selectivity to the dehydration product. Postsynthetic modification of SBA-15 or other silicas by silane grafting is an effective but uncontrolled functionalization approach with respect to active site placement and proximity due to the nature of the random grafting over the amorphous silica surface area.[114,123,124,126]

Cellulose nanocrystals, in contrast, are crystalline in nature and have regularly ordered surfaces.[30,158,161] The wood-derived CNCs used in this study are in the form of cellulose Iβ which features two exposed crystal planes: *(010)* and *(100)*.[183] TEMPO-mediated oxidation selectivity oxidizes only C6 hydroxyl groups, which are present with regular spacing and positioning on CNC surfaces (Figure 3.7a, d). Amine-functionalization through amidation also occurs at these C6 sites, as they are grafted to the surface through reactions of these ordered carboxylic acids. There is some evidence against clustering of

amine moieties on CNC surfaces, suggesting amidation may occur at random acid sites on CNC surfaces. For example, there is an apparent limit in COOH conversion to amides despite use of a significant excess DAP or bocDAP during functionalization. A simple electrostatic argument of charge repulsion would be consistent with more regularly spaced amine sites.

As seen in Figure 3.6, the relative positioning of acid and base species on functionalized CNC surfaces differs for the two exposed crystallographic faces (a–c vs d–f); however, COOH–NH_2 spacing appears sufficient such that direct acid–base quenching is unlikely while proximity and ordering are favorable for cooperativity. Inter- and intrachain acid to base spacings for both crystal faces appear too great for direct interaction but within the range necessary for cooperative activity (Figure 3.6a, d; Figure B.13). This precise spacing supports our previous findings wherein CNC catalysts functionalized with shorter (ethylenediamine) and longer (hexamethylenediamine) diamines were significantly less active than DAP materials due to limited cooperativity and increased diamide cross-linking, respectively.[138] The ordered nature of the CNC surfaces highlights a particular advantage for developing bifunctional cooperativity on these materials that is not feasible in typical silane grafting functionalization approaches common in silica-supported organocatalysts. This surface order and enhanced cooperativity is likely a key factor in the superior catalytic activity actualized in optimized CNC acid–base catalysts, as well as in the incorporation of two relatively strong acid/base species that would otherwise quench and poison active sites without precise relative positioning.

3.4 Conclusions

The surface chemistry of cellulose nanocrystal-supported acid–base heterogeneous cooperative organocatalysts was investigated and optimized. CNCs are presented as an alternative support to well-studied mesoporous oxides for acid–base organocatalysis. Key surface species (sulfate half-esters, carboxylic acids, and primary amines) were quantitatively varied to probe their impact on catalytic performance. Partially reduced sulfate half-ester content was determined to be optimal as such species do not improve catalysis but are important for CNC dispersion and functionalization. Catalysts synthesized with initially protected diamines were hindered by incomplete deprotection, and unprotected DAP functionalization was minimally affected by cross-linking due to the choice of appropriate diamine length and native acid spacing on the oxidized CNC surface.

The CNC organocatalysts' site time yields were strongly correlated with COOH:NH_2 ratio. Carboxylic acids functioned as effective acid cooperative partners to the primary amine moieties, whereas surface hydroxyls were present in high densities but appeared ineffective. Full initial oxidation and partial hydrothermal rehydrolysis of amides yielded optimized CNC catalysts with a high acid/base ratio. CNC catalysts were active for furfural upgrading by aldol condensation with acetone; high selectivities to dehydration products were achieved due to fast dehydration of the aldol intermediate by carboxylic acid sites. Optimized CNC catalysts outperformed both analogous SBA-15-supported catalysts in activity and selectivity. The inherent order of crystalline cellulose surfaces and the selective surface oxidation are ideal templates for the precise design of cooperative

catalysts. CNC surface structure and functionalization approaches are appealing alternatives to amorphous oxide-supported organocatalysts which suffer from limitations in multifunctional design due to poorly controlled silane grafting.

CHAPTER 4. ACID–BASE FUNCTIONALIZED CELLULOSE NANOFIBRIL AEROGELS AS POROUS SOLID COOPERATIVE ORGANOCATALYSTS

4.1 Introduction

Aerogels are a unique class of materials characterized by high surface area and porosity and remarkably low densities.[75,189] These ultralight structures are commonly composed of silica, ceramics, polymers, and, more recently, cellulose and are used in applications such as insulation, adsorption, electronics, bioengineering, and templating.[75] Cellulose and cellulose nanomaterials (CNMs) are being widely studied as a scalable and renewable basis for advanced materials.[11,12,181] Cellulose nanomaterials are semi-crystalline, high aspect ratio fibers of cellulose with nanoscale widths.[3] Well-dispersed CNMs and other precursors readily form aerogels through ice-templating and freeze drying.[52,54,190,191] CNM hydrogels and aerogels have been fairly widely reviewed in their production and applications,[16,43,76] which non-exhaustively include tissue engineering,[76,192] electronics,[62,193] separations,[83,85–87,194] insulation,[64] and reinforcement.[195]

A growing use of CNMs is as catalyst supports.[88] Most examples to date of CNMs in catalysis are as supports for noble metal nanoparticles (NPs). These supported metal catalysts have been used for various test reactions, such as reductions with Au,[40,93] hydrogenations with Pd,[41] and asymmetric additions with Rh.[94] Much of the current literature focuses on reactions with catalyst CNMs homogeneously dispersed in a solvent, often water, but applications in catalysis with CNM-based aerogels are now gaining

interest. Early work by Kuga et al produced Ag, Au, and Pt NPs supported on cellulose aerogels,[96] but they were not explicitly used for catalysis. Polydopamine-functionalized aerogels were used to support Pd NPs for Suzuki and Heck cross-coupling reactions with minimal leeching.[100] Aerogel-supported Au NPs have been demonstrated for styrene epoxidation.[97] In line with the abundance of studies utilizing CNM aerogels for adsorptive separations of metals and organic compounds, Ag- and CuS- functionalized aerogels were used for catalytic degradation of organic dyes by Fenton reactions.[98,99]

With the expanding field of supported organocatalysis,[109] some researchers have been investigating the use of catalytic organic acid and/or base functionality in CNMs. Oxidized CNMs with carboxylic acid moieties have been used as acid catalysts,[105,106] and our previous works have investigated and optimized acid–base bifunctional cellulose nanocrystals as cooperative organocatalysts for aldol condensation reactions.[138,170] Nanofibrillar chitin, structurally similar to cellulose but with natural amine functionality, has been used as a base catalyst in its aerogel form for the Knoevenagel condensation.[154] Further investigation of CNM aerogel catalysts is key to the development of real-world applications, as CNMs would most likely to be implemented as porous solid catalysts.

In this study, we develop synthetic and processing methods to produce acid–base aerogel organocatalysts from cellulose nanofibrils (CNF). Our prior studies in this area outlined the advantageous properties of CNC-based cooperative catalysts,[170] and the work presented here moves these materials toward application by advancing to the solid phase with aerogel-based catalysts. Mechanically and chemically robust CNM aerogels are often produced with the aid of chemical or physical cross-linkers.[43,55] Small molecules cross-linking with facile or spontaneous reactions,[50,196] polymeric cross-linking with UV-

inducible polymerizations,[46,197] and physical cross-linking with non-covalent fillers[47,198] have been demonstrated as effective approaches for the production of robust CNM aerogels.

Herein, we investigate multiple functionalization and processing approaches to the production of robust acid–base organocatalyst CNF aerogels. The optimized catalytic functionality which we have previously reported in cellulose nanocrystals, incorporating acid and base sites through TEMPO-mediated oxidation and diamine amide coupling,[138,170] is here used as the basis for catalytic function in cellulose nanofibrils. TEMPO-oxidized CNFs (TOCNFs) modified for catalysis are subsequently covalently cross-linked with small molecules or physically reinforced with carboxymethylcellulose as an additive. TOCNFs are also functionalized and cross-linked with amine-dense poly(ethyleneimine). Effects of hydrogel solvent and functionalization on aerogel chemical and physical stability, pore structure, and catalytic activity are evaluated. CNF aerogel catalysts are compared to previously optimized homogeneous CNC catalysts in batch aldol condensation reactions.

4.2 Materials and Methods

4.2.1 TEMPO-Oxidized Cellulose Nanofibril Preparation and Titration

Microfibrillated cellulose (MFC) derived from mechanical treatment of bleached wood pulp, produced by the Forest Products Laboratory, was obtained through the University of Maine in ~ 3 wt% aqueous suspension. Fibrillated cellulose with nanoscale cross-sections was produced by TEMPO-mediated oxidation of the stock MFC followed by homogenization (Figure C.1). The widely-used TEMPO-mediated procedure[28] was

adapted to oxidize MFC (8 g, dry basis). To an aqueous suspension of MFC, NaClO (73 mL, 11–15% active Cl, Alfa Aesar), (2,2,6,6-tetramethylpiperidin-1-yl)-oxyl (TEMPO, 0.8 g, 98%, Sigma-Aldrich), and NaBr (8 g) were added with additional deionized (DI) water to achieve ~ 2 wt% MFC. The pH was maintained at 10–11, and the mixture was stirred at room temperature for four hours before collection and washing with NaCl (0.5 M), HCl (0.1 M), and deionized water by repeated centrifugation. The washed product was finally dialyzed to yield TEMPO-oxidized MFC (TOMFC).

All of the TOFMC was diluted to 0.1 wt% in DI water and homogenized with a Mini DeBEE Homogenizer (BEE International) at ~ 1000 bar (1000 psi oil pressure) with a total of ten passes (Figure 4.1). The opacity of the suspension significantly decreased with homogenization. The homogenized TOFMC was concentrated by ultrafiltration and collected as a viscous suspension (1.9 wt%). The resulting material is termed TEMPO-oxidized cellulose nanofibrils (TOCNF).

4.2.2 Material Storage and Freeze-drying Procedures

TOCNF and intermediate materials were stored at 4 °C in aqueous suspension. All TOCNF aerogels were freeze-dried for at least 48 h with a Labconco FreeZone freeze dryer (0.03 mbar, -105 °C collector) in 28 mm diameter glass vials (80 mL capacity). All aerogels were ultimately frozen directly prior to freeze-drying in liquid N_2 (LN_2), but processing before final freeze-drying varied. Unless otherwise specified, the final wt% of suspensions freeze-dried to aerogels was 1.5. Aerogels of TOCNF materials functionalized beyond oxidation were stored in septum-cap vials purged with Ar.

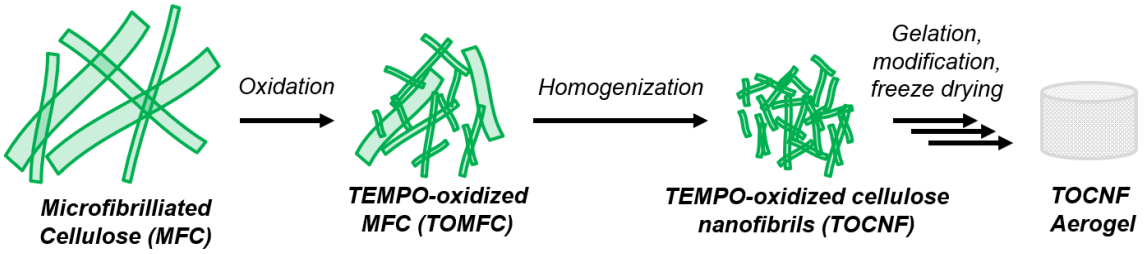

Figure 4.1 – General approach to preparation of TOCNF aerogels from MFC starting material.

4.2.3 Functionalization, Cross-linking, and Processing of TOCNF Aerogel Catalysts

TOCNF acid–base aerogel catalysts were produced with a variety of synthetic and processing approaches (Figure 4.2). Amine functionalization for acid–base cooperative catalysis was achieved using aqueous amide coupling of 1,3-diaminopropane (DAP, >99%, Sigma-Aldrich) to TOCNF surface carboxylic acids using a method similar to those of our previously published works.[138,170] TOCNF was functionalized with two differing quantities of DAP by controlling the equivalents of DAP with respect to carboxylic acid content. Briefly, 1-ethyl-3-(3-(dimethylamino)-propyl)carbodiimide hydrochloride (EDC, 2 equiv, >99%, Sigma-Aldrich), *n*-hydroxysuccinimide (NHS, 2 equiv, 98%, Sigma-Aldrich), and DAP (2 equiv or 5 equiv) were added to a 1 wt% suspension of TOCNF with stirring. Reaction mixture pH was adjusted to between 7.5 and 8, and the reactions were stirred overnight prior to purification by dialysis. The two resulting DAP-functionalized materials are referred to as TOCNF-DAP (two equiv) and TOCNF-DAP2 (five equiv).

One approach to the production of cross-linked TOCNF catalyst aerogels utilized terephthalaldehyde (TPA, 99%, Sigma-Aldrich) as a small molecule dialdehyde cross-linker. TOCNF-DAP was solvent exchanged via centrifugation and solvent replacement (four times) to mixtures of DI water/*tert*-butyl alcohol (tBA, >99%, Sigma-Aldrich) at 1:1

or 3:1 v%:v%. The suspensions were vortexed and bath sonicated after solvent exchange. A quantity of TPA (0.1 equiv with respect to DAP content of TOCNF-DAP) dissolved in 0.6 mL solvent was added to the suspension, and the final suspension (1.5 wt% TOCNF-DAP) was vortexed for one minute, allowed to sit for one additional minute, and then submerged in LN_2 for 15 minutes. The frozen suspensions were thawed in a refrigerator (4 °C) and then heated without stirring in an oil bath at 35 °C for 12 h. Finally, the resulting hydrogels were allowed to cool to RT and subsequently frozen again in LN_2 and freeze-dried. These aerogels are referred to as TOCNF-DAP-TPA_1-1 and TOCNF-DAP-TPA_3-1, respectively. Additionally, unmodified TOCNF samples were similarly solvent exchanged to 1:1 and 3:1 H_2O/tBA and freeze-died (TOCNF_1-1 and TOCNF_3-1).

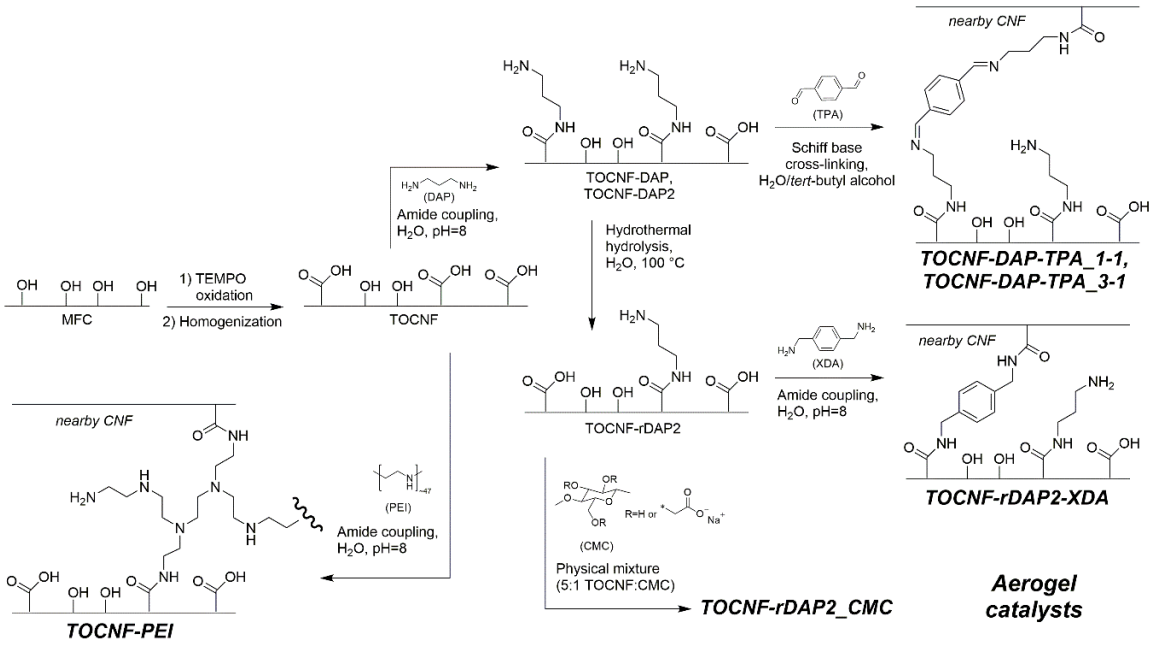

Figure 4.2 – Schematic of processing and chemical functionalization of TOCNF-based aerogel catalyst materials.

Adapting an approach developed in our previous work,[170] the DAP content of TOCNF-DAP2 and unfavorable diamide bonds were partially reduced by hydrothermal

hydrolysis. An aqueous suspension of TOCNF-DAP2 was diluted to 0.7 wt% in a round-bottom flask fitted with a reflux condenser and magnetically stirred at 100 °C for 4 h before being allowed to cool and dialyzed to remove cleaved DAP. This sample with reduced DAP content is referred to TOCNF-rDAP2. For further processing, portions of this sample were concentrated by centrifugation and removal of some excess water prior to redispersion with stirring and sonication. A sample of TOCNF-rDAP2 was freeze-dried without further modification from a 1.5 wt% suspension in water. Additionally, a sample of TOCNF-rDAP2 was mixed with an aqueous solution of high viscosity carboxymethylcellulose sodium salt (CMC, Sigma-Aldrich), thoroughly dispersed via stirring and sonication, and freeze-dried. The total dry content (TOCNF+CMC) of the suspension was 1.5 wt%, and the mass ratio of TOCNF:CMC was 5:1. This sample is referred to as TOCNF-rDAP2_CMC.

Two chemically cross-linked aerogels were produced via aqueous amide coupling. For one, a sample of TOCNF-rDAP2 was cross-linked with *p*-xylylenediamine (XDA, >99%, TCI). To a concentrated suspension of TOCNF-rDAP2, NHS and EDC dissolved in a small quantity of water were added (0.1 equiv with respect to residual carboxylic acid content, Table 4-1) and mixed thoroughly. Next, XDA (0.1 equiv, dissolved in a small quantity of water) and HCl (0.025 equiv, to adjust pH) were added via pipette. The suspension was vortexed for one minute to thoroughly mix the components prior to freezing in LN_2 and thawing at 4 °C. The thawed hydrogel was held at room temperature for 12 h and was then washed twice with 0.02 M HCl and once with DI water before freezing again in LN_2 and freeze-drying.

With similar processing, TOCNF was functionalized and cross-linked with branched poly(ethyleneimine) (PEI, 1800 Mw, 99%, Polysciences, Inc). EDC and NHS (2 equiv, dissolved in a small quantity of water) were added to an aqueous suspension of TOCNF and mixed thoroughly. The branched PEI used is specified by the supplier to possess 40% primary, 36% secondary, and 24% tertiary amines. A solution of PEI in water (2 equiv primary amines with respect to carboxylic acids in TOCNF) was added to the suspension along with HCl (0.5 equiv with respect to amines in PEI), and the suspension was vortexed for two minutes and allowed to sit briefly prior to freezing in LN_2. The frozen mixture was thawed at 4 °C and left at room temperature for 12 h prior to washing twice with 0.1 M HCl and once with DI water. Finally, it was frozen in LN_2 and freeze-dried.

4.2.4 Characterization of Modified TOCNF and Merogels

Conductometric titrations of 0.5 wt% suspensions of TOMFC and TOCNF from pH 3 to 11 were performed with NaOH (0.100 N). Both pH and conductivity were monitored during titration, and the roughly flat portion of the conductivity curve (pH ~ 4–8) was used to quantify carboxylic acid content resulting from oxidation. The elemental content (C H N) of samples was analyzed combustion elemental analysis (EA) as performed by Atlantic Microlab, Inc. Transmission Fourier transform-infrared (FT–IR) spectra of samples pelleted with KBr were collected with a Nicolet iS10 FT–IR Spectrometer. Thermogravimetric analysis (TGA) was performed with a Netzsch STA409 instrument. X-ray diffraction (XRD) patterns were obtained with an X'Pert Pro PANalytical X-ray diffractometer. Scanning electron microscopy (SEM) images of dropcast suspensions were collected with a ZEISS Ultra 60 FE-SEM, and images of aerogels were collected with a Hitachi SU-8230 FE-SEM. Aerogels were coated with 15–

20 nm Au by a Hummer Sputter System prior to SEM imaging. Aerogel densities were determined by caliper size measurements and gravimetry of aerogel sections.

4.2.5 Solvent Uptake Testing and Catalysis Experiments

Aerogel stability in water, toluene, and acetone solvents was evaluated. Small fragments of intact aerogels (5–15 mg) were weighed in 20 mL vials, to which 3 mL of solvent was carefully added, and initial observations were recorded. The samples were left undisturbed for 48 h after which aerogel redispersion was re-assessed. If possible, all excess solvent was removed via pipette and the solvent uptake of the swelled aerogel was measured gravimetrically.

Batch aldol condensation reactions of 4-nitrobenzaldehyde (4NB, 98%, Sigma-Aldrich) and acetone catalyzed by TOCNF acid–base materials were performed under nearly identical conditions to our previous work for direct comparison.[170] Reactions were performed at 60 °C in two-neck round-bottom flasks fitted with reflux condensers. DAP-functionalized aerogel precursors (TOCNF-DAP, TOCNF-DAP2) were solvent exchanged to 1:1 v%:v% acetone/acetonitrile as homogeneous dispersions, in line with the methodology developed in our previous works. Aerogel catalysts were dispersed in 3 mL acetone/acetonitrile with magnetic stirring at reaction temperature for 1 h prior to addition of 4NB and the internal standard, 1,4-dimethoxybenzene (>99%, TCI). All reactions were performed in 4 mL total of 1:1 acetone/acetonitrile with 50 mM each of the substrate (4NB) and internal standard. Reaction aliquots were removed by needle and syringe and analyzed by flame ionization detector with a Shimadzu gas chromatograph. After 4 h, the product mixture was recovered by filtration, concentrated by rotary evaporation, and analyzed via

^{1}H NMR in DMSO-d_6. Each reaction was performed with 10 mol% catalyst, with catalyst loading being defined by the active amine content of each material (Table 4-1). Active amine content was defined by the total loading of amine-containing molecules for each material. For TOCNF-PEI, the active amine content was defined by the available primary and secondary amines.

4.3 Results and Discussion

4.3.1 MFC Processing for Aerogel Production

The production of hydrogels and aerogels from cellulose-based materials is a complex art in which many factors influence the ultimate form and properties. A few key variables are the type of cellulose or cellulose nanomaterial, the suspension concentration and dispersion, the solvent, and the freezing conditions. While solvent, processing, and freezing may be readily standardized, the breadth of cellulose nanomaterial sources used in the formation of aerogels and hydrogels, and the unavoidable differences in fiber size and structure, dispersion, surface chemistry and more, results in a landscape where precise reproducibility is challenging. Nonetheless, certain general rules exist relating freezing and drying approaches, CNM size, dispersion, concentration, and surface charge to the resulting aerogel properties.[43]

Generally, a highly disperse suspension of flexible, high aspect ratio CNMs at a sufficiently high concentration will readily form a physical network upon ice-templating by freezing.[43,51,52] The starting material used herein is MFC mechanically produced from wood pulp, which consists of fibers far too large for effective network formation and hydrogelation. A high degree of oxidation (1.9 mmol COOH g^{-1}) is achieved with TEMPO-

mediated oxidation in mechanically mild conditions (magnetic stirring), indicating chemical penetration without significant fiber fibrillation. Strong subsequent mechanical treatment via homogenization was necessary to effectively fibrillate the TOMFC and achieve particle sizes amenable to hydrogelation. The resulting TOCNF fibers were well dispersed, nanoscale in width, and microns in length (Figure C.1). A simple freeze-thaw test (LN_2 freezing) was used to assess the stability of the hydrogel formed by ice-templated physical networking. The TOCNF produced herein formed stable, invertible hydrogels upon freeze-thawing at concentrations above roughly 1 wt% (Figure C.2).

TOCNF processing for aerogel formation was designed to maximize utility for catalysis, in which aerogel surface area is proportional to active catalyst site availability. Rapid freezing has been demonstrated to yield aerogels with finer pore structure due to increased ice nucleation resulting in smaller crystals during ice-templating.[53] Thus, LN_2 freezing was used for all aerogel samples. The TOCNF concentration in aerogel precursor suspensions was kept constant at 1.5 wt% to ensure network formation even if particle dispersion had decreased with functionalization and processing. Water was used as the solvent where possible, and mixtures of H_2O/*tert*-butyl alcohol were employed as a readily freeze-dryable co-solvent system when increased solvent hydrophobicity was necessary to dissolve chemicals used in TOCNF functionalization.

4.3.2 TOCNF Chemical Functionalization and Aerogel Production

Chemical and physical cross-linking of CNM aerogels is commonly utilized to improve mechanical properties.[16,43] Aerogels utilized for catalysis would generally be employed in a packed column flow reactor, where shear from gas or slow liquid flow would

not require significant mechanical strength but, in the case of liquid flow, would necessitate structural stability in the working solvent. Here, small molecule cross-linking of TOCNFs during aerogel formation was utilized to improve solvent stability. Small molecule cross-linking in CNM aerogels requires fiber proximity, i.e. fibers must be in physical contact or proximity for a covalent cross-link to form. It has been shown that covalent cross-linking during or after physical network formation, in particular with spontaneous bond-forming reactions, is an effective approach to small molecule CNM cross-linking.[50,84]

Functionalization and aerogel formation methods were designed such that small molecule covalent cross-linking occurred during or after physical TOCNF network formation by ice-templating in order to promote cross-linking functionalization at points of fiber-fiber contact. Aryl small molecules were utilized in cross-linking to prevent intra-fiber reactions, such as the diamide formation with a flexible diamines described in our previous work.[138] Generally, acid–base functionality was imparted to TOCNFs by modification in homogeneous suspensions. Our previous works developed CNC catalysts whose cooperative acid–base active sites were a proximal surface carboxylic acid and primary amine.[138,170] The same design utilizing oxidation and subsequent amide coupling with 1,3-diaminopropane (DAP) was employed here. Following initial functionalization, covalent cross-linking reactions were performed during or after ice-templated network formation by freezing.

Several approaches utilizing this design structure were used to produce TOCNF aerogel catalysts. One approach used Schiff base (imine) formation between primary amines on the TOCNF surface and an aryl dialdehyde cross-linker, terephthalaldehyde (TPA). Another used diamide formation using aqueous amide coupling of an aryl diamine

cross-linker, *p*-xylylenediamine (XDA), to residual TOCNF surface carboxylic acids. Additionally, a non-covalent filler, high viscosity CMC, was used to improve the aerogel properties of DAP-modified TOCNF. Finally, a significant degree of amine functionality was imparted to previously unmodified TOCNF by forming covalent cross-links by amide coupling with an amine-dense branched aminopolymer, poly(ethyleneimine), with an average molecular weight of 1,800 Da.

Mechanically produced MFC, unlike fibrillated cellulose produced with the aid of TEMPO oxidation or crystalline cellulose produced from sulfuric acid hydrolysis, has no native surface charge. TEMPO-mediated oxidation selectively oxidizes the accessible C6 position of the anhydroglucopyranose monomer of cellulose. By conductometric titration, oxidation produced 1.9 mmol COOH g^{-1} in TOMFC. This quantity is greater than the ~ 1.5 mmol g^{-1} maximum achieved in CNCs with widths of ~ 5 nm, indicating that there is some amorphous cellulose present in the samples. Amorphous cellulose, unlike crystalline regions, may be penetrated and oxidized beneath the nominal surface. The quantity of COOH measured in the same material after homogenization, TOCNF, was identical, indicating that homogenization solely acted to mechanically fibrillate and reduce the particle size of the cellulose (Figure C.1).

Intermediate and final materials were evaluated for their elemental content (C, H, and N) in order to determine extents of functionalization. Elemental content as well as estimations of residual active acid and base loadings are shown in Table 4-1. Previous studies have shown this approach as an effective means of quantifying catalytically active primary amines and residual carboxylic acid content in DAP-functionalized CNCs.[138,170]

For all materials functionalized beyond TEMPO-oxidation, the residual acid content is estimated assuming 1:1 consumption during amide formation with DAP.

In the synthesis of TOCNF-rDAP2-XDA, a low quantity of XDA cross-linker was added (0.2 equiv) which would at most marginally reduce the COOH content. To note, the final N content and amine loading of TOCNF-rDAP2-XDA was less than that of the pre-crosslinked material, TOCNF-rDAP2. This can be attributed to the washing of the cross-linked hydrogel with dilute HCl, which likely hydrolyzed some of the amide bonds (DAP and XDA). A method for quantification of the conversion of carboxylic acids was not discerned for the PEI-functionalized sample, as the total quantity of amines in the PEI added exceeded the total carboxylic acid content. The active amine content was estimated as the total number of primary and secondary amines (76% primary or secondary) in the quantity of PEI contained in the material. Primary and secondary amines have been demonstrated as active basic species for the catalysis of interest.[117]

Table 4-1 – Elemental, carboxylic acid, and amine contents of functionalized TOCNF samples as determined by elemental analysis and conductometric titration

sample	C content (wt %)	H content (wt %)	N content (wt %)	COOH loading[a] (mmol g^{-1})	active amine loading[b] (mmol g^{-1})
TOCNF	40.3	5.81	-	1.9	-
TOCNF-DAP	41.2	6.51	2.74	*0.92*	0.98
TOCNF-DAP-TPA_1-1	41.7	6.48	2.36	*1.06*	*0.84*
TOCNF-DAP-TPA_3-1	41.5	6.45	2.33	*1.07*	*0.83*
TOCNF-DAP2	41.3	6.53	4.06	*0.45*	1.45
TOCNF-rDAP2	40.4	6.25	2.16	*1.13*	0.77
TOCNF-rDAP2_CMC	39.7	6.11	1.26	*0.66*	0.45
TOCNF-rDAP2-XDA	40.4	6.07	1.54	*1.35*	*0.55*
TOCNF-PEI	36.9	7.48	11.14	undetermined	4.6[c]

[a]COOH content of TOCNF was determined by conductometric titration. All other values (italicized) were estimated assuming a 1:1 consumption per amide-linked amine molecule, resulting in a *maximum* COOH loading. This estimation is not viable for the PEI-functionalized sample.
[b]Active amine loading assumes one active $–NH_2$ per diamine molecule present. In TPA-cross-linked samples, up to 20% may be consumed to form Schiff bases (0.1 equiv dialdehyde introduced). With XDA, the reduction in total N content hinders estimation of DAP vs. XDA functionalization, thus the active amine loading is a maximum; true active amine could be as low as zero.
[c]For TOCNF-PEI, the active amine loading was estimated from the total NH + NH_2 content of the total PEI loading.

FT–IR spectroscopy was used to qualitatively verify the success of surface functionalization and the presence of intended chemistries. Full spectra and expanded IR region of interest, from 1450–1850 cm^{-1}, are presented in Figure 4.3. Interpretation of unmodified, TEMPO-oxidized, and diamine-functionalized (including DAP) CNCs has

been detailed in our and other previous works.[138,170] TEMPO-oxidation yields a strong C=O stretching peak at 1740 cm^{-1} in TOCNF. Upon amide-coupling, IR modes at ~ 1650 cm^{-1} for amide I (amide C=O stretching) and at ~ 1600 cm^{-1} for NH bending of free primary and secondary amines appear. The spectra for TOCNF-DAP and TOCNF-rDAP2 are quite similar and in line with previously reported spectra. The highly DAP-functionalized sample, TOCNF-DAP2, displayed additional intensity in the region of amide I and NH response prior to hydrothermal reduction of DAP content.

Evidence of effective functionalization with TPA in the spectra of TOCNF-DAP cross-linked as such was most clearly found in the reduction of the NH bending mode at 1600 cm^{-1}, as free primary amine content is reduced with Schiff base cross-linking, and in the small but sharp aldehyde C=O stretch ~ 1700 cm^{-1}. Residual aldehyde content indicates that not all TPA was fully cross-linked, but it confirms the successful incorporation of TPA. The major relevant significant Schiff base stretch (1660 cm^{-1}) unfortunately overlaps with the strong amide I mode, and aromatic C–H stretching bands (3000–3100 cm^{-1}) are indistinguishable in the strong IR signal from the cellulose bulk structure.

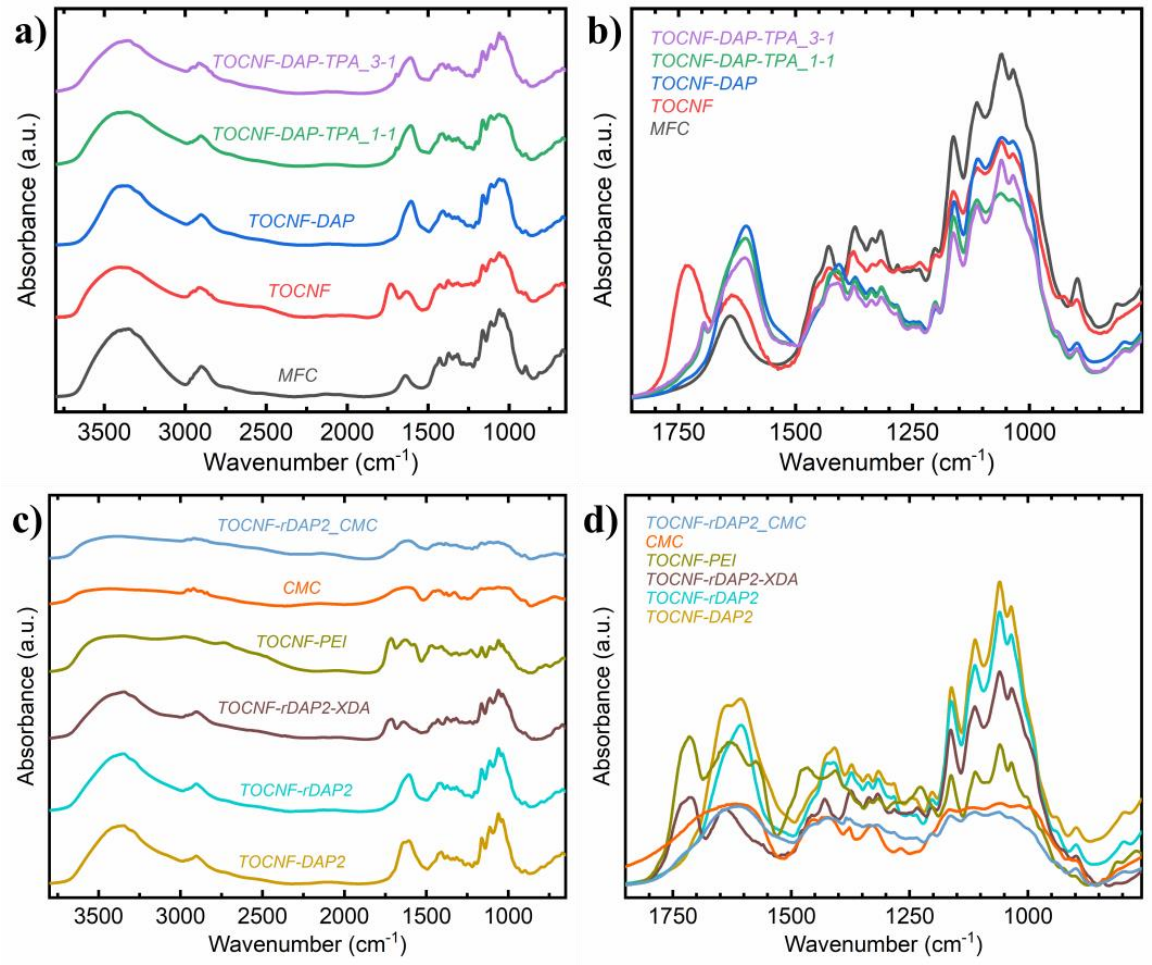

Figure 4.3 – Transmission FT–IR spectra of all samples. (a,c) Full spectra with arbitrary offset. (b,d) Spectra in the range of interest for chemical functionalization, overlaid without offset for facile comparison.

As discussed above for TOCNF-rDAP2-XDA, significant cleavage of amide bonds with the weakly acidic washing altered the intended surface chemistry. The acidic wash fully protonated residual acid content, which is seen as a reappearance of the C=O carboxylic acid stretch at 1735 cm^{-1}. The amide I peak is present at a low intensity, and there is insignificant evidence of the free amine NH bending. This may be in part attributed to successful diamide cross-linking of XDA. As with TPA cross-linked samples, any aromatic IR evidence is buried in the strong absorbance by cellulose. In PEI-functionalized

TOCNF, the carboxylic acid C=O peak at 1735 cm^{-1} is present, indicative of relatively low amidation despite the excess total amine content. Peaks attributed to PEI occur at 1630 and 1570 cm^{-1} (amide and amine groups)[199] and 1460 cm^{-1} (C-H bending).[194] Qualitative FT–IR analysis confirms the success of each of the functionalization chemistries utilized in sample synthesis herein.

4.3.3 Aerogel Structure and Porosity

The structure, appearance, and stability of the cross-linked and control aerogels were analyzed. Most aerogels formed somewhat brittle white structures which could generally be readily handled. The DAP-functionalized TOCNF freeze-dried without cross-linking, TOCNF-rDAP2, was the least mechanically robust and collapsed as a powder with moderate mechanical disturbance. This same material physically mixed with CMC formed the most mechanically robust aerogel, TOCNF-rDAP2_CMC. The only material to exhibit notable shrinking upon freeze-drying was TOCNF-PEI, which likely over-agglomerated with strong interactions between PEI and the TOCNF.

The pore structure of the aerogels was strongly affected by the chemical functionalization and suspension solvent. Representative SEM images of all functionalized and control aerogels are depicted in Figure 4.4. Measured aerogel densities and solvent stability are reported in Table 4-2. Unmodified TOCNF freeze-dried at 1.5 wt% from water may be taken as a baseline structure to which to compare in order to understand the effects of solvent, processing, and cross-linking. The TOCNF aerogel exhibited macroporous structure with fibers compressed into thin, connected sheets. There is some anisotropy in pore structure, which may be attributed to the rapid radial cooling experienced during

freezing (cylindrical vials were vertically plunged into LN_2). The TOCNF aerogel has a density of 26 ± 2 mg cm^{-3}.

The bulk density of an aerogel material that is freeze-dried without constriction or other volume change is primarily determined by the suspension wt% and solvent which determine the mass per volume of the liquid suspension. As all aerogels studied here were produced at roughly 1.5 wt%, and the resulting density of most materials was quite similar (20–40 mg cm^{-3}). Lower bulk densities have been achieved in cellulose aerogel literature,[61,200] but these low density materials require very small TOCNF particle size, perfect dispersion, and suspensions of much lower wt% solids. An effective aerogel catalyst does not require an extraordinarily low density, rather the major design goals are to optimize aerogel surface area to maximize accessible active sites, optimize pore structure to minimize transport limitations, and achieve chemical and mechanical stability for recyclability.

TOCNF-rDAP2 freeze-dried without cross-linking, Figure 4.4d, exhibited generally similar aerogel structure to TOCNF. Functionalization led to reduced dispersion of TOCNF in water suspensions, and this resulted in larger sheet-like walls and macropores. Additionally, less anisotropy was observed, and more fine fiber structure excluded from the walls was visible. These may be attributed to a reduction in ordering and dispersion in suspension due to decreased net surface charge with amine functionalization, which would lead to less ordered and more condensed wall structures upon ice-templating.

However, the addition of high viscosity sodium salt CMC (0.2 equiv by mass) to TOCNF-rDAP2 led to a recovery in aerogel order and integrity (Figure 4.4g). This aerogel had a bulk density approximately identical to the unfunctionalized TOCNF aerogel, but it exhibited smaller macropores and significant anisotropy. There was long-range directional order in the aerogel walls, indicating that the nominally inert CMC filler may have improved suspension order and dispersion. The significant increase in viscosity with the addition of CMC may also slow down ice crystal growth, which could lead to the smaller and more uniform macropores seen. The mechanical integrity of this aerogel was the greatest due to its structural uniformity and anisotropy.

The dramatic effect of solvent on aerogel structure can be seen in the TOCNF samples freeze-dried from H_2O/tBA cosolvent suspensions (Figure 4.4b,c). The bulk density of these materials was slightly higher than that of TOCNF freeze-dried from water, but the pore structure was radically different. The H_2O/tBA aerogel pores are generally much smaller, with highly connected and finely porous TOCNF walls. The clear, directional macropores seen in TOCNF from water are not apparent. The structure appears denser, but the fine porosity of the fiber structures compensates for the lack of bulk void space from regular macroporosity.

The molecular liquid structure of water and *tert*-butyl alcohol mixtures as well as their ice crystal formation and ice-templating behavior have been previously reported.[65,201–203] The cosolvent mixtures used in this study, 1:1 and 3:1 v%:v% H_2O/tBA, correspond to 16 mol%, 44 wt% and 6 mol%, 21 wt% tBA, respectively. In this mole fraction range of tBA, the hydrophobic self-association of the *tert*-butyl heads of tBA leads to small clusters in a liquid that is otherwise ordered like liquid water.[201] In ceramics templated by H_2O/tBA

mixtures, largely macroporous structures that form in pure H_2O or pure tBA give way to porosity that is 1–2 orders of magnitude smaller with much thinner wall structure.[65] The dynamics of freezing were not investigated, but snowflake-like ice microstructures are apparent in this concentration range. The fine aerogel structure observed in this work may be attributed to the nucleation of these small ice crystals preventing the large sheet-like wall structures of water-derived aerogels.

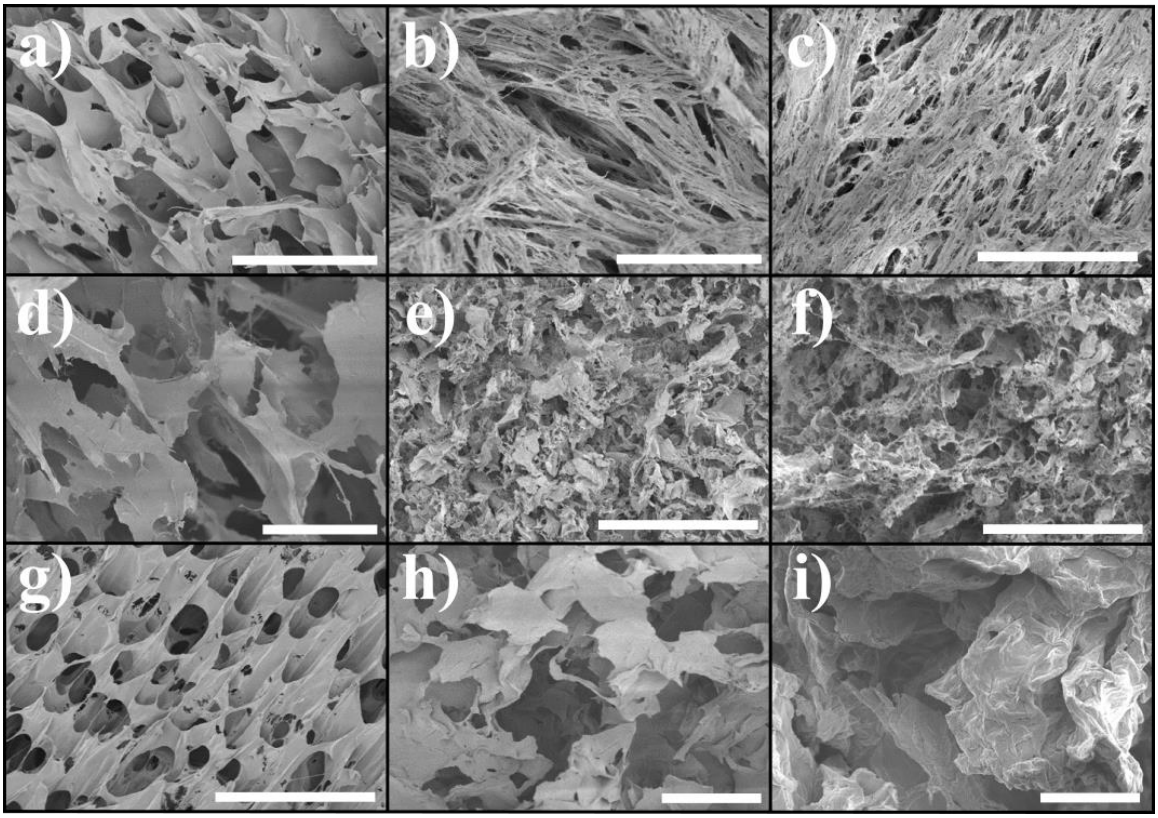

Figure 4.4 – Representative SEM images of the nine freeze-dried aerogels analyzed, all of which were produced from 1.5 wt% suspensions. Scale bars are all 50 µm. (a) TOCNF, (b) TOCNF_1-1, (c) TOCNF_3-1, (d) TOCNF-rDAP2, (e) TOCNF-DAP-TPA_1-1, (f) TOCNF-DAP-TPA_3-1, (g) TOCNF-rDAP2_CMC, (h) TOCNF-rDAP2-XDA, and (i) TOCNF-PEI.

The aerogel structures of TOCNF-DAP cross-linked with TPA are most significantly defined by the H_2O/tBA solvent mixtures from which they were freeze-dried.

Similar to the unfunctionalized TOCNF aerogels from these solvents, the pores were much smaller, and the structure did not exhibit large sheet-like walls. TOCNF-DAP was more poorly dispersed in 1:1 H_2O/tBA, and the small sections of non-porous structure could be attributed to partial aggregation from poor dispersion or from strong chemical cross-linking. TOCNF-DAP-TPA_3-1 did not exhibit these non-porous artifacts nearly as significantly and notably had very fine, interconnected porous structure.

Cross-linked TOCNF-rDAP2-XDA, Figure 4.4h, was freeze-dried from water and had similar large anisotropic non-porous sheets to TOCNF-rDAP2. However, its bulk density was close to an order of magnitude higher as it exhibited partial constriction upon freeze-drying. This is evident in the thickness of the wall structures observed, which was evidently greater than that of the other aerogels freeze-dried from water. As with the loss of amine content by acid-catalyzed amide bond cleavage, the weak acid (dilute HCl) washes of the functionalized hydrogel may have further aggregated fibers in suspension, increasing bulk density. Finally, the PEI-cross-linked material, TOCNF-PEI, was significantly constricted upon freeze-drying which is reflected in its very high density and minimally porous structure. The large, bulk structures of the freeze-dried solid are indicative of strong agglomeration and collapse upon mixing and reaction with PEI. As with TOCNF-rDAP2-XDA, the acid washing steps after freeze-thaw and reaction may have further aggregated the material.

4.3.4 Aerogel Solvent Stability

Cellulose-based aerogels for catalysis are most applicable to flow reaction systems, either in the liquid or gas phase. In a flow system, particular one involving a liquid phase,

the stability of the aerogel structure in the solvent is vital to its function. This differs from many cellulose aerogel applications in which mechanical strength is the physical property of interest. Limited mechanical stress is applied to a stationary aerogel packed, for example, in a flow column for catalysis. As such, the stability of the aerogels studied herein to polar solvent (water), non-polar solvent (toluene), and to the partially polar reaction solvent of interest (acetone) is assessed (Table 4-2). The stability is rated in a scale of 1–4, from completely stable (1) to fully disintegrated (4). For solvent-stable aerogels, the solvent uptake per mass of aerogel is also reported.

Both cross-linked and non-cross-linked aerogels were generally unstable in water. The denser, more agglomerated materials (TOCNF-rDAP2-XDA and TOCNF-PEI), however, were partially stable in water. This could be due to effective cross-linking or a lack of swelling related to the non-porous phases formed. The water uptake in these two cases was very low. Unmodified TOCNF freeze-dried from H_2O/tBA was more stable in water than its cross-linked analogues, however the resulting water-swelled gels formed were not mechanically robust. TOCNF-rDAP2_CMC was fully disintegrated over 48 h in water despite its robust mechanical structure. This supports a key hypothesis of this work that, regardless of mechanical stability, covalent cross-linking is useful, if not necessary, for robust chemical stability.

The aerogels produced herein, as are cellulose-based aerogels generally, are primarily hydrophilic. In highly non-polar toluene, almost all the materials assessed were fully stable over the testing period. As mentioned, freeze-dried TOCNF-rDAP2 was not mechanically robust, and it partially disintegrated even in toluene. Upon swelling with toluene, most of the originally white, opaque aerogels appeared partially transparent. Even

aerogels which were solely physically networked were robust in toluene, and these samples exhibited the greatest toluene uptake.

Table 4-2 – Aerogel densities as well as solvent uptake and stability in water, toluene, and acetone

sample	hydrogel solvent	aerogel density (mg cm^{-3})	*water*		*toluene*		*acetone*	
			uptake (g_{H2O} g^{-1})	stability	uptake (g_{tol} g^{-1})	stability	uptake (g_{acet} g^{-1})	stability
TOCNF_1-1	1:1 v:v H_2O/tBA	38 ± 3	97 ± 7	2	55 ± 3	1	64 ± 3	1
TOCNF_3-1	3:1 v:v H_2O/tBA	31 ± 2	66 ± 3	2	48 ± 2	1	57 ± 3	1
TOCNF-DAP-TPA_1-1	1:1 v:v H_2O/tBA	32 ± 2	-	3	29 ± 1	1	35 ± 1	2
TOCNF-DAP-TPA_3-1	3:1 v:v H_2O/tBA	23 ± 2	-	3	37 ± 1	1	37 ± 1	2
TOCNF-rDAP2	H_2O	18 ± 1	-	4	-	2	-	3
TOCNF-rDAP2_CMC	H_2O	29 ± 2	-	4	61 ± 3	1	61 ± 3	1
TOCNF-rDAP2-XDA	H_2O	130 ± 20	2 ± 0.1	1	13 ± 1	1	8 ± 1	1
TOCNF-PEI	H_2O	1300 ± 380	6 ± 0.2	2	3 ± 0.2	1	3 ± 0.4	1

Key for stability information. 1: Stable - negligibly changed; 2: Slighly unstable - partial flaking or weak gel; 3: Slightly stable - significant flaking, partial redispersion; 4: Unstable - near complete redispersion. The density of TOCNF freeze-dried at 1.5 wt% from water was 26 ± 2 mg cm^{-3}.

Aerogel stability in acetone was slightly worse than that in toluene due to the increased polarity of acetone. All aerogels except the very weak TOCNF-rDAP2 were functionally stable in acetone, although the TPA-cross-linked samples displayed some signs of partial instability. In acetone, unlike in toluene, all samples retained their white color and opacity. The mass uptake of acetone was similar to that of toluene in all materials.

Aerogel stability in acetone was initially promising for their application in flow reaction systems for the aldol condensation, as studied here, which utilized acetone as the solvent.

Solvent stability and uptake testing results showed that chemical cross-linking does not necessarily prevent redispersion in all solvents, especially water, and that strong physical networks can function well for organic solvent stability. Hydrophilic aerogels tested here still readily swell and uptake organic solvent but are significantly more stable than in water, which is ideal for the application to flow reaction system utilizing organic solvents.

4.3.5 Aldol Condensation Catalysis with TOCNF Aerogels

Amine-functionalized acid–base TOCNF materials were evaluated as catalysts for the aldol condensation reaction of 4-nitrobenzaldehyde with acetone. Previous works have developed and optimized CNC surface chemistry for cooperative catalysis of this reaction, utilizing homogeneously dispersed CNCs as heterogeneous catalysts.[138,170] CNCs have very high specific surface area due to their ~ 5 nm cross-section, and thus their catalytically active surfaces were nearly fully accessible by reactants. By using identical catalytic surface functionalization, the catalysts studied here differ from the CNC catalysts primarily by their physical size and solution dispersion and by their lack of sulfate half-esters.

TOCNF catalysts most directly analogous to previously demonstrated CNC-based materials were first tested, as the CNCs were,[138,170] as homogeneously dispersed suspensions. Aqueous suspensions of TOCNF-DAP and TOCNF-rDAP2 were solvent exchanged to the reaction solvent (1:1 v%:v% acetone/acetonitrile), and their catalytic activity for the aldol condensation reaction of 4NB and acetone was evaluated by their

initial reaction rates as well as catalyst mass-specific rates (Figure 4.5). The mol fraction of catalyst (10 mol%) relative to the limiting reactant, 4NB, was held constant and was used to determine the mass of catalyst used by the active amine content (Table 4-1). Both homogeneously tested TOCNF materials showed reasonable catalytic activity but were ~ 70% less active than the optimized CNC catalyst in these conditions.

There are many factors which may account for the reduced activity in the TOCNF catalysts as compared to the reference CNC catalysts. Cellulose nanocrystals were previously demonstrated to be highly advantageous acid–base organocatalysts substrates due to their ordered crystalline surfaces and high specific surface area. The TOCNF catalysts additionally do not possess sulfate half-esters, although these were not demonstrated to be catalytically advantageous.[170] The TOCNF particles, even prior to aerogel formation, have larger cross-sections than CNCs, which reduces their specific surface area and thus available active catalyst. TOCNF samples were more poorly dispersed in the reaction solvent than CNCs, and the resulting partial agglomeration could introduce additional mass transfer limitations in the reaction.

TOCNF samples contain residual amorphous cellulose content, evident by differences in XRD (Figure C.4) and their initial degree of oxidation (Table 4-1). Amorphous cellulose does not benefit from crystalline order shown to be pivotal in the function of acid–base CNC catalysts.[170] Increased amorphous content reduces the availability of proximal cooperative acid and base sites. In similar CNC materials, the ratio of acid to base surface functionalization as well as acid–base site pairing and proximity were key contributors to their activity and in optimization. These TOCNF catalysts were

not optimized for acid/base ratio and are not highly ordered and idealized catalyst supports like the crystalline nanocellulose.

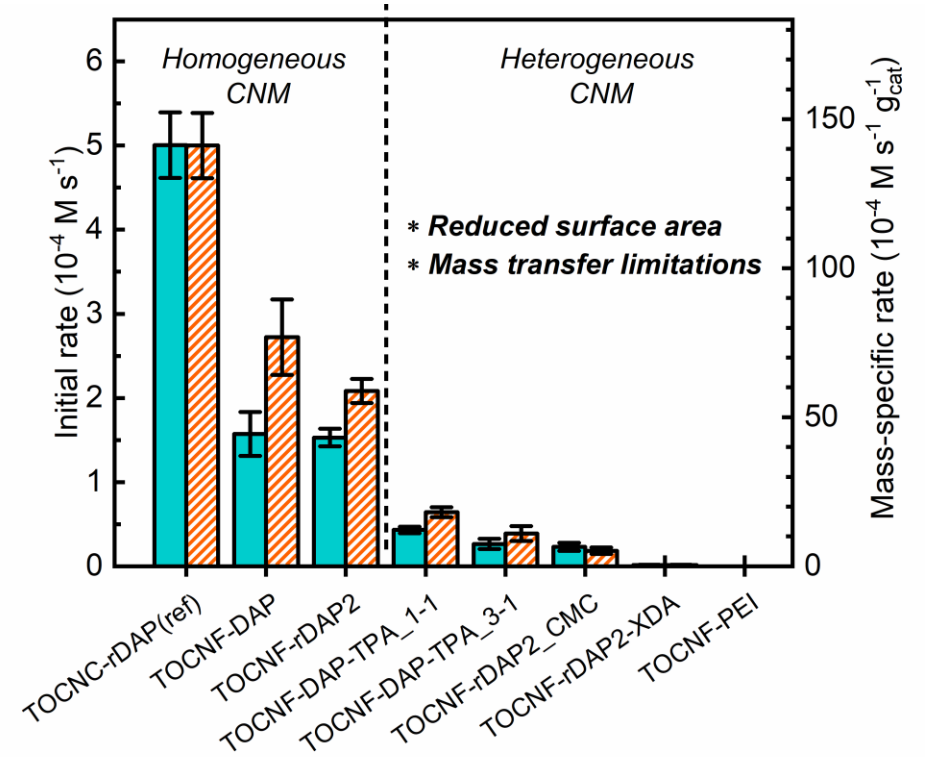

Figure 4.5 – Catalytic activities of TOCNF materials as initial reaction rates and normalized by catalyst masses. The first sample listed, TOCNC-rDAP, is our previously published optimized CNC acid–base organocatalyst presented here as a reference.[170]

TOCNF aerogel catalysts were also evaluated as catalysts under similar reaction conditions (Figure 4.5). Catalytic rates were reduced by several fold in comparison to those of the homogeneous TOCNF catalysts, and TOCNF-PEI did not have measurable catalytic activity. Catalyst quantities were normalized by estimated active amine content (Table 4-1), but this did not attempt to account for surface area reduction or steric hindrance and removal of active sites from the cross-linking chemistries used. Active amine values were thus over-estimations of the true base site loading, which reduces the true mol% catalyst.

Rather than by solvent exchange, a measured mass of the aerogel was added to a reaction flask and dispersed with magnetic stirring in 3 mL of the reaction solvent for 1 h at 60 °C prior to addition of the reactant and internal standard. Aerogels were intentionally fragmented into relatively small pieces before addition to minimize mass transfer limitations. However, the varying aerogel stabilities in the stirred and heated reaction solvent yielded aerogels dispersed to differing degrees in the reaction solvent. Under these conditions, the TPA-cross-linked samples were fairly well dispersed in reaction mixtures, although they were more poorly dispersed than the never-dried solvent exchanged catalysts. The remaining aerogels did not redisperse well in the reaction solutions. In particular, TOCNF-rDAP2-CMC was quite stable and did not significantly redisperse. This lack of dispersion introduced significant mass transfer limitations which account for some of the reduction in catalyst rates.

Aerogel formation significantly reduces the specific surface area of the TOCNF due to the formation of nonporous sheet-like walls in the aerogels. The TPA-cross-linked TOCNF aerogels, which had the greatest activity among the aerogel samples, displayed the finest pore structure by SEM and were the most redispersed in reaction mixtures. Importantly, true active site availability is proportional to accessible surface area. For example, if 10 mol% of a TOCNF aerogel catalyst with an aerogel surface area that was 10 % of its pre-drying homogeneous surface area, its effective mol% would be about 1. With significant TOCNF agglomeration during drying, the effective quantity of catalyst used in the batch reaction tests of aerogels is significantly below that of the homogeneous materials.

Several factors may have contributed to the lack of activity in TOCNF-PEI. The primary reaction active site is a cooperative action between an acid and a base.[170] Despite its high amine loading, the potential for low residual acid content and a large excess of amines means there may be few cooperative acid sites available. The active amine content was estimated with the total primary and secondary amine content, which far exceeds the availability of actual cooperative sites which exist in the material. Most importantly, this freeze-dried material was very dense and not significantly porous. Its effective catalyst surface area is incredibly low, so at an estimated 10 mol% catalyst the true availability of accessible and effective active sites is negligibly low.

4.4 Conclusions

TEMPO-oxidized cellulose nanofibrils (TOCNF) acid–base catalyst aerogels were synthesized with several cross-linking and processing approaches. Acid–base catalytic surface chemistry, known from cellulose nanocrystals, was achieved with surface carboxylic acids and amide-linked primary amines. TOCNF catalysts were cross-linked chemically by small molecules and physically by carboxymethylcellulose. Catalyst aerogels were stable in polar (acetone) and non-polar (toluene) organic solvents but not in water. Chemical cross-linking aided in the solvent stability of aerogel catalysts.

Aerogels produced from water-only suspensions were macroporous with thin aerogel walls, and CMC improved the structure and stability of acid–base functionalized TOCNF. Increasingly fine pore structure and significantly smaller pore sizes were achieved by producing aerogels from water/*tert*-butyl alcohol mixtures. Acid–base TOCNF catalysts exhibited significant catalytic activity for the aldol condensation of 4-nitrobenzaldehyde

and acetone. As expected, TOCNF aerogels had reduced activity as compared to optimized CNC-based catalysts. Aerogel formation reduced activity by limiting active surface area and introducing mass transfer limitations.

CHAPTER 5. SUMMARY AND SUGGESTED FUTURE RESEARCH DIRECTIONS

5.1 Thesis Summary

5.1.1 Chapter 2, Research Aim 1: Design and Demonstration of CNC Organocatalysts

The initial direction of the work presented in this thesis was to demonstrate the feasibility of cooperative organocatalysis using functionalized cellulose nanomaterials. An initial, and ultimately fruitful, multi-step functionalization route of cellulose nanocrystals for acid–base surface chemistry was designed. This simple, two-step CNC modification approach utilized selective TEMPO-mediated oxidation and EDC amide coupling with short alkyl diamines. The option to initially partially reduce the sulfate half-ester content of sulfuric acid-derived CNCs by acid hydrolysis was also presented. Modified CNC surface chemistry was validated qualitatively by FT–IR spectroscopy and quantitatively by conductometric titration and elemental analysis. CNC catalytic activity for the aldol condensation of 4-nitrobenzaldehyde and acetone was initially demonstrated in water/acetone co-solvent reaction mixtures. The processing method of the never-dried CNCs was adjusted to use solvent exchange to disperse the CNC catalysts in an all-organic reaction mixture of acetone/acetonitrile. This change led to a massive increase in catalytic activity, and CNC acid–base catalysts displayed similar activity to well-studied aminosilica organocatalysts. Finally, the importance of the length of the alkyl diamine was highlighted, as CNCs functionalized with a three-carbon diamine significantly outperformed those with either two- or six-carbon diamines. This was rationalized by poor cooperativity and over-

cross-linking, respectively. This chapter was an initial demonstration of cooperative organocatalysis with functionalized cellulose nanomaterials.

5.1.2 Chapter 3, Research Aim 2: Optimizing and Understanding CNC Surface Chemistry

This second aim expanded directly upon the CNC acid–base catalyst framework established in Chapter 2. The catalytic function of the surface chemistry modified CNCs was directly probed by rigorous quantitative control of each aspect. Sulfate half-ester, carboxylic acid, and amine content were varied to investigate the effect of each on catalysis for aldol condensation reactions. Sulfate half-esters were found not to be catalytically useful but were necessary to maintain structural integrity and CNC dispersion. Carboxylic acid and primary amine content both controlled catalytic function of the CNC acid–base catalysts. Normalized by base sites, catalytic activity was strongly correlated with the acid/base ratio of surface species. This indicated that cooperative acid availability was a strong determinant in overall catalytic function. Protection of diamines during functionalization was disadvantageous due to issues with incomplete deprotection. CNC catalysts were utilized for aldol condensation upgrading reactions of furfural, demonstrating good activity and selectivity to dehydrated products. CNCs outperformed analogous silica-supported acid–base catalysts which were synthesized, tested, and compared. CNC functionalization was examined at the molecular scale, and the spatial arrangement of functional groups due to the ordered crystalline surfaces was found to be highly advantageous.

5.1.3 Chapter 4, Research Aim 3: Development of Acid–base CNF Aerogel Catalysts

In this final research aim, the acid–base catalyst functionalization developed in previous aims was applied to the synthesis of porous aerogel acid–base catalysts. Highly dispersed cellulose nanofibrils were produced by TEMPO oxidation and subsequent homogenization of microfibrillated cellulose. Acid–base surface chemistry was achieved with previously developed functionalization methods. Various approaches were used to further cross-link and produce robust CNF aerogel catalysts. CNFs were cross-linked with dialdehyde and diamine small molecules after hydrogel network formation. Physically cross-linked CNFs were produced with the addition of an inert carboxymethylcellulose filler. CNFs were also chemically cross-linked with amine-dense poly(ethyleneimine). Chemical cross-linking improved aerogel solvent stability. Incorporation of *tert*-butyl alcohol into suspension solvents drastically decreased the pore size of CNF aerogels. Acid–base CNFs displayed promising reactivity in homogeneous suspension. Cross-linked aerogels were also active catalysts for the aldol condensation reaction but suffered from reduced surface areas and mass transfer limitations.

5.2 Future Research Directions

5.2.1 Aerogel-encapsulated Catalysts for Cascade Reactions

This suggested future direction is based on an initial reach goal of this thesis project that was, ultimately, not reached. This direction is heavily inspired by an impressive body of work by Cranston and coworkers, in which an extremely robust approach to cross-linked CNC aerogel formation was developed[50] and subsequently utilized as a versatile matrix in which other active nanomaterials could be encapsulated.[82,85,193] The Cranston group

developed orthogonally-functionalized CNCs, one with a semi-rigid 10-atom functional group terminated with a dihydrazide and another with surface aldehydes. Upon mixing together aqueous suspensions of these two CNC types, the dihydrazide spontaneously reacts with surface aldehydes of the other upon contact. The mixture is rapidly combined and then freeze-dried, yielding a flexible, shape-recovering aerogel.[50]

This basic design was used as the basis for a number of publications, several of which amounted to, basically, incorporation of functional nanomaterials into the CNC–CNC suspension prior to freeze-drying. Once mixed and freeze-dried, these functional particles were physically entangled in the CNC aerogel while maintaining their function. Supercapacitor aerogels were achieved by incorporation of polypyrroles nanofibers,[193] MnO_2 nanoparticles,[193] or multiwalled carbon nanotubes.[82] Additionally, three water-stable MOFs (ZIF-8, UiO-66, and MIL-100(Fe)) were incorporated into this same template in a similar fashion and used for adsorptive separations for water treatment.[85] My proposed research direction is to incorporate heterogeneous catalyst materials into this or another model system for facile, extremely robust aerogel formation. A robust cross-linked cellulose nanomaterial aerogel is an extremely interesting and versatile substrate, and the ability to "drop" in particles to this compressible, low-density, swellable structure is extremely powerful.

There are many possible research directions, but initial work could incorporate simple heterogeneous catalysts, for example Pd/Al_2O_3, into this existing CNC aerogel framework and evaluate any changes in their function. For example, Pd/Al_2O_3 for test hydrogenation reactions could be tested as neat particles and encapsulated within CNC aerogels. The possibility of mass transfer limitations could be evaluated in liquid-phase

reactions, preferably in flow. This also provides a convenient, low pressure-drop matrix for fine heterogeneous catalyst particles. This reduces the need for pelletization and, in the gas phase, would likely not be hindered by external mass transport problems. Even more ambitiously, functionalized cellulose nanomaterial aerogels could be used as the encapsulating phase. In this regard, cascade chemistry could be approached by using, for example, an organocatalytic CNM aerogel and an encapsulated supported metal catalyst. Cascade reactions in biomass upgrading could be investigated, for example the aldol condensation and subsequent hydrogenation/hydrodeoxygenation of furfural with renewable ketones and H_2.[204–206] Acid–metal systems, utilizing simple TEMPO-oxidized CNFs which are the ideal CNM for aerogel formation, can perform ring-opening and hydrogenation reactions of levulinic acid, another biomass platform molecule.[207,208]

5.2.2 Enzyme Immobilization in CNM Aerogels for Pharmaceutical Transformations in Flow

A recent book chapter[209] discussed recent developments in cellulose-based supports for enzyme immobilization. As with all the work being suggested in this chapter, this is a promising practical application of cellulose nanomaterial aerogels. Enzymes are expensive but powerful catalysts, and immobilization to enhance recovery, reusability, and activity is a growing area of interest in applications of enzymes. Many current applications of enzymes are in pharmaceutical transformations, but this is significantly related to the steep cost of enzyme catalysis in industrial applications, whereas the high margins of the pharmaceutical industry compensate for that cost. With improved recovery, efficiency, and utilization, enzymes may be applied in an expanding array of industrial applications.

Cellulose-binding domains (CBDs) are typically found in cellulolytic enzymes,[210] which bind to polysaccharides in order to systematically degrade them. However, these cellulose-binding domains have been added to non-cellulolytic enzymes through genetic engineering for enzyme immobilization. For example, β-glucosidase was immobilized with a non-natural cellulose-binding domain and was fully non-leaching while retaining most of its activity.[211] Many enzyme immobilization techniques are non-specific or non-covalent, including adsorption[212] and cross-linking. Amine-containing polysaccharides, specifically chitin and chitosan, have been widely used for enzyme immobilization given their reactivity and affinity based on the amine and acetamide functionalities.[213] Much of this work, aside from the recent book chapter, is quite dated (1990s–early 2000s), and significant strides in enzyme, protein, genetic, and cellulose engineering have been made. Robust, chemically and mechanically stable cellulose nanomaterial aerogels like those discussed in the previous section[50] are extremely promising substrates for enzyme immobilization. They are biocompatible, macroporous, lightweight, and functionalizable. Incorporation of cellulose-binding domains in enzymes for important industrial transformations is well within the reasonable realm of protein engineering. While I am not an expert in biocatalysis or pharmaceutical transformations, the ability to produce CNM aerogels of any shape or size could position them as feasible industrial supports for enzymes.

5.2.3 Continuous Separations with Cellulose Nanomaterial Aerogels

Functional CNM aerogels are often demonstrated in separation applications. Hydrophobized CNMs can readily separate oil from water,[50,214] functionalized aerogels can adsorb and degrade dyes and heavy metals,[86,87,98,99] and MOF-containing CNF films have

been used for gas separations.[215] These demonstrations are typically performed as simple demonstrations (oil and water separation by photographs) or as basic uptake kinetics or capacities. Aerogel materials are solid porous scaffolds amenable to flow applications, and applications in continuous flow are often more industrially relevant.

Simple suggestions would be to demonstrate and further investigate established heavy metal or dye adsorptive separations in flow systems to evaluate CNM aerogel sorbent stability, capacity, and regenerability. The encapsulation of MOFs in CNM aerogel structures is under-investigated given the breadth of separation applications of metal organic frameworks.[216] Recently, an amine-functionalized Mg MOF was shown to have remarkable CO_2 capture working capacities with very low cycling temperatures.[217] This interesting MOF, Mg_2(dobpdc), was later grown on a low-pressure-drop alumina monolith in order to demonstrate its feasibility in direct air capture applications.[218] While this and many other MOFs are not water stable, and thus far all examples of MOFs incorporated into CNM aerogel frameworks have used water-based processing, there is little work done in CNM aerogels produced from alternative solvents. The work presented in this thesis, for example, demonstrates unique aerogel structures produced by freeze-drying CNMs from water/*tert*-butyl alcohol mixtures. CNCs are dispersible in highly polar organic solvents like DMSO and DMF, and DMSO, for example, is compatible with freeze-drying. The incorporation of non-water stable MOFs into organic solvent derived CNM freeze-dried aerogels poses an interesting research direction. Macroporous CNM aerogels, for example, could be effective low pressure drop matrices for CO_2 capture materials like the monolith in the cited work.

APPENDIX A. CHAPTER 2 SUPPORTING INFORMATION

A.1 Product Isolation and NMR Analysis of Catalyzed Aldol Condensation Selectivity

In order to identify and confirm major products formed as well as determine isolated yields, larger scale reactions were performed (20 mL reaction volume) and the aldol condensation reaction mixtures (Figure A.1) were recovered at the end of the 5 h reaction periods and isolated by column chromatography. Reaction solutions were cooled to room temperature and transferred to centrifuge tubes. The suspension of homogeneous products and CNC catalysts was centrifuged for 20 min at 4000 rpm. The supernatant solution was recovered, and the catalysts were washed and centrifuged two more times with additional solvent. The solvents (acetonitrile and acetone) were removed from the recovered product mixtures by rotary evaporation at 40 °C. The dried products of the larger scale reactions were dissolved in ethyl acetate, mixed with 2 g of silica gel, and dried by rotary evaporation. This was used to dry-load a silica gel column, from which products were eluted in 25:75 EtOAc:hexanes. The column was finally flushed with methanol. Fractions were combined and dried, weighed, and then dissolved in DMSO-d_6 and analyzed via ^{1}H NMR with a Bruker Avance III 400 MHz NMR. Some impurities were removed from **2** after collection and prior to analysis by dissolving the dried product in diethyl ether and removing trace insoluble material. Isolated yields for starting material and major products are reported in Table A-2, and NMR spectra of isolated chemical species are shown in Figure A.2–Figure A.4.

Otherwise, final reaction mixtures (4 mL) were recovered as described above and dissolved in DMSO-d_6 without purification for ^{1}H NMR analysis. From these crude NMR spectra, the selectivity of the aldol condensation reaction of 4-nitrobenzaldehyde (**1**) to the aldol (**2**) and dehydration (**3**) products was determined by integrations of the proton peaks in bold in the NMR assignments below. A small fraction of the crossed-aldol adduct (e.g. **4**) was detected by GC-MS. The conversion of **1**, the selectivity toward and yields of products **2** and **3** are calculated by equations *A-1–A-3*, respectively, and shown in Table A-1. An example ^{1}H NMR spectrum of a crude product mixture used for selectivity and yield calculations is shown in Figure A.5.

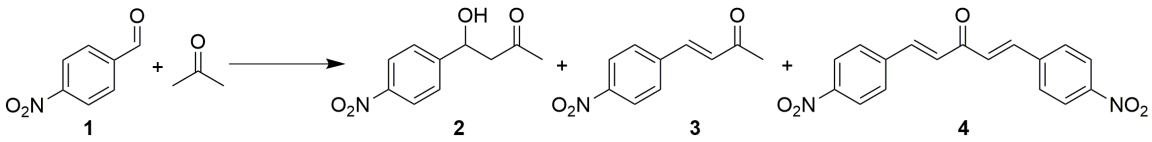

Figure A.1 – Aldol condensation reaction of 4-nitrobenzaldehyde (1) and acetone. The major products formed are 2 and 3, with a small percentage of crossed-aldol condensation products like 4 and other related adducts evident in GC-MS analysis.

1. 4-nitrobenzaldehyde: ^{1}H (400 MHz, DMSO-d6) δ **10.17 (s, 1H)**, 8.43 (dt, J = 8.7 Hz, 2H), 8.17 (d, J = 8.8 Hz, 2H)

2. 4-hydroxy-4-(4-nitrophenyl)butan-2-one: ^{1}H (400 MHz, DMSO-d6) δ 8.20 (dt, J = 8.8 Hz, 2H), 7.64 (dt, J = 8.5 Hz, 2H), 5.72 (d, J = 4.8 Hz, 1H), **5.15 (q, J = 4.9 Hz, 1H)**, 2.75 (d, J = 6.6 Hz, 2H), 2.14 (s, 3H)

3. 4-(4-nitrophenyl)but-3-en-2-one: ^{1}H (400 MHz, DMSO-d6) δ 8.27 (dt, J = 8.9 Hz, 2H), 8.00 (dt, J = 8.8 Hz, 2H), 7.73 (d, J = 16.5 Hz, 1H), 7.00 (d, J = 16.4 Hz, 1H), **2.38 (s, 3H)**

1,4-dimethoxybenzene (internal standard): ^{1}H (400 MHz, DMSO-d6) δ **6.86 (s, 4H)**, 3.69 (s, 6H)

$$x_1 = \frac{I_2 + I_3}{I_1 + I_2 + I_3} \quad \text{(A-1)}$$

$$S_i = \frac{I_i}{I_2 + I_3} \quad \text{(A-2)}$$

$$\gamma_i = \frac{I_i}{I_1 + I_2 + I_3} \quad \text{(A-3)}$$

Table A-1 – Product analysis of the aldol condensation reaction for CNC catalysts (60 °C, 10 mol%) recovered after 5 hours and analyzed via GC and NMR, described above

Sample	Conversion (%, GC FID)	Conversion (%, NMR, *eq A-1*)	Selectivity to 3 (%, NMR, *eq A-2*)	Yield of 2 (%, NMR, *eq A-3*)	Yield of 3 (%, NMR, *eq A-3*)
CNC-DS50-COOH	< 1	< 1	-	-	-
CNC-DS50-DAP	65	66	88	7.9	58
CNC-DS50-EDA	17	17	66	5.8	11
CNC-DS50-HMDA	16	15	71	4.4	11

Table A-2 – Yields of major chemical species isolated after 5 h of reaction (CNC-DS50-DAP catalyst, 20 mL, 60 °C, 10 mol%, 50:50 acetone:MeCN) determined by mass of isolated products and crude NMR integrations of the mixture prior to purification

Molecule	Isolated Yield[a] (%)	Crude NMR Yield[b] (%)	Selectivity[a] (%)	Selectivity[b] (%)
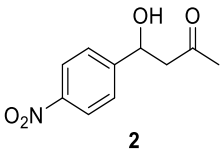 **2**	6.3	7.4	22	15
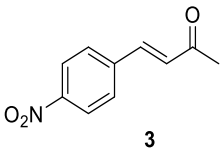 **3**	31	42	78	85

Discrepancies between yields and selectivities determined by each method may be primarily attributed to imperfect separation during column chromatography (impurities & incomplete recollection) as well as incomplete drying (trace water and other solvents). The conversion of **1** by crude NMR was 49% and the isolated yield of residual **1** by mass was 43%. To note, **2** had noticeably more impurities by NMR after separation in comparison to **1** and **3**, which were isolated with higher degrees of purity.

[a]Determined by masses of purified products after column chromatography.

[b]Determined by crude NMR integrations.

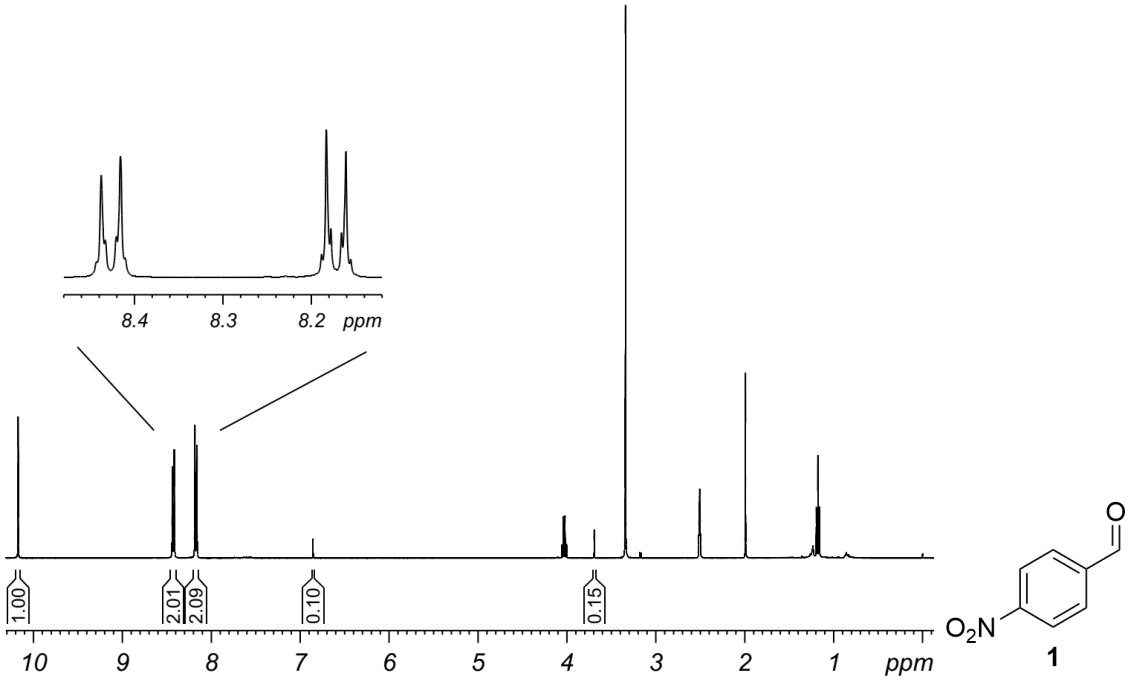

Figure A.2 – ^{1}H NMR spectrum of 4-nitrobenzaldehyde (1) isolated from the recovered aldol condensation reaction mixture at 5 h catalyzed by CNC-DS50-DAP. Noted impurities: 3.89 and 6.85 ppm are trace 1,4-dimethoxybenzene, the internal standard; ~0.85 and 1.23 ppm are trace hexanes; 1.18, 1.99, and 4.03 ppm are trace ethyl acetate; 3.16 is trace methanol; 3.35 ppm is trace water generated by the condensation reaction; 2.50 ppm is the DMSO-d_6 solvent peak.

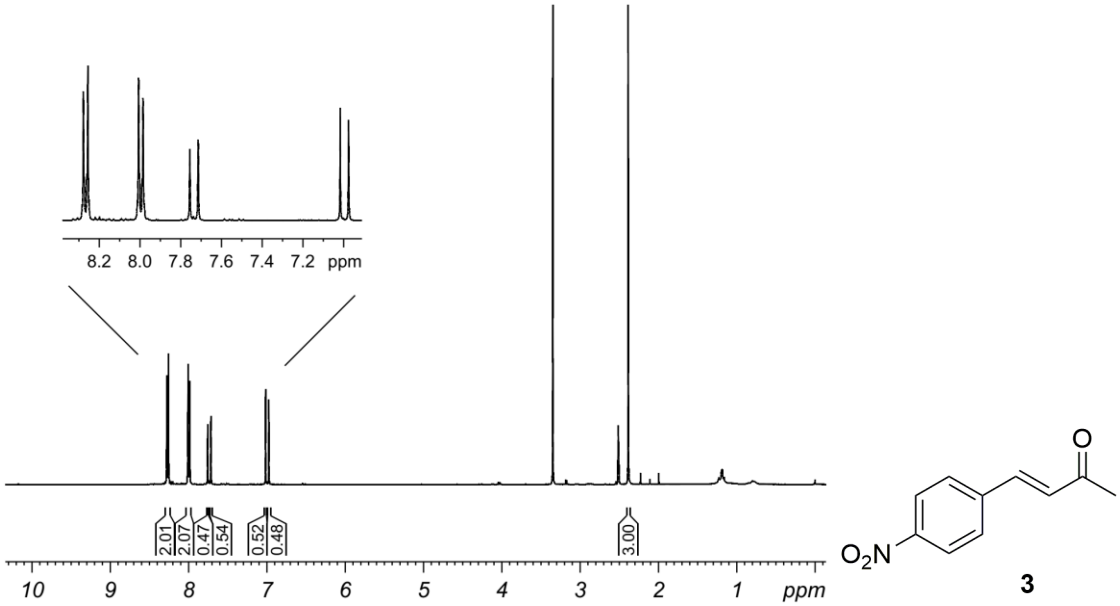

Figure A.3 – ^{1}H NMR spectrum of 3 isolated from the recovered aldol condensation reaction mixture at 5 h catalyzed by CNC-DS50-DAP. Noted impurities: ~0.85 and 1.23 ppm are trace hexanes; 1.18, 1.99, and 4.03 ppm are trace ethyl acetate; 3.16 is trace methanol; 3.35 ppm is trace water generated by the condensation reaction; 2.50 ppm is the DMSO-d_6 solvent peak; ~2–2.2 ppm are methyl peaks from self-condensation of acetone and other side products.

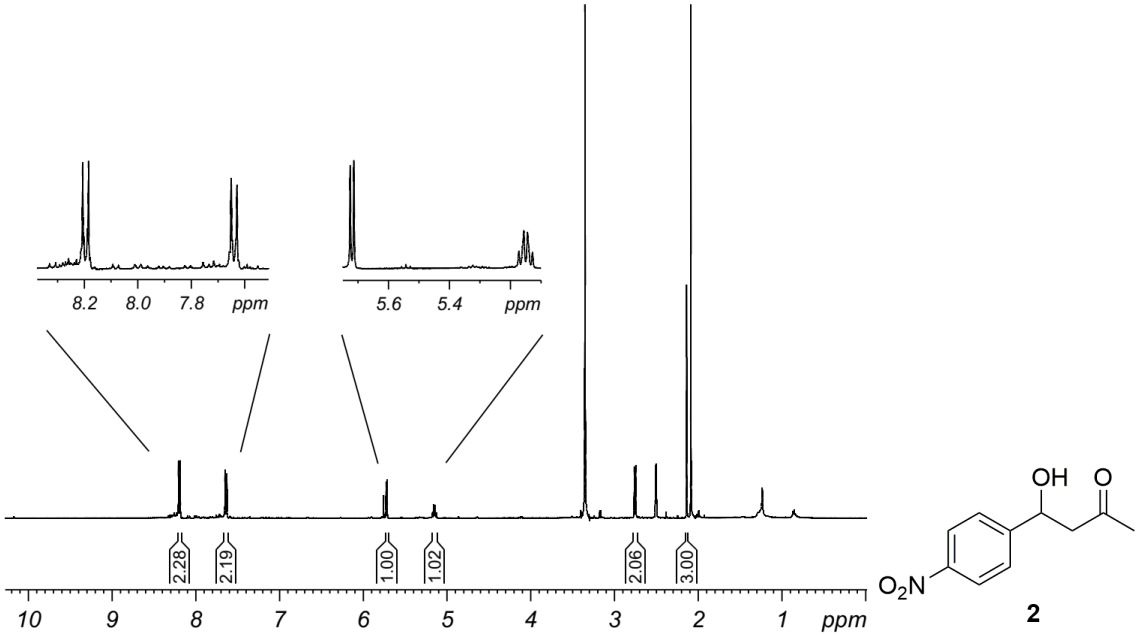

Figure A.4 – ^{1}H NMR spectrum of 2 isolated from the recovered aldol condensation reaction mixture at 5 h catalyzed by CNC-DS50-DAP. Noted impurities: ~0.85 and 1.23 ppm are trace hexanes; 2.09 ppm is acetone; 3.16 is trace methanol; 3.35 ppm is trace generated by the condensation reaction; 2.50 ppm is the DMSO-d_6 solvent peak; ~7.5–8.3 are aryl protons from various side products, including 3 and mixed condensation products.

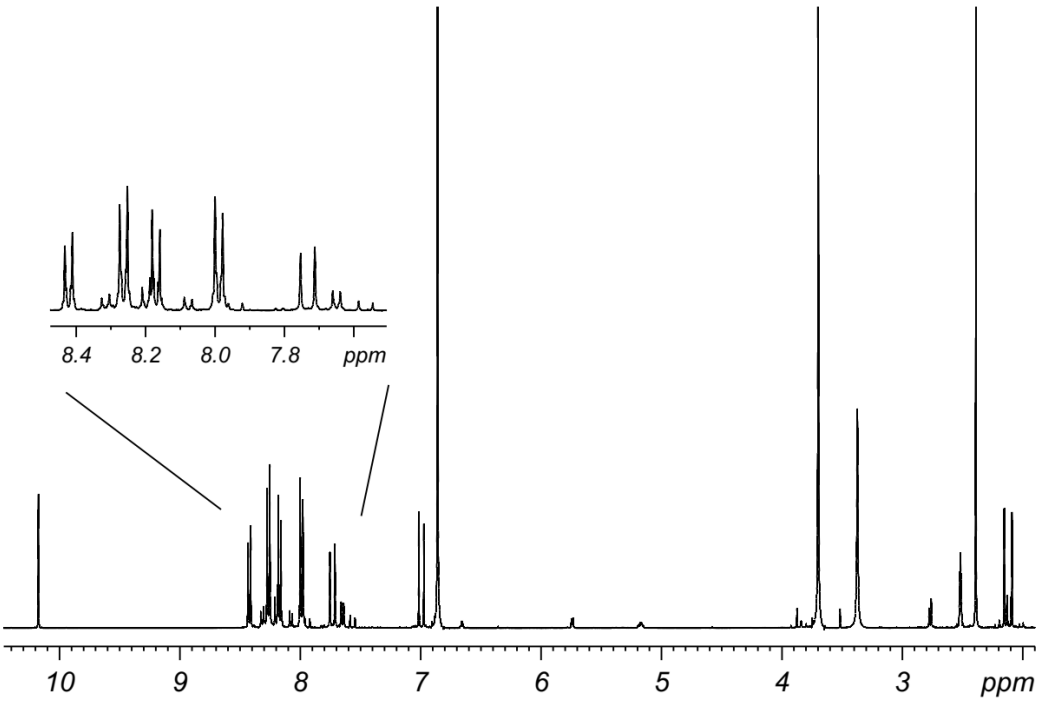

Figure A.5 – Example ^{1}H NMR spectrum of the crude recovered product mixture (5 h) from a catalyzed aldol condensation reaction (CNC-DS50-DAP) including the internal standard, 1,4-dimethoxybenzene. Noted impurities: small peaks from ~7.5–8.3 ppm are aryl protons from various side products, including mixed condensation products; 3.35 ppm is trace water generated by the condensation reaction; 2.50 ppm is the DMSO-d_6 solvent peak; ~2–2.2 ppm are methyl peaks from self-condensation of acetone and other side products.

A.2 FTIR Spectra of Functionalized CNC Samples

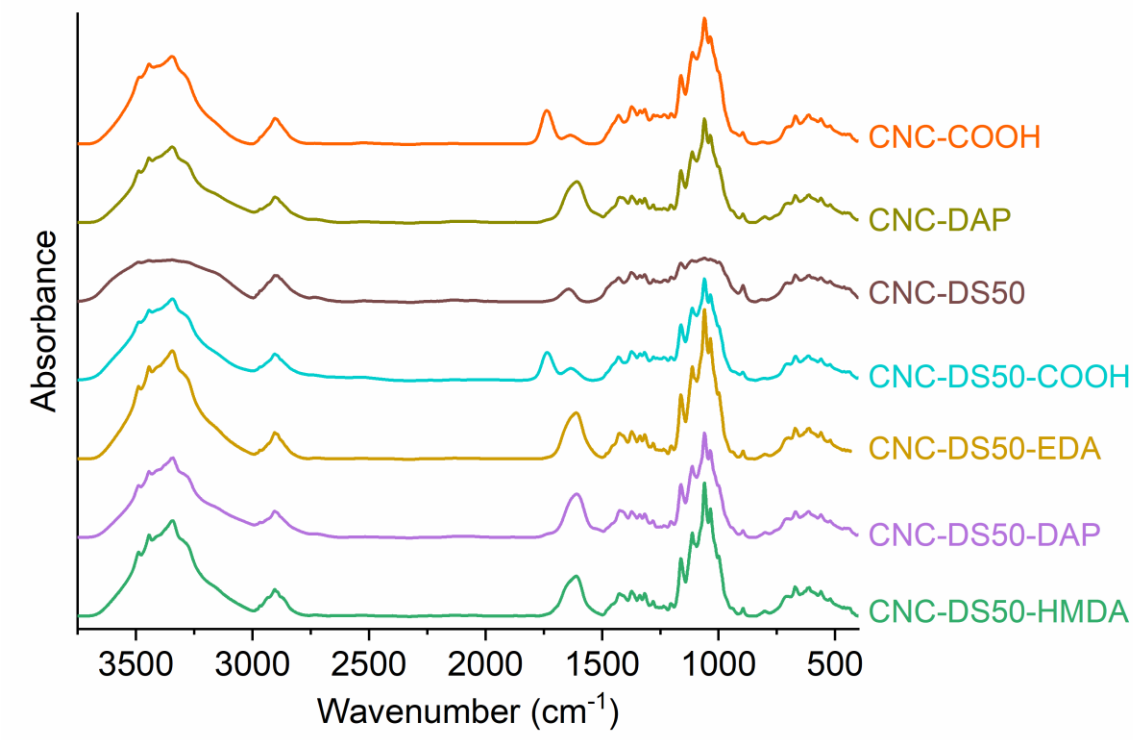

Figure A.6 – Full transmission FTIR spectra of functionalized CNCs.

A.3 Scanning Electron Microscopy of Functionalized CNCs

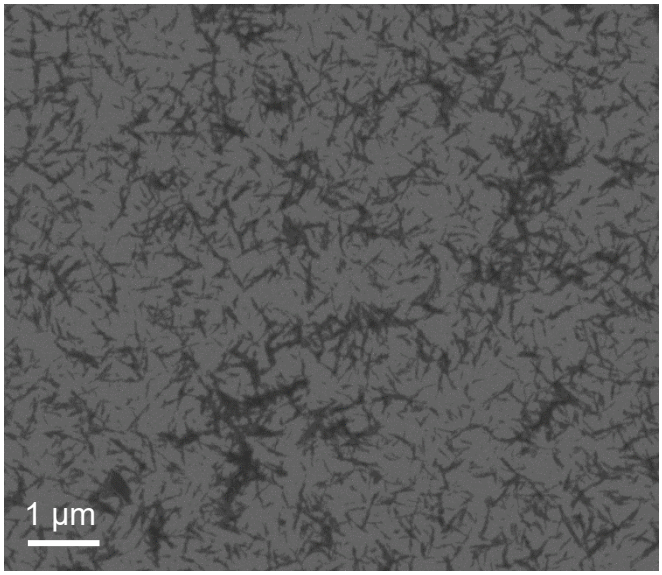

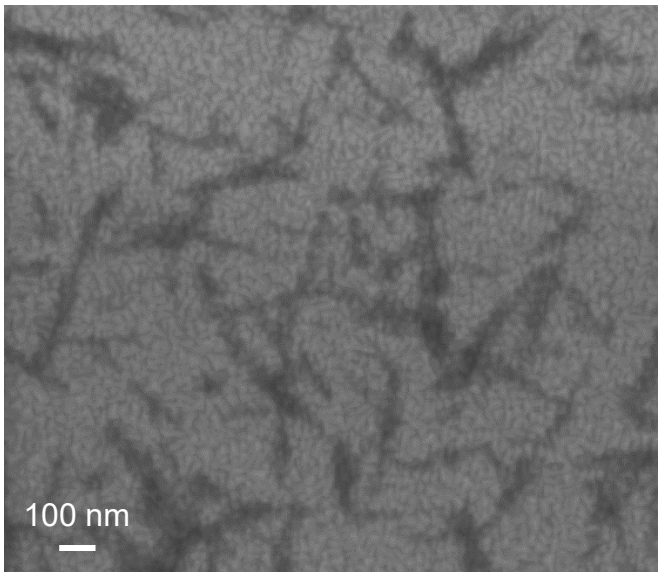

Figure A.7 – SEM images of CNC-DS50-DAP. SEM samples were prepared by dropcasting CNC suspensions (< 0.01 wt%) onto plasma-cleaned Pt-coated substrates. SEM images were collected with a ZEISS Ultra 60 FE-SEM. Some CNC cross-linking and agglomeration is evident.

APPENDIX B. CHAPTER 3 SUPPORTING INFORMATION

B.1 Synthesis of *tert*-butyl-2-methyl-3-(triethoxysilyl)-propanoate

The *tert*-butyl protected carboxylic acid silane was synthesized by hydrosilylation of *tert*-butyl methacrylate with triethoxysilane silane utilizing Karstedt's catalyst as reported elsewhere.[111]

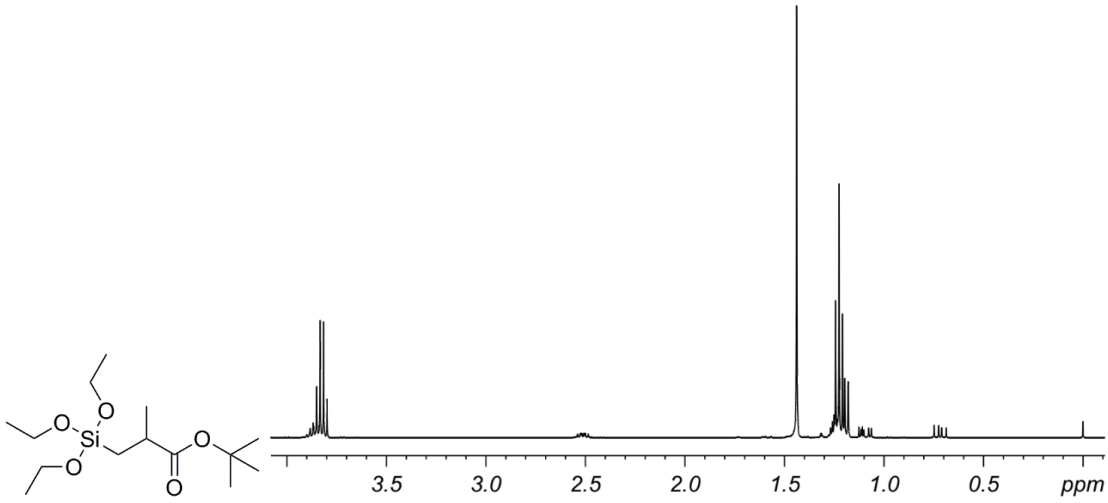

Figure B.1 – ^{1}H NMR spectrum of *tert*-butyl-2-methyl-3-(triethoxysilyl)-propanoate as synthesized.

tert-butyl-2-methyl-3-triethoxysilyl-propanoate: ^{1}H (400 MHz, $CDCl_3$) δ 3.82 (q, *J* = 7.0 Hz, 6H), 2.51 (qt, *J* = 7.0 Hz, 1H), 1.44 (s, 9H), 1.23 (t, *J* = 7.0 Hz, 10H), 1.19 (d, *J* = 7.0 Hz, 3H), 1.09 (dd, *J* = 15.2 Hz, 1H), 0.72 (dd, *J* = 15.2 Hz, 1H)

B.2 Catalyst Synthetic Schemes

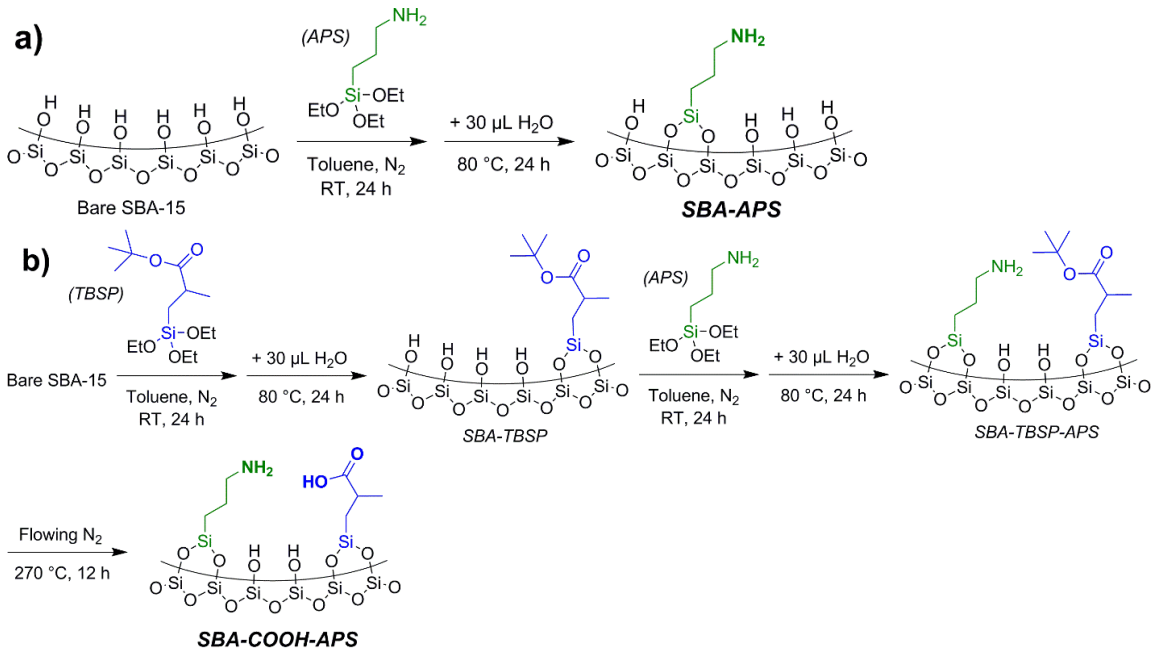

Figure B.2 – Synthesis scheme for SBA-15 supported organocatalysts: (a) SBA-APS, (b) SBA-COOH-APS. Residual silyl ethoxy groups post-grafting are omitted.

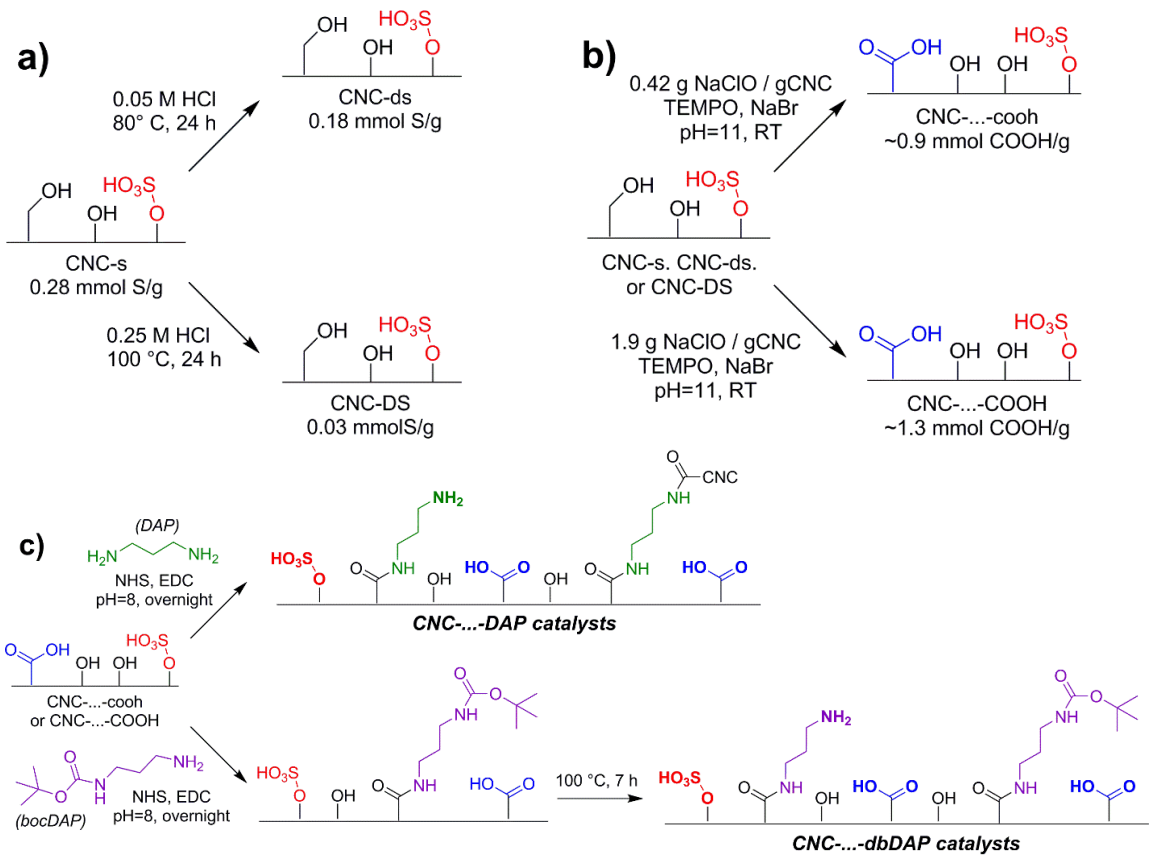

Figure B.3 – Synthesis scheme for cellulose nanocrystal catalysts. Ellipses indicate non-specific intermediate sample descriptors, e.g. CNC-…-cooh may refer to CNC-ds-cooh or CNC-DS-cooh. (a) Partial removal of sulfate half-ester content by acid hydrolysis with HCl. (b) Partial or significant TEMPO-mediated C6 hydroxyl oxidation. (c) Amide coupling to carboxylic acids by 1,3-diaminopropane (DAP, green) or n-boc-1,3-diaminopropane (bocDAP, purple) and subsequent hydrothermal boc deprotection. The sample CNC-ds-COOH-HT was treated with the hydrothermal deprotection conditions despite lacking boc protecting groups.

B.3 Catalyst Spectroscopic and Textural Characterizations

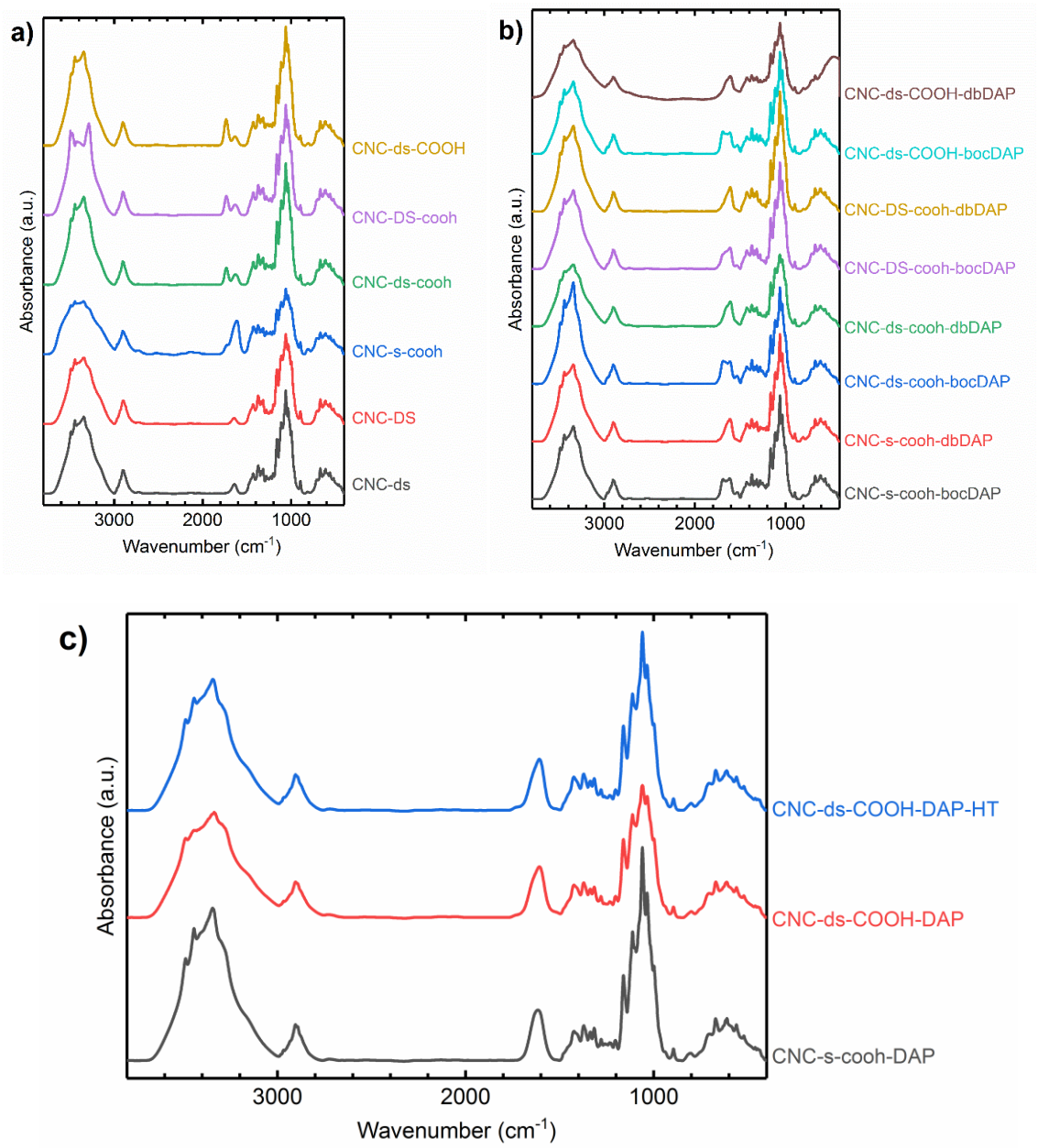

Figure B.4 – Full transmission FTIR spectra of functionalized CNCs: (a) partially desulfated and oxidized CNCs; (b) bocDAP-functionalized CNCs before and after deprotection; (c) DAP-functionalized CNCs.

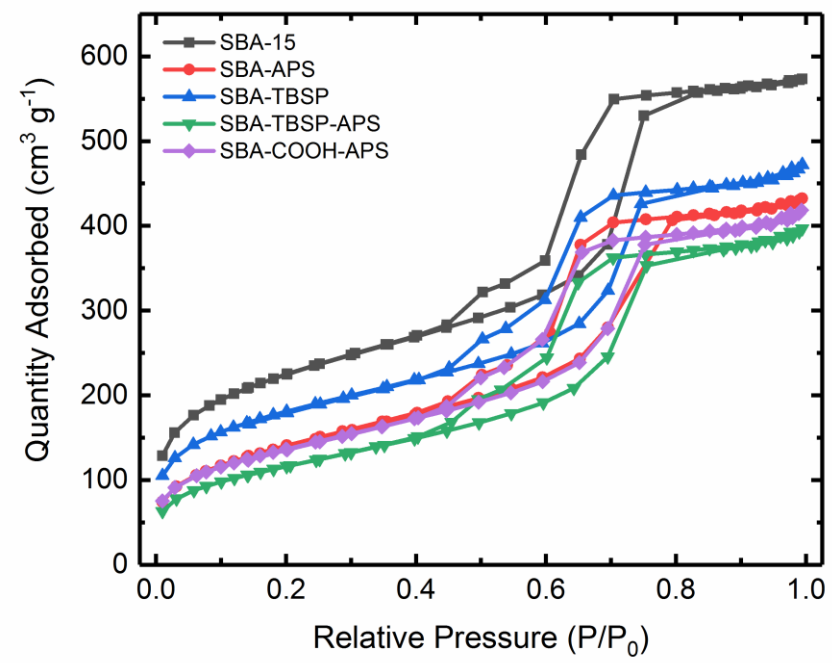

Figure B.5 – N_2 physisorption isotherms for bare SBA-15 and SBA-15-supported catalysts and intermediate materials.

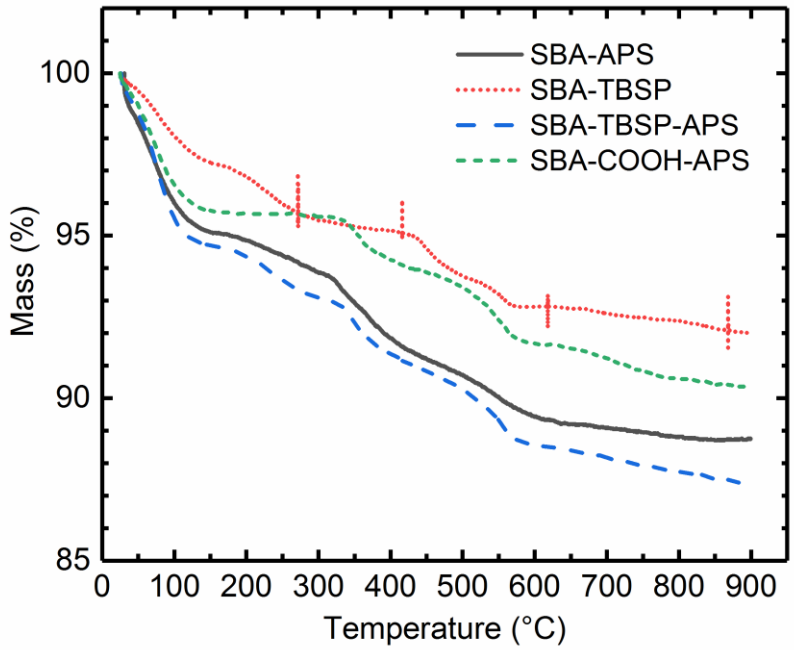

Figure B.6 – Thermogravimetric analysis of SBA-15-supported catalysts and intermediate materials. The loss of the *tert*-butyl protecting group from TBSP is seen in the mass loss between 200 and 300 °C. These losses are not present in the deprotected sample, SBA-COOH-APS.

B.3.1 FTIR Analysis of Silica-Supported Catalysts

A relatively strong signal from bound water (1635 cm^{-1}) impedes detailed analysis of underlying peaks (e.g. primary amine N-H bending ~1600 cm^{-1}). The ester carbonyl at ~1700 cm^{-1} is reduced significantly during deprotection, and some intensity attributed to a carboxylate formed by interactions between carboxylic acid and primary amine-containing silanes is visible around 1550 cm^{-1}. This is in agreement with the referenced work which described the acid–base interactions resulting from proximal grafting of carboxylic acid- and primary amine-containing silane.[111] Peak intensities are low, in particular for SBA-COOH-APS, which limits the conclusiveness of FTIR analysis for these materials. However, the spectra are consistent with previous work and the proposed description of the SBA-COOH-APS catalyst surface.

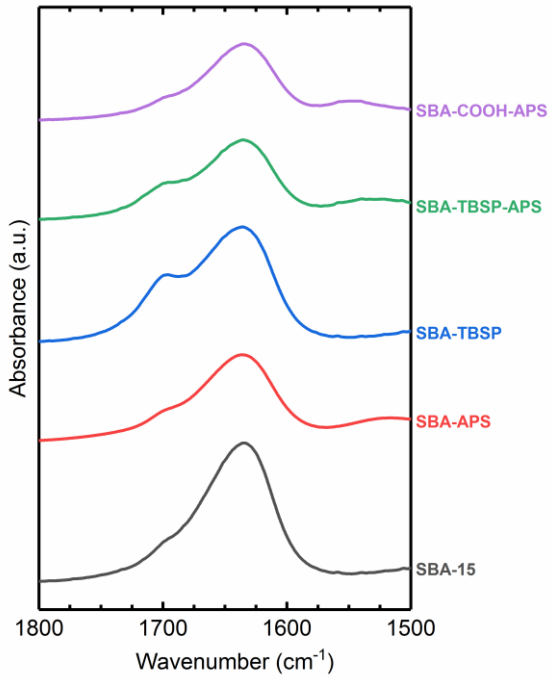

Figure B.7 – A portion of the FTIR spectra for SBA-15, SBA-15-supported catalysts, and intermediate materials.

B.4 Reaction Mechanism and Mass Transfer Limitation Considerations

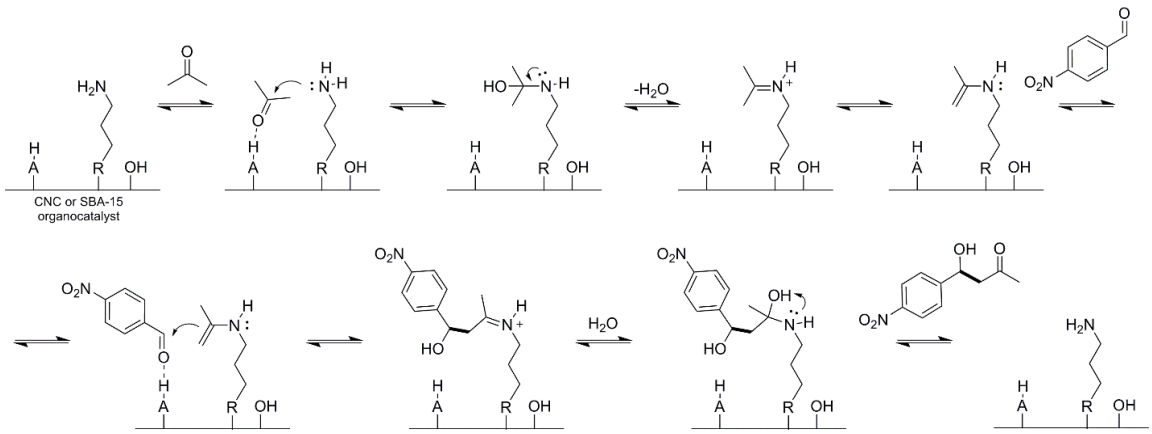

Figure B.8 – Mechanism of the acid-base catalyzed aldol condensation of 4NB and acetone by a generic cooperative acid, *A*, with a primary amine (CNC: *R* = CNC – CH_2 – CONH; SBA-15: *R* = SBA-15 – O – Si).[113,117,120] **The cooperative acid *A* is typically a surface silanol for SBA-15 or a carboxylic acid for CNC catalysts.**

B.4.1 Calculation of Mears' Criterion to Determine External Transport Effects

The Mears' criterion is defined as follows:

$$MR = \frac{-r'_{obs}\rho_{bulk}R_p n}{k_c C_{bulk}} = \frac{-r_{obs}R_p n}{V k_c C_{bulk}} \quad \text{(B-1)}$$

rewritten here in terms of overall max reaction rate $r_{obs,}$ the reaction order n, reaction volume V, particle size R_p, and mass transfer coefficient k_c. For values of the Mears' criterion $MR \ll 0.15$, external mass transfer limitations are considered negligible. A conservative (high) estimate for R_p was used based on functionalized CNC DLS measurements from previous works.[138] Mass transfer coefficients were calculated using correlations for the Sherwood number for forced convection.

Table B-1 – Parameters and values used in the calculation of the Mears' criterion (MR)

	CNC catalysts	**SBA-15 catalysts**
r_{obs} (max) (mol s^{-1} m^{-3})	0.5	0.375
R_p (nm)	500	1000
V (cm^{-3})	4	4
n	1	1
k_c (m s^{-1})	0.0085	0.0054
C_{bulk} (mol m^{-3})	50	50
MR	**1.7×10^{-6}**	**4.4×10^{-6}**

B.4.2 Calculation of Weisz-Prater Parameter to Determine Internal Transport Effects

The Weisz-Prater parameter is defined as follows:

$$C_{WP} = \frac{r_{obs} R_p^2}{D_{eff} C_{bulk}} \quad \text{(B-2)}$$

The Weisz-Prater parameter may be used to estimate the effects of internal mass transfer limitations on overall reaction rate. If $C_{WP} \ll 1$ then internal MT effects may be assumed to be negligible. The effective diffusion coefficient in the interior of catalyst particles was estimated by an empirical formula for liquid diffusion in pores described by Ternan:[219,220]

$$D_{eff} = D_{bulk} \frac{(1-\lambda)^2}{(1+P\lambda)} \quad \text{(B-3)}$$

where λ is the molecule to pore radius ratio, P is an empirical factor (~11), and D_{bulk} is estimated for liquids. The internal structure of partial CNC agglomerates during reaction is challenging to describe, but a value of 5 nm was estimated for the internal "pore size" of a CNC agglomerate. The SBA-15 pore radius was determined by N_2 physisorption using the BdB-FHH method for cylindrical pores.

Table B-2 – Values and parameters used in the calculation of the Weisz-Prater parameter

Parameter	CNC catalysts	SBA-15 catalysts
$\mathbf{r_{obs}}$ **(max) (mol s^{-1} m^{-3})**	0.5	0.375
$\mathbf{R_{particle}}$ **(nm)**	500	1000
$\mathbf{d_{pore}}$ **(nm)**	5	6
$\mathbf{D_{AB}}$ **(m^2 s^{-1})**	10^{-9}	10^{-9}
$\mathbf{D_{eff}}$ **(m^2 s^{-1})**	2.9×10^{-10}	3.4×10^{-10}
$\mathbf{C_{bulk}}$ **(mol m^{-3})**	50	50
$\mathbf{C_{WP}}$	$\mathbf{8.6\times10^{-6}}$	$\mathbf{2.9\times10^{-5}}$

B.5 Additional Catalyst Performance Evaluations and Descriptions

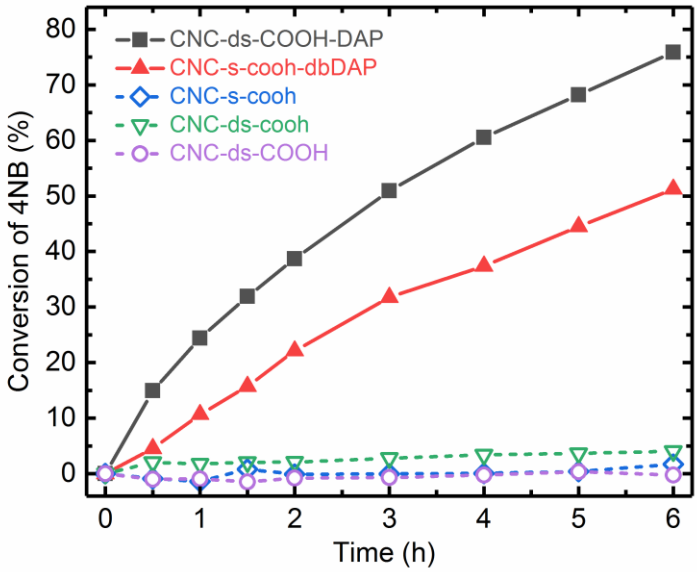

Figure B.9 – Reaction data for the aldol condensation of 4-nitrobenzaldehyde and acetone performed with acid-functionalized carboxylated CNC intermediate materials (CNC-s-cooh, CNC-ds-cooh, CNC-ds-COOH). Negligible activity was observed as conversion of 4NB by GC-MS was noisy and under 5%. Representative reaction data from a fairly highly active catalyst (CNC-ds-COOH-DAP) and a catalyst with low activity (CNC-s-cooh-dbDAP) are included here for comparison. These data are consistent with results from our previous work,[138] where similar acid-only functionalized CNCs were shown to be not active for the aldol condensation reaction under the conditions employed.

B.5.1 Dynamic Light Scattering (DLS) Analysis of CNC Agglomeration from Desulfation

Dynamic light scattering was used to investigate the effect of desulfation on particle agglomeration. DLS measurements were taken with a Malvern Zetasizer Nano of CNC suspensions of <0.1 wt% CNC. A significant increase in hydrodynamic radius was noted with high degrees of desulfation as a result of the near complete removal of charged surface species. With additional functionalization, the final catalyst materials generally displayed a reduction in agglomerate size when compared to their respective starting materials. Significant increases in visual opacity were noted for highly desulfated (DS) CNC suspensions in particular. CNC-DS did not form a stable suspension in water and some settling was seen with time.

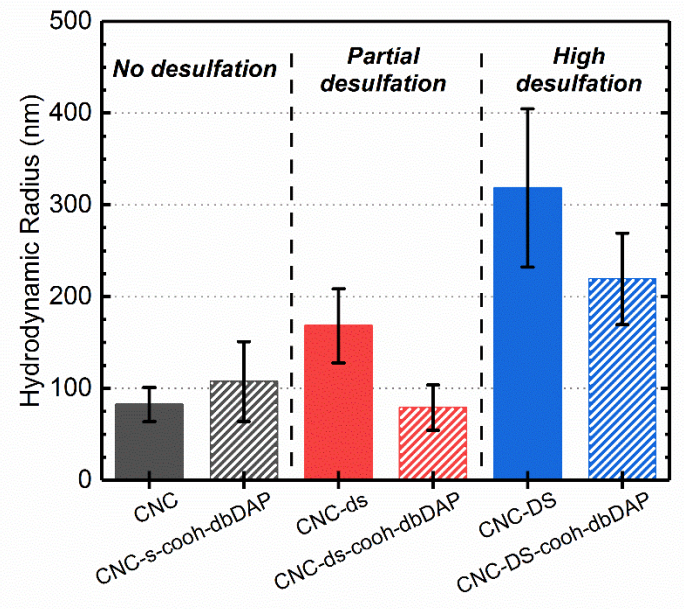

Figure B.10 – Hydrodynamic radii of CNC starting materials (unmodified or with partial or high degrees of desulfation) as well as the resulting series of comparable catalyst materials from DLS.

B.5.2 Reaction Product and Selectivity Analyses

Table B-3 – Selectivities to aldol condensation dehydration products (3 or 6 below; 2 in main text) for all catalysts for reactions of 4-nitrobenzaldehyde (4NB) and furfural (furf) determined by crude ^{1}H NMR of product mixtures collected after 6 h of reaction.

Catalyst	Selectivity to 2 (4NB-AC) (%)	Selectivity to 2 (Furf-AC) (%)
CNC-s-cooh-dbDAP	53	92
CNC-ds-cooh-dbDAP	78	98
CNC-DS-cooh-dbDAP	43	85
CNC-ds-COOH-dbDAP	83	77
CNC-s-cooh-DAP	87	79
CNC-ds-COOH-DAP	88	69
CNC-ds-COOH-DAP-HT	88	81
SBA-APS	27	72
SBA-COOH-APS	22	60

^{1}H NMR analysis of aldol condensation reactions

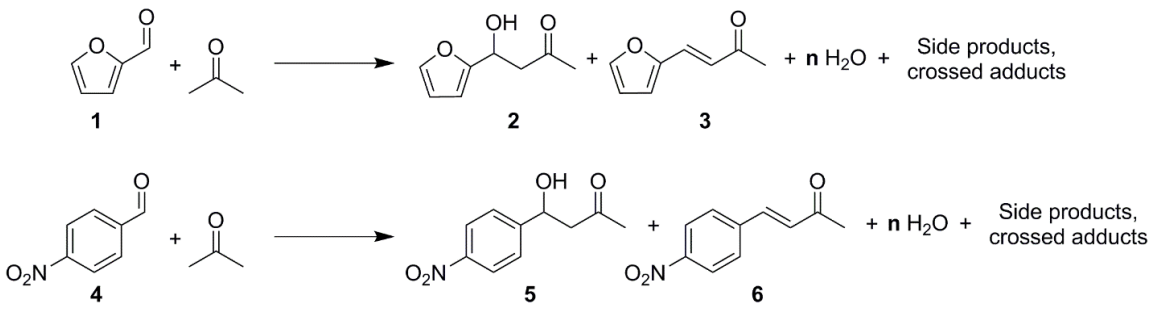

Figure B.11 – Reaction schemes for the aldol condensations of furfural (1) and 4-nitrobenzaldehyde (4) with acetone and their major products. Bolded assignments (below) indicate the most distinct peaks in crude reaction mixtures which were used for quantitative integration. Selectivity to the dehydration products (3 or 6 above) discussed in the main text was calculated as the ratio of the dehydration product to the sum of the aldol (2 or 5 above) and the dehydration products.

1. furfural: ^{1}H (400 MHz, DMSO-d_6) δ **9.62 (d, *J* = 0.8 Hz, 1H)**, 8.11 (quin, *J* = 0.8 Hz, 1H), 7.55 (dd, *J* = 3.6 Hz, 1H), 6.79 (dd, *J* = 3.6 Hz, 1H)

2. 4-(furan-2-yl)-4-hydroxybutan-2-one: ^{1}H (400 MHz, DMSO-d_6) δ 7.90 (d, *J* = 1.5 Hz, 1H), 7.57 (dd, *J* = 1.8 Hz, 1H), 6.38 (dd, *J* = 3.2 Hz, 1H), 5.49 (d, *J* = 5.6 Hz, 1H), **4.98 (dt, *J* = 8.2 Hz, 1H)**, 2.83 (t, *J* = 6.4 Hz, 2H), 2.13 (s, 3H)

3. 4-(2-Furyl)-3-buten-2-one: ^{1}H (400 MHz, DMSO-d_6) δ 7.87 (d, *J* = 1.5 Hz, 1H), 7.44 (d, *J* = 16.2 Hz, 1H), 6.98 (d, *J* = 3.5 Hz, 1H), 6.66 (dd, *J* = 3.5 Hz, 1H), 6.48 (d, *J* = 16.1 Hz, 1H), **2.29 (s, 3H)**

4. 4-nitrobenzaldehyde: ^{1}H (400 MHz, DMSO-d_6) δ **10.17 (s, 1H)**, 8.43 (dt, *J* = 8.7 Hz, 2H), 8.17 (d, *J* = 8.8 Hz, 2H)

5. 4-hydroxy-4-(4-nitrophenyl)butan-2-one: ^{1}H (400 MHz, DMSO-d_6) δ 8.20 (dt, *J* = 8.8 Hz, 2H), 7.64 (dt, *J* = 8.5 Hz, 2H), 5.72 (d, *J* = 4.8 Hz, 1H), **5.15 (q, *J* = 4.9 Hz, 1H)**, 2.75 (d, *J* = 6.6 Hz, 2H), 2.14 (s, 3H)

6. 4-(4-nitrophenyl)but-3-en-2-one: ^{1}H (400 MHz, DMSO-d_6) δ 8.27 (dt, *J* = 8.9 Hz, 2H), 8.00 (dt, *J* = 8.8 Hz, 2H), 7.73 (d, *J* = 16.5 Hz, 1H), 7.00 (d, *J* = 16.4 Hz, 1H), **2.38 (s, 3H)**

1,4-dimethoxybenzene (internal standard): ^{1}H (400 MHz, DMSO-d_6) δ **6.86 (s, 4H)**, 3.69 (s, 6H)

B.5.3 Time-resolved Aldol Condensation Selectivity and Catalyst Recycling Tests

Aldol condensation reactions of 4NB and acetone were performed at conditions identical to those in the main text, but the reactions were scaled to 16 mL to allow for sufficiently voluminous aliquots to be concentrated and analyzed via NMR. The CNC catalyst activity of this experiment was in the low range expected for this material, whereas SBA-APS kinetics were among the fastest seen in repeated reactions. For both materials, selectivities were approximately constant over the course of the 6 h reaction (Figure B.12a, b below). For the CNC catalysts, the dehydration step may occur at the catalyst surface without intermediate diffusion of **1** to the bulk. It is also possible that the bound aldol intermediate (Figure B.8) undergoes the dehydration while still bound and in proximity to a nearby acid site before desorbing from the amine site. The consistency of the selectivities, for both the CNC and SBA-APS catalyst, indicates that the selectivity is primarily a function of the catalyst and reaction environment and not of reaction time. This is additional evidence that the bifunctional active site of the CNC acid–base catalysts is superior to that of the silanol–amine acid–base nature of the aminosilica catalysts.

A quantity of the recovered catalyst (filtered, washed, air dried, and stored under Ar atmosphere) equaling that required for 10 mol% fresh catalyst was used in a 4 mL reaction for each material (Figure B.12c,d). Recovered CNC catalysts were orange even with significant washing with acetone after recovered, indicative of strongly bound reactant (4NB). For all reactions performed with CNC catalysts in this work, recovered catalysts were characteristically orange and therefore had residual bound substrates. Catalysts selective for the dehydrated product (CNC catalysts) had orange to dark orange reaction solutions, whereas those selective for the aldol product (SBA-15 catalysts) were typically

yellow. The SBA-APS catalyst was white to faintly yellow after recovery and washing. Both catalysts retained some activity but with ~70 % reduction in activity upon reuse with minimal processing and regeneration between reactions.

In the case of the CNC catalysts, this deactivation may be related to the irreversible agglomeration which occurs upon drying the catalysts. They were filtered, washed, and dried on filter paper before storage and re-use. Qualitatively, the CNCs appeared less homogeneously dispersed in the reaction mixture in the recycle reaction. Strong binding of 4-nitrobenzaldehyde, as indicated by the orange color of the catalyst persisting with washing, could poison some base sites and reduce the overall activity. Finally, a mass of catalyst identical to that of 10 mol% fresh catalyst was used, and the presence of residual bound surface species would mean that the mass of actual catalyst would be reduced.

For SBA-APS, there is similarly the possibility of strongly bound residual substrate blocking actives sites. It has been shown that water can lead to the hydrolysis of grafted silanes and deactivate aminosilica organocatalysts.[188] As water is produced in the condensation reaction, this may have led to a partial removal of grafted silanes and therefore active sites. These factors may have contributed to the reduction in activity with recycle.

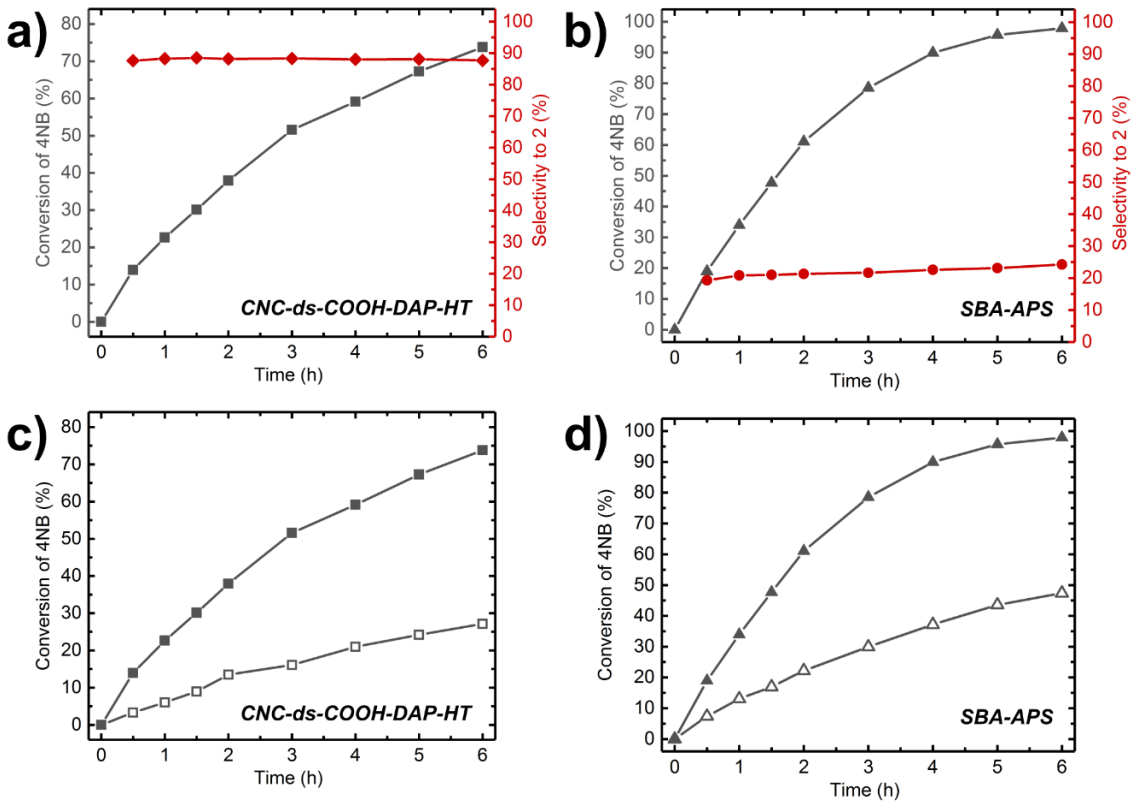

Figure B.12 – a) and b) Time course conversion and selectivity data from scaled kinetics experiments of the optimized CNC catalyst (CNC-ds-COOH-DAP-HT) and SBA-APS. Selectivity to the dehydrated aldol product (6 above (Scheme S1); 2 in main text) was determined from the yield of 2 divided by the sum of the yields of the two major products, 1 and 2. c) and d) Catalyst recyclability tests using recovered catalyst from the scaled reactions for time-resolved selectivity. Reaction kinetics using fresh catalyst (solid symbols) and once recycled catalyst (open symbols) are shown.

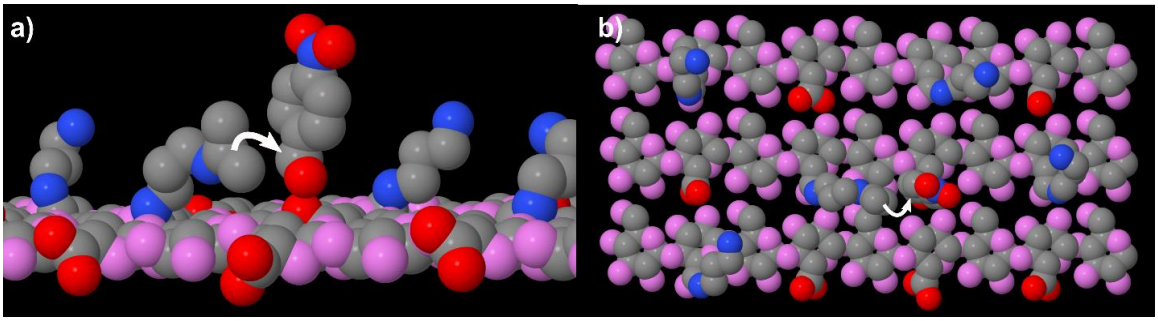

Figure B.13 – (a) Side and (b) top-down views of the C-C bond forming step cooperatively catalyzed by a primary amine and carboxylic acid on a small portion of a (100) surface of a functionalized CNC catalyst. This image demonstrates the sufficient proximity of the nucleophilic enamine and carboxylic acid-activated aldehyde of 4-nitrobenzaldehyde in this step. Red atoms are oxygen in carboxylic acids, blue atoms are nitrogen in amide-linked diamines, grey atoms are carbon, and violet atoms are all other oxygen. Hydrogen atoms are omitted for simplicity and atomic radii are specified as 75% of the Van der Waals radii. This intra-chain cooperativity on the (100) surface has the largest average NH_2 – COOH spacing (δ_3 = 11.0 $\pm$ 2.3 Å) of the four likely cooperative pairs described in Figure 3.6, indicating that the other three pairs would be sufficiently proximal for cooperative catalytic function. Functional groups and reactants were manually positioned and automatically minimized in Jmol.

APPENDIX C. CHAPTER 4 SUPPORTING INFORMATION

C.1 Microfibrillated Cellulose Processing to Cellulose Nanofibrils

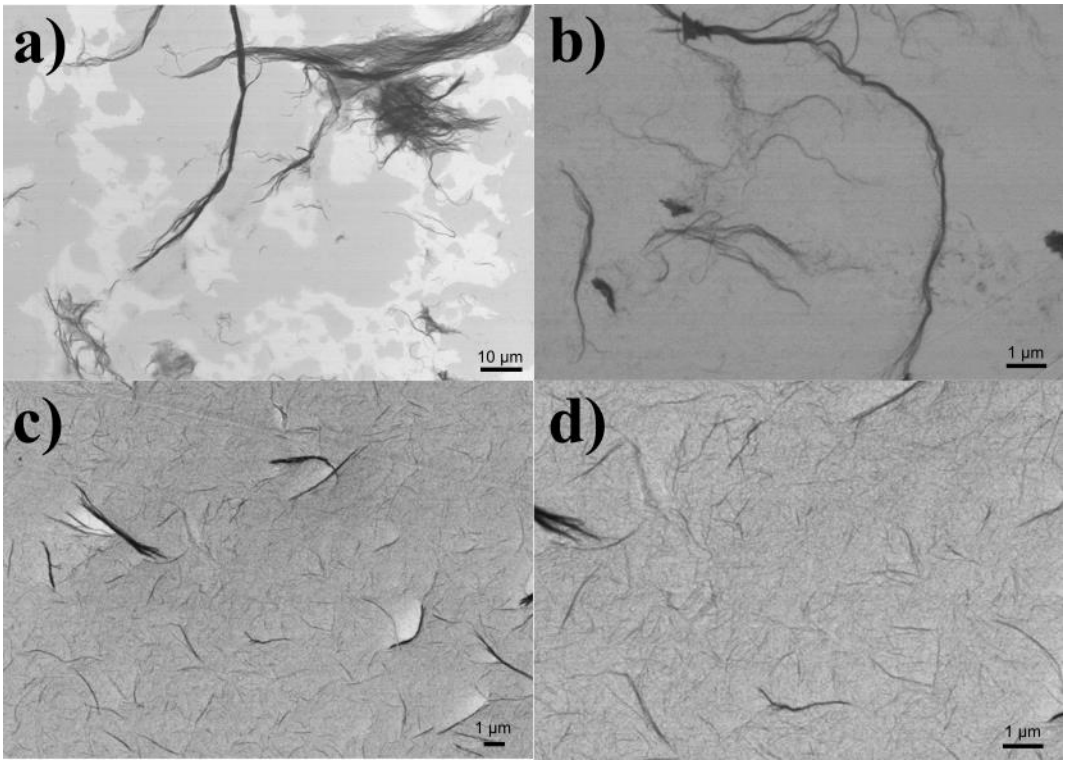

Figure C.1 – SEM images of TEMPO-oxidized microfibrillated cellulose before (a,b) and after (c,d) homogenization. After homogenization, primarily highly disperse fibers of nanoscale widths and lengths of several microns were obtained. No extremely large fibers of the scale seen in MFC and TOMFC were visible.

a) 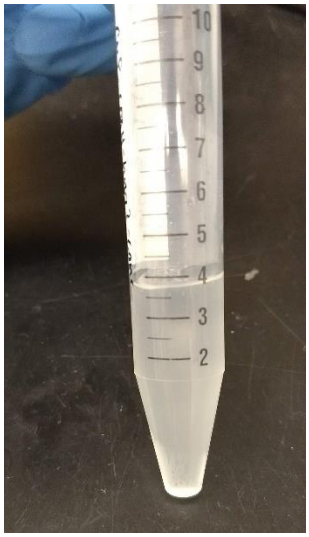 b) 

Figure C.2 – A 1.2 wt% suspension of TOCNF (a) before and (b) after a single freeze-thaw. The freeze-thawed TOCNF suspension formed a stable, invertible hydrogel.

C.2 Aldol Condensation Reaction and Selectivity

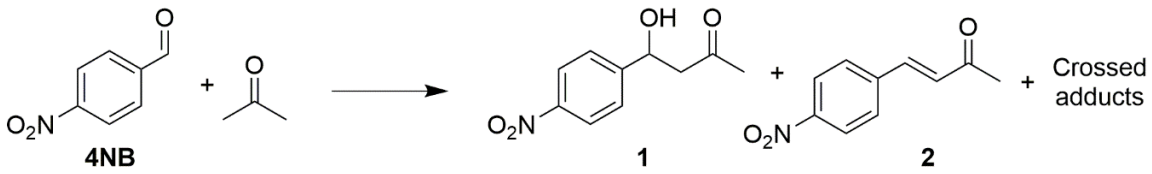

Figure C.3 – Aldol condensation reaction scheme of 4-nitrobenzaldehyde (4NB) with acetone.

Table C-1 – Catalyst selectivities for the dehydrated aldol product (2, above) of the aldol condensation reaction of 4-nitrobenzaldehyde and acetone. Selectivity was evaluated after 4 h of reaction by ^{1}H NMR analysis of a crude mixture of the reaction products

catalyst	phase	selectivity to 2 (%)
TOCNF-rDAP(ref)	homogeneous	88
TOCNF-DAP	homogeneous	82
TOCNF-rDAP2	homogeneous	88
TOCNF-DAP-TPA_1-1	aerogel	83
TOCNF-DAP-TPA_3-1	aerogel	83
TOCNF-rDAP2_CMC	aerogel	90
TOCNF-rDAP2-XDA	aerogel	95
TOCNF-PEI	aerogel	N/A

C.3 Additional Aerogel Characterization

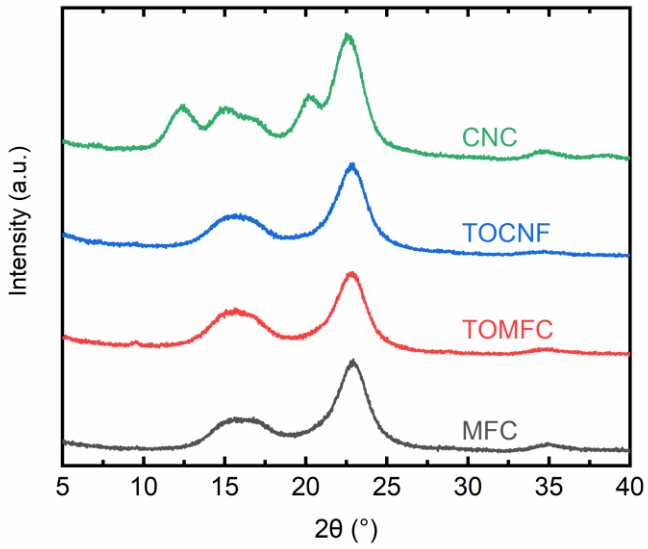

Figure C.4 – X-ray diffraction patterns of the MFC starting material, TEMPO-oxidized MFC (TOMFC), homogenized TEMPO-oxidized CNF (TOCNF), and sulfuric acid-derived cellulose nanocrystals.

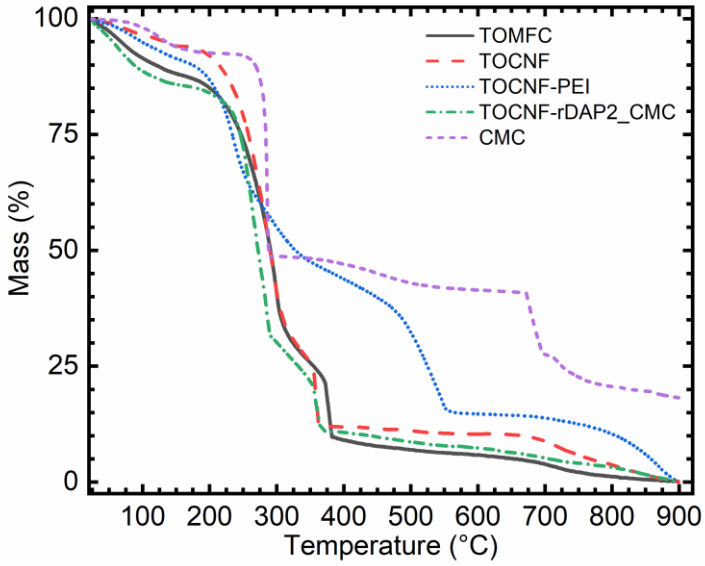

Figure C.5 – Thermogravimetric analysis (TGA) of various aerogel samples, in particular those which include a polymeric filler like PEI or CMC.

REFERENCES

(1) Milanez, D. H.; Amaral, R. M. Do; Faria, L. I. L. De; Gregolin, J. A. R. Assessing Nanocellulose Developments Using Science and Technology Indicators. *Mater. Res.* **2013**, *16* (3), 635–341. https://doi.org/10.1590/S1516-14392013005000033.

(2) Rånby, B. G.; Banderet, A.; Sillén, L. G. Aqueous Colloidal Solutions of Cellulose Micelles. *Acta Chem. Scand.* **1949**, *3*, 649–650. https://doi.org/10.3891/acta.chem.scand.03-0649.

(3) Moon, R. J.; Martini, A.; Nairn, J.; Simonsen, J.; Youngblood, J. Cellulose Nanomaterials Review: Structure, Properties and Nanocomposites. *Chem. Soc. Rev.* **2011**, *40* (7), 3941–3994. https://doi.org/10.1039/c0cs00108b.

(4) Keshk, S. M. Bacterial Cellulose Production and Its Industrial Applications. *J. Bioprocess. Biotech.* **2014**, *04* (02), 1–10. https://doi.org/10.4172/2155-9821.1000150.

(5) Hansen, E. Responding to the Bioeconomy: Business Model Innovation in the Forest Sector. In *Environmental Footprints and Eco-design of Products and Processes*; Kutnar, A., Muthu, S. S., Eds.; Springer Singapore: Singapore, 2016; pp 227–248. https://doi.org/10.1007/978-981-10-0655-5_7.

(6) Woodall, C. W.; Ince, P. J.; Skog, K. E.; Aguilar, F. X.; Keegan, C. E.; Sorenson, C. B.; Hodges, D. G.; Smith, W. B. An Overview of the Forest Products Sector Downturn in the United States. *For. Prod. J.* **2012**, *61* (8), 595–603.

(7) Ollikainen, M. Forestry in Bioeconomy – Smart Green Growth for the Humankind. *Scand. J. For. Res.* **2014**, *29* (4), 360–336. https://doi.org/10.1080/02827581.2014.926392.

(8) Fatih Demirbas, M. Biorefineries for Biofuel Upgrading: A Critical Review. *Appl. Energy* **2009**, *86* (SUPPL. 1), S151–S161. https://doi.org/10.1016/j.apenergy.2009.04.043.

(9) Harfouche, A.; Khoury, S.; Fabbrini, F.; Mugnozza, G. S. Forest Biotechnology Advances to Support Global Bioeconomy. *Ann. Silivicultural Res.* **2014**, *38* (2), 42–50. https://doi.org/10.12899/asr-1012.

(10) Perlack, R. D.; Stokes, B. J. *US Billion Ton Update: Biomass Supply for a Bioenergy and Bioproducts Industry (Executive Summary)*; Oak Ridge, TN, 2011; Vol. 7. https://doi.org/10.1089/ind.2011.7.375.

(11) Shatkin, J. A.; Wegner, T. H.; Bilek, E.; Cowie, J. Market Projections of Cellulose Nanomaterial-Enabled Products - Part 1: Applications. *Tappi J.* **2014**, *13* (5), 9–16.

(12) Moon, R. J.; Schueneman, G. T.; Simonsen, J. Overview of Cellulose Nanomaterials, Their Capabilities and Applications. *Jom* **2016**, *68* (9), 2383–2394. https://doi.org/10.1007/s11837-016-2018-7.

(13) Nechyporchuk, O.; Belgacem, M. N.; Bras, J. Production of Cellulose Nanofibrils: A Review of Recent Advances. *Ind. Crops Prod.* **2016**, *93*, 2–25. https://doi.org/10.1016/j.indcrop.2016.02.016.

(14) Habibi, Y.; Lucia, L. A.; Rojas, O. J. Cellulose Nanocrystals: Chemistry, Self-Assembly, and Applications. *Chem. Rev.* **2010**, *110* (6), 3479–3500. https://doi.org/10.1021/cr900339w.

(15) Peng, B. L.; Dhar, N.; Liu, H. L.; Tam, K. C. Chemistry and Applications of Nanocrystalline Cellulose and Its Derivatives: A Nanotechnology Perspective. *Can. J. Chem. Eng.* **2011**, *89* (5), 1191–1206. https://doi.org/10.1002/cjce.20554.

(16) Mariano, M.; El Kissi, N.; Dufresne, A. Cellulose Nanocrystals and Related Nanocomposites: Review of Some Properties and Challenges. *J. Polym. Sci. Part B Polym. Phys.* **2014**, *52* (12), 791–806. https://doi.org/10.1002/polb.23490.

(17) Zhang, Y. H. P. Reviving the Carbohydrate Economy via Multi-Product Lignocellulose Biorefineries. *J. Ind. Microbiol. Biotechnol.* **2008**, *35* (5), 367–375. https://doi.org/10.1007/s10295-007-0293-6.

(18) Bioenergy Technologies Office. *Biochemical Conversion: Using Enzymes, Microbes, and Catalysts to Make Fuels and Chemicals*; 2013.

(19) Climent, M. J.; Corma, A.; Iborra, S. Conversion of Biomass Platform Molecules into Fuel Additives and Liquid Hydrocarbon Fuels. *Green Chem.* **2014**, *16* (2), 516. https://doi.org/10.1039/c3gc41492b.

(20) Energy, U. S. D. of. *Integrated Biorefineries: Reducing Investment Risk in Novel Technology*; 2014.

(21) Huh, S.; Chen, H. T.; Wiench, J. W.; Pruski, M.; Lin, V. S. Y. Cooperative Catalysis by General Acid and Base Bifunctionalized Mesoporous Silica Nanospheres. *Angew. Chem., Int. Ed.* **2005**, *44* (12), 1826–1830. https://doi.org/10.1002/anie.200462424.

(22) Margelefsky, E. L.; Zeidan, R. K.; Davis, M. E. Cooperative Catalysis by Silica-Supported Organic Functional Groups. *Chem. Soc. Rev.* **2008**, *37* (6), 1118–1126. https://doi.org/10.1039/b710334b.

(23) Ferré, M.; Pleixats, R.; Wong Chi Man, M.; Cattoën, X.; Seifert, A.; Ernst, S.; Thiel, W. R.; Martinez, J.; Martra, G.; Toulemon, D.; et al. Recyclable Organocatalysts Based on Hybrid Silicas. *Green Chem.* **2016**, *18* (4), 881–922. https://doi.org/10.1039/C5GC02579F.

(24) Brinchi, L.; Cotana, F.; Fortunati, E.; Kenny, J. M. Production of Nanocrystalline Cellulose from Lignocellulosic Biomass: Technology and Applications. *Carbohydr. Polym.* **2013**, *94* (1), 154–169. https://doi.org/10.1016/j.carbpol.2013.01.033.

(25) Sacui, I. A.; Nieuwendaal, R. C.; Burnett, D. J.; Stranick, S. J.; Jorfi, M.; Weder, C.; Foster, E. J.; Olsson, R. T.; Gilman, J. W. Comparison of the Properties of Cellulose Nanocrystals and Cellulose Nanofibrils Isolated from Bacteria, Tunicate, and Wood Processed Using Acid, Enzymatic, Mechanical, and Oxidative Methods. *ACS Appl. Mater. Interfaces* **2014**, *6* (9), 6127–6138. https://doi.org/10.1021/am500359f.

(26) Turbak, A.; Snyder, F.; Sandberg, K. Microfibrillated Cellulose, February 22, 1983.

(27) Isogai, A.; Saito, T.; Fukuzumi, H. TEMPO-Oxidized Cellulose Nanofibers. *Nanoscale* **2011**, *3* (1), 71–85. https://doi.org/10.1039/c0nr00583e.

(28) Saito, T.; Nishiyama, Y.; Putaux, J. L.; Vignon, M.; Isogai, A. Homogeneous Suspensions of Individualized Microfibrils from TEMPO-Catalyzed Oxidation of Native Cellulose. *Biomacromolecules* **2006**, *7* (6), 1687–1691. https://doi.org/10.1021/bm060154s.

(29) Habibi, Y. Key Advances in the Chemical Modification of Nanocelluloses. *Chem. Soc. Rev.* **2014**, *43* (5), 1519–1542. https://doi.org/10.1039/C3CS60204D.

(30) Eyley, S.; Thielemans, W. Surface Modification of Cellulose Nanocrystals. *Nanoscale* **2014**, *6* (3), 7764–7779. https://doi.org/10.1007/s11705-007-0041-5.

(31) Foster, E. J.; Moon, R. J.; Agarwal, U. P.; Bortner, M. J.; Bras, J.; Camarero-Espinosa, S.; Chan, K. J.; Clift, M. J. D.; Cranston, E. D.; Eichhorn, S. J.; et al. Current Characterization Methods for Cellulose Nanomaterials. *Chem. Soc. Rev.* **2018**, *47* (8), 2609–2679. https://doi.org/10.1039/c6cs00895j.

(32) Stenstad, P.; Andresen, M.; Tanem, B. S.; Stenius, P. Chemical Surface Modifications of Microfibrillated Cellulose. *Cellulose* **2008**, *15* (1), 35–45. https://doi.org/10.1007/s10570-007-9143-y.

(33) Missoum, K.; Belgacem, M. N.; Bras, J. Nanofibrillated Cellulose Surface Modification: A Review. *Materials* **2013**, *6* (5), 1745–1766. https://doi.org/10.3390/ma6051745.

(34) Eyley, S.; Thielemans, W. Imidazolium Grafted Cellulose Nanocrystals for Ion Exchange Applications. *Chem. Commun.* **2011**, *47* (14), 4177–4179. https://doi.org/10.1039/c0cc05359g.

(35) Çetin, N. S.; Tingaut, P.; Özmen, N.; Henry, N.; Harper, D.; Dadmun, M.; Sèbe, G. Acetylation of Cellulose Nanowhiskers with Vinyl Acetate under Moderate Conditions. *Macromol. Biosci.* **2009**, *9* (10), 997–1003. https://doi.org/10.1002/mabi.200900073.

(36) Azzam, F.; Heux, L.; Putaux, J. L.; Jean, B. Preparation by Grafting onto, Characterization, and Properties of Thermally Responsive Polymer-Decorated Cellulose Nanocrystals. *Biomacromolecules* **2010**, *11* (12), 3652–3659. https://doi.org/10.1021/bm101106c.

(37) Araki, J.; Wada, M.; Kuga, S. Steric Stabilization of a Cellulose Microcrystal Suspension by Poly(Ethylene Glycol) Grafting. *Langmuir* **2001**, *17* (1), 21–27. https://doi.org/10.1021/la001070m.

(38) Nielsen, L. J.; Eyley, S.; Thielemans, W.; Aylott, J. W. Dual Fluorescent Labelling of Cellulose Nanocrystals for PH Sensing. *Chem. Commun.* **2010**, *46* (47), 8929–8931. https://doi.org/10.1039/c0cc03470c.

(39) Zhou, P.; Wang, H.; Yang, J.; Tang, J.; Sun, D.; Tang, W. Bacteria Cellulose Nanofibers Supported Palladium(0) Nanocomposite and Its Catalysis Evaluation in Heck Reaction. *Ind. Eng. Chem. Res.* **2012**, *51* (16), 5743–5748. https://doi.org/10.1021/ie300395q.

(40) Yan, W.; Chen, C.; Wang, L.; Zhang, D.; Li, A.-J.; Yao, Z.; Shi, L.-Y. Facile and Green Synthesis of Cellulose Nanocrystal-Supported Gold Nanoparticles with Superior Catalytic Activity. *Carbohydr. Polym.* **2016**, *140*, 66–73. https://doi.org/10.1016/j.carbpol.2015.12.049.

(41) Cirtiu, C. M.; Dunlop-Brière, A. F.; Moores, A. Cellulose Nanocrystallites as an Efficient Support for Nanoparticles of Palladium: Application for Catalytic Hydrogenation and Heck Coupling under Mild Conditions. *Green Chem.* **2011**, *13* (2), 288–291. https://doi.org/10.1039/c0gc00326c.

(42) Lavoine, N.; Desloges, I.; Dufresne, A.; Bras, J. Microfibrillated Cellulose - Its Barrier Properties and Applications in Cellulosic Materials: A Review. *Carbohydr. Polym.* **2012**, *90* (2), 735–764. https://doi.org/10.1016/j.carbpol.2012.05.026.

(43) De France, K. J.; Hoare, T.; Cranston, E. D. Review of Hydrogels and Aerogels Containing Nanocellulose. *Chem. Mater.* **2017**, *29* (11), 4609–4631. https://doi.org/10.1021/acs.chemmater.7b00531.

(44) Way, A. E.; Hsu, L.; Shanmuganathan, K.; Weder, C.; Rowan, S. J. PH-Responsive Cellulose Nanocrystal Gels and Nanocomposites. *ACS Macro Lett.* **2012**, *1* (8), 1001–1006. https://doi.org/10.1021/mz3003006.

(45) Oechsle, A. L.; Lewis, L.; Hamad, W. Y.; Hatzikiriakos, S. G.; MacLachlan, M. J. CO2-Switchable Cellulose Nanocrystal Hydrogels. *Chem. Mater.* **2018**, *30* (2), 376–385. https://doi.org/10.1021/acs.chemmater.7b03939.

(46) Yang, J.; Xu, F.; Han, C. R. Metal Ion Mediated Cellulose Nanofibrils Transient Network in Covalently Cross-Linked Hydrogels: Mechanistic Insight into Morphology and Dynamics. *Biomacromolecules* **2017**, *18* (3), 1019–1028. https://doi.org/10.1021/acs.biomac.6b01915.

(47) Hu, Z.; Cranston, E. D.; Ng, R.; Pelton, R. Tuning Cellulose Nanocrystal Gelation with Polysaccharides and Surfactants. *Langmuir* **2014**, *30* (10), 2684–2692. https://doi.org/10.1021/la404977t.

(48) Zhang, J.; Liu, T.; Liu, Z.; Wang, Q. Facile Fabrication of Tough Photocrosslinked Polyvinyl Alcohol Hydrogels with Cellulose Nanofibrils Reinforcement. *Polymer* **2019**, *173* (February), 103–109. https://doi.org/10.1016/j.polymer.2019.04.028.

(49) Chang, C.; Zhang, L.; Zhou, J.; Zhang, L.; Kennedy, J. F. Structure and Properties of Hydrogels Prepared from Cellulose in NaOH/Urea Aqueous Solutions. *Carbohydr. Polym.* **2010**, *82* (1), 122–127. https://doi.org/10.1016/j.carbpol.2010.04.033.

(50) Yang, X.; Cranston, E. D. Chemically Cross-Linked Cellulose Nanocrystal Aerogels with Shape Recovery and Superabsorbent Properties. *Chem. Mater.* **2014**, *26* (20), 6016–6025. https://doi.org/10.1021/cm502873c.

(51) Jiang, F.; Hsieh, Y. Lo. Super Water Absorbing and Shape Memory Nanocellulose Aerogels from TEMPO-Oxidized Cellulose Nanofibrils via Cyclic Freezing-Thawing. *J. Mater. Chem. A* **2014**, *2* (2), 350–359. https://doi.org/10.1039/c3ta13629a.

(52) Lewis, L.; Hatzikiriakos, S. G.; Hamad, W. Y.; MacLachlan, M. J. Freeze–Thaw Gelation of Cellulose Nanocrystals. *ACS Macro Lett.* **2019**, 486–491. https://doi.org/10.1021/acsmacrolett.9b00140.

(53) Geidobler, R.; Winter, G. Controlled Ice Nucleation in the Field of Freeze-Drying: Fundamentals and Technology Review. *Eur. J. Pharm. Biopharm.* **2013**, *85* (2), 214–222. https://doi.org/10.1016/j.ejpb.2013.04.014.

(54) Zhang, H.; Hussain, I.; Brust, M.; Butler, M. F.; Rannard, S. P.; Cooper, A. I. Aligned Two- and Three-Dimensional Structures by Directional Freezing of Polymers and Nanoparticles. *Nat. Mater.* **2005**, *4* (10), 787–793. https://doi.org/10.1038/nmat1487.

(55) Chau, M.; De France, K. J.; Kopera, B.; Machado, V. R.; Rosenfeldt, S.; Reyes, L.; Chan, K. J. W.; Förster, S.; Cranston, E. D.; Hoare, T.; et al. Composite Hydrogels with Tunable Anisotropic Morphologies and Mechanical Properties. *Chem. Mater.* **2016**, *28* (10), 3406–3415. https://doi.org/10.1021/acs.chemmater.6b00792.

(56) Peng, Y.; Gardner, D. J.; Han, Y. Drying Cellulose Nanofibrils: In Search of a Suitable Method. *Cellulose* **2012**, *19* (1), 91–102. https://doi.org/10.1007/s10570-011-9630-z.

(57) Heath, L.; Thielemans, W. Cellulose Nanowhisker Aerogels. *Green Chem.* **2010**, *12* (8), 1448–1453. https://doi.org/10.1039/c0gc00035c.

(58) Josset, S.; Hansen, L.; Orsolini, P.; Griffa, M.; Kuzior, O.; Weisse, B.;

Zimmermann, T.; Geiger, T. Microfibrillated Cellulose Foams Obtained by a Straightforward Freeze–Thawing–Drying Procedure. *Cellulose* **2017**, *24* (9), 3825–3842. https://doi.org/10.1007/s10570-017-1377-8.

(59) Zhang, X.; Liu, M.; Wang, H.; Yan, N.; Cai, Z.; Yu, Y. Ultralight, Hydrophobic, Anisotropic Bamboo-Derived Cellulose Nanofibrils Aerogels with Excellent Shape Recovery via Freeze-Casting. *Carbohydr. Polym.* **2019**, *208* (8), 232–240. https://doi.org/10.1016/j.carbpol.2018.12.073.

(60) Tripathi, A.; Parsons, G. N.; Rojas, O. J.; Khan, S. A. Featherlight, Mechanically Robust Cellulose Ester Aerogels for Environmental Remediation. *ACS Omega* **2017**, *2* (8), 4297–4305. https://doi.org/10.1021/acsomega.7b00571.

(61) Wu, Z. Y.; Li, C.; Liang, H. W.; Chen, J. F.; Yu, S. H. Ultralight, Flexible, and Fire-Resistant Carbon Nanofiber Aerogels from Bacterial Cellulose. *Angew. Chem., Int. Ed.* **2013**, *52* (10), 2925–2929. https://doi.org/10.1002/anie.201209676.

(62) Kobayashi, Y.; Saito, T.; Isogai, A. Aerogels with 3D Ordered Nanofiber Skeletons of Liquid-Crystalline Nanocellulose Derivatives as Tough and Transparent Insulators. *Angew. Chem. Int. Ed. Engl.* **2014**, *53* (39), 10394–10397. https://doi.org/10.1002/anie.201405123.

(63) Rocha, I.; Ferraz, N.; Mihranyan, A.; Strømme, M.; Lindh, J. Sulfonated Nanocellulose Beads as Potential Immunosorbents. *Cellulose* **2018**, *25* (3), 1899–1910. https://doi.org/10.1007/s10570-018-1661-2.

(64) Song, J.; Chen, C.; Yang, Z.; Kuang, Y.; Li, T.; Li, Y.; Huang, H.; Kierzewski, I.; Liu, B.; He, S.; et al. Highly Compressible, Anisotropic Aerogel with Aligned Cellulose Nanofibers. *ACS Nano* **2018**, *12* (1), 140–147. https://doi.org/10.1021/acsnano.7b04246.

(65) Tang, Y.; Qiu, S.; Wu, C.; Miao, Q.; Zhao, K. Freeze Cast Fabrication of Porous Ceramics Using Tert-Butyl Alcohol-Water Crystals as Template. *J. Eur. Ceram. Soc.* **2016**, *36* (6), 1513–1518. https://doi.org/10.1016/j.jeurceramsoc.2015.12.047.

(66) Harris, K. R.; Newitt, P. J. Diffusion and Structure in Water−Alcohol Mixtures: Water + Tert -Butyl Alcohol (2-Methyl-2-Propanol) . *J. Phys. Chem. A* **2002**, *103* (33), 6508–6513. https://doi.org/10.1021/jp990659v.

(67) Fu, T.; Montes, F.; Suraneni, P.; Youngblood, J.; Weiss, J. The Influence of Cellulose Nanocrystals on the Hydration and Flexural Strength of Portland Cement Pastes. *Polymers (Basel).* **2017**, *9* (9). https://doi.org/10.3390/polym9090424.

(68) Dufresne, A. Polysaccharide Nano Crystal Reinforced Nanocomposites. *Can. J. Chem.* **2008**, *86* (6), 484–494. https://doi.org/10.1139/v07-152.

(69) Saito, T.; Kumamoto, Y.; Fukuzumi, H.; Iwata, T.; Isogai, A. Transparent and High Gas Barrier Films of Cellulose Nanofibers Prepared by TEMPO-Mediated

Oxidation. *Biomacromolecules* **2008**, *10* (1), 162–165. https://doi.org/10.1021/bm801065u.

(70) Wang, J.; Gardner, D. J.; Stark, N. M.; Bousfield, D. W.; Tajvidi, M.; Cai, Z. Moisture and Oxygen Barrier Properties of Cellulose Nanomaterial-Based Films. *ACS Sustain. Chem. Eng.* **2018**, *6* (1), 49–70. https://doi.org/10.1021/acssuschemeng.7b03523.

(71) Satam, C. C.; Irvin, C. W.; Lang, A. W.; Jallorina, J. C. R.; Shofner, M. L.; Reynolds, J. R.; Meredith, J. C. Spray-Coated Multilayer Cellulose Nanocrystal - Chitin Nanofiber Films for Barrier Applications. *ACS Sustain. Chem. Eng.* **2018**, *6* (8), 10637–10644. https://doi.org/10.1021/acssuschemeng.8b01536.

(72) Peng, B.; Tang, J.; Luo, J.; Wang, P.; Ding, B.; Tam, K. C. Applications of Nanotechnology in Oil and Gas Industry: Progress and Perspective. *Can. J. Chem. Eng.* **2017**, *96* (1), 91–100. https://doi.org/10.1002/cjce.23042.

(73) Fereydouni, M.; Sabbaghi, S.; Saboori, R.; Zeinali, S. Effect of Polyanionic Cellulose Polymer Nanoparticles on Rheological Properties of Drilling Mud. *Int. Journalof Nanosci. Nanotechnol.* **2012**, *8* (3), 171–174.

(74) Li, M. C.; Wu, Q.; Song, K.; Qing, Y.; Wu, Y. Cellulose Nanoparticles as Modifiers for Rheology and Fluid Loss in Bentonite Water-Based Fluids. *ACS Appl. Mater. Interfaces* **2015**, *7* (8), 5009–5016. https://doi.org/10.1021/acsami.5b00498.

(75) Barrios, E.; Fox, D.; Li Sip, Y. Y.; Catarata, R.; Calderon, J. E.; Azim, N.; Afrin, S.; Zhang, Z.; Zhai, L. Nanomaterials in Advanced, High-Performance Aerogel Composites: A Review. *Polymers (Basel).* **2019**, *11* (4), 726. https://doi.org/10.3390/polym11040726.

(76) Jorfi, M.; Foster, E. J. Recent Advances in Nanocellulose for Biomedical Applications. *J. Appl. Polym. Sci.* **2015**, *132* (14), 1–19. https://doi.org/10.1002/app.41719.

(77) Roman, M. Toxicity of Cellulose Nanocrystals: A Review. *Ind. Biotechnol.* **2015**, *11* (1), 25–33. https://doi.org/10.1089/ind.2014.0024.

(78) Peppas, N. A.; Hilt, J. Z.; Khademhosseini, A.; Langer, R. Hydrogels in Biology and Medicine: From Molecular Principles to Bionanotechnology. *Adv. Mater.* **2006**, *18* (11), 1345–1360. https://doi.org/10.1002/adma.200501612.

(79) Gaharwar, A. K.; Peppas, N. A.; Khademhosseini, A. Nanocomposite Hydrogels for Biomedical Applications. *Biotechnol. Bioeng.* **2014**, *111* (3), 441–453. https://doi.org/10.1002/bit.25160.

(80) Bodin, A.; Concaro, S.; Brittberg, M.; Gatenholm, P. Bacterial Cellulose as a Potential Meniscus Implant. *J. Tissue Eng. Regen. Med.* **2007**, *1* (5), 406–408. https://doi.org/10.1002/term.51.

(81) Lv, Y.; Zhou, Y.; Shao, Z.; Liu, Y.; Wei, J.; Ye, Z. Nanocellulose-Derived Carbon Nanosphere Fibers-Based Nanohybrid Aerogel for High-Performance All-Solid-State Flexible Supercapacitors. *J. Mater. Sci. Mater. Electron.* **2019**. https://doi.org/10.1007/s10854-019-01180-9.

(82) Shi, K.; Yang, X.; Cranston, E. D.; Zhitomirsky, I. Efficient Lightweight Supercapacitor with Compression Stability. *Adv. Funct. Mater.* **2016**, *26* (35), 6437–6445. https://doi.org/10.1002/adfm.201602103.

(83) Zhang, Z.; Sèbe, G.; Rentsch, D.; Zimmermann, T.; Tingaut, P. Ultralightweight and Flexible Silylated Nanocellulose Sponges for the Selective Removal of Oil from Water. *Chem. Mater.* **2014**, *26* (8), 2659–2668. https://doi.org/10.1021/cm5004164.

(84) Jiang, F.; Hsieh, Y. Lo. Cellulose Nanofibril Aerogels: Synergistic Improvement of Hydrophobicity, Strength, and Thermal Stability via Cross-Linking with Diisocyanate. *ACS Appl. Mater. Interfaces* **2017**, *9* (3), 2825–2834. https://doi.org/10.1021/acsami.6b13577.

(85) Zhu, H.; Yang, X.; Cranston, E. D.; Zhu, S. Flexible and Porous Nanocellulose Aerogels with High Loadings of Metal-Organic-Framework Particles for Separations Applications. *Adv. Mater.* **2016**, *28* (35), 7652–7657. https://doi.org/10.1002/adma.201601351.

(86) Ma, S.; Zhang, M.; Nie, J.; Tan, J.; Song, S.; Luo, Y. Lightweight and Porous Cellulose-Based Foams with High Loadings of Zeolitic Imidazolate Frameworks-8 for Adsorption Applications. *Carbohydr. Polym.* **2019**, *208* (September 2018), 328–335. https://doi.org/10.1016/j.carbpol.2018.12.081.

(87) Tang, J.; Song, Y.; Zhao, F.; Spinney, S.; da Silva Bernardes, J.; Tam, K. C. Compressible Cellulose Nanofibril (CNF) Based Aerogels Produced via a Bio-Inspired Strategy for Heavy Metal Ion and Dye Removal. *Carbohydr. Polym.* **2019**, *208* (September 2018), 404–412. https://doi.org/10.1016/j.carbpol.2018.12.079.

(88) Kaushik, M.; Moores, A. Review: Nanocelluloses as Versatile Supports for Metal Nanoparticles and Their Applications in Catalysis. *Green Chem.* **2016**, *18* (3), 622–637. https://doi.org/10.1039/C5GC02500A.

(89) Evans, B. R.; O'Neill, H. M.; Malyvanh, V. P.; Lee, I.; Woodward, J. Palladium-Bacterial Cellulose Membranes for Fuel Cells. *Biosens. Bioelectron.* **2003**, *18* (7), 917–923. https://doi.org/10.1016/S0956-5663(02)00212-9.

(90) Koga, H.; Tokunaga, E.; Hidaka, M.; Umemura, Y.; Saito, T.; Isogai, A.; Kitaoka, T. Topochemical Synthesis and Catalysis of Metal Nanoparticles Exposed on Crystalline Cellulose Nanofibers. *Chem. Commun.* **2010**, *46* (45), 8567–8569. https://doi.org/10.1039/c0cc02754e.

(91) Araki, J.; Hida, Y. Comparison of Methods for Quantitative Determination of Silver Content in Cellulose Nanowhisker/Silver Nanoparticle Hybrids. *Cellulose* **2018**, *25*

(2), 1065–1076. https://doi.org/10.1007/s10570-017-1640-z.

(92) Wu, X.; Shi, Z.; Fu, S.; Chen, J.; Berry, R. M.; Tam, K. C. Strategy for Synthesizing Porous Cellulose Nanocrystal Supported Metal Nanocatalysts. *ACS Sustain. Chem. Eng.* **2016**, *4* (11), 5929–5935. https://doi.org/10.1021/acssuschemeng.6b00551.

(93) Chen, M.; Kang, H.; Gong, Y.; Guo, J.; Zhang, H.; Liu, R. Bacterial Cellulose Supported Gold Nanoparticles with Excellent Catalytic Properties. *ACS Appl. Mater. Interfaces* **2015**, *7* (39), 21717–21726. https://doi.org/10.1021/acsami.5b07150.

(94) Yasukawa, T.; Miyamura, H.; Kobayashi, S. Cellulose-Supported Chiral Rhodium Nanoparticles as Sustainable Heterogeneous Catalysts for Asymmetric Carbon-Carbon Bond-Forming Reactions. *Chem. Sci.* **2015**, *6* (11), 6224–6229. https://doi.org/10.1039/c5sc02510a.

(95) Kaushik, M.; Basu, K.; Benoit, C.; Cirtiu, C. M.; Vali, H.; Moores, A. Cellulose Nanocrystals as Chiral Inducers: Enantioselective Catalysis and Transmission Electron Microscopy 3D Characterization. *J. Am. Chem. Soc.* **2015**, *137* (19), 6124–6127. https://doi.org/10.1021/jacs.5b02034.

(96) Cai, J.; Kimura, S.; Wada, M.; Kuga, S. Nanoporous Cellulose as Metal Nanoparticles Support. *Biomacromolecules* **2009**, *10* (1), 87–94. https://doi.org/10.1021/bm800919e.

(97) Keshipour, S.; Khezerloo, M. Gold Nanoparticles Supported on Cellulose Aerogel as a New Efficient Catalyst for Epoxidation of Styrene. *J. Iran. Chem. Soc.* **2017**, *14* (5), 1107–1112. https://doi.org/10.1007/s13738-017-1060-x.

(98) Chook, S. W.; Chia, C. H.; Chan, C. H.; Chin, S. X.; Zakaria, S.; Sajab, M. S.; Huang, N. M. A Porous Aerogel Nanocomposite of Silver Nanoparticles-Functionalized Cellulose Nanofibrils for SERS Detection and Catalytic Degradation of Rhodamine B. *RSC Adv.* **2015**, *5* (108), 88915–88920. https://doi.org/10.1039/c5ra18806g.

(99) Saeed, R. M. Y.; Bano, Z.; Sun, J.; Wang, F.; Ullah, N.; Wang, Q. CuS-Functionalized Cellulose Based Aerogel as Biocatalyst for Removal of Organic Dye. *J. Appl. Polym. Sci.* **2019**, *136* (15), 47404. https://doi.org/10.1002/app.47404.

(100) Li, Y.; Xu, L.; Xu, B.; Mao, Z.; Xu, H.; Zhong, Y.; Zhang, L.; Wang, B.; Sui, X. Cellulose Sponge Supported Palladium Nanoparticles as Recyclable Cross-Coupling Catalysts. *ACS Appl. Mater. Interfaces* **2017**, *9* (20), 17155–17162. https://doi.org/10.1021/acsami.7b03600.

(101) Fryxell, G. E. The Synthesis of Functional Mesoporous Materials. *Inorg. Chem. Commun.* **2006**, *9* (11), 1141–1150. https://doi.org/10.1016/j.inoche.2006.06.012.

(102) Soltani Firooz, N.; Panahi, R.; Mokhtarani, B.; Yazdani, F. Direct Introduction of

Amine Groups into Cellulosic Paper for Covalent Immobilization of Tyrosinase: Support Characterization and Enzyme Properties. *Cellulose* **2017**, *24* (3), 1407–1416. https://doi.org/10.1007/s10570-017-1192-2.

(103) Serizawa, T.; Sawada, T.; Wada, M. Chirality-Specific Hydrolysis of Amino Acid Substrates by Cellulose Nanofibers. *Chem. Commun.* **2013**, *49* (78), 8827–8829. https://doi.org/10.1039/c3cc44416c.

(104) Serizawa, T.; Sawada, T.; Okura, H.; Wada, M. Hydrolytic Activities of Crystalline Cellulose Nanofibers. *Biomacromolecules* **2013**, *14* (3), 613–617. https://doi.org/10.1021/bm4000822.

(105) Tamura, Y.; Kanomata, K.; Kitaoka, T. Interfacial Hydrolysis of Acetals on Protonated TEMPO-Oxidized Cellulose Nanofibers. *Sci. Rep.* **2018**, *8* (1), 5021. https://doi.org/10.1038/s41598-018-23381-8.

(106) Kanomata, K.; Tatebayashi, N.; Habaki, X.; Kitaoka, T. Cooperative Catalysis of Cellulose Nanofiber and Organocatalyst in Direct Aldol Reactions. *Sci. Rep.* **2018**, *8* (1), 4098. https://doi.org/10.1038/s41598-018-22350-5.

(107) Dalko, P. I.; Moisan, L. In the Golden Age of Organocatalysis. *Angew. Chem., Int. Ed.* **2004**, *43* (39), 5138–5175. https://doi.org/10.1002/anie.200400650.

(108) Notz, W.; Tanaka, F.; Barbas, C. F. Enamine-Based Organocatalysis with Proline and Diamines: The Development of Direct Catalytic Asymmetric Aldol, Mannich, Michael, and Diels-Alder Reactions. *Acc. Chem. Res.* **2004**, *37* (8), 580–591. https://doi.org/10.1021/ar0300468.

(109) Shylesh, S.; Thiel, W. R. Bifunctional Acid-Base Cooperativity in Heterogeneous Catalytic Reactions: Advances in Silica Supported Organic Functional Groups. *ChemCatChem* **2011**, *3* (2), 278–287. https://doi.org/10.1002/cctc.201000353.

(110) Ferré, M.; Cattoën, X.; Wong Chi Man, M.; Pleixats, R. Recyclable Silica-Supported Proline Sulphonamide Organocatalysts for Asymmetric Direct Aldol Reaction. *ChemistrySelect* **2016**, *1* (21), 6741–6748. https://doi.org/10.1002/slct.201601859.

(111) Brunelli, N. A.; Venkatasubbaiah, K.; Jones, C. W. Cooperative Catalysis with Acid-Base Bifunctional Mesoporous Silica: Impact of Grafting and Co-Condensation Synthesis Methods on Material Structure and Catalytic Properties. *Chem. Mater.* **2012**, *24* (13), 2433–2442. https://doi.org/10.1021/cm300753z.

(112) Zeidan, R. K.; Hwang, S. J.; Davis, M. E. Multifunctional Heterogeneous Catalysts: SBA-15-Containing Primary Amines and Sulfonic Acids. *Angew. Chem., Int. Ed.* **2006**, *45* (38), 6332–6335. https://doi.org/10.1002/anie.200602243.

(113) Zeidan, R. K.; Davis, M. E. The Effect of Acid-Base Pairing on Catalysis: An Efficient Acid-Base Functionalized Catalyst for Aldol Condensation. *J. Catal.* **2007**,

247 (2), 379–382. https://doi.org/10.1016/j.jcat.2007.02.005.

(114) Shylesh, S.; Wagner, A.; Seifert, A.; Ernst, S.; Thiel, W. R. Cooperative Acid-Base Effects with Functionalized Mesoporous Silica Nanoparticles: Applications in Carbon-Carbon Bond-Formation Reactions. *Chem. - A Eur. J.* **2009**, *15* (29), 7052–7062. https://doi.org/10.1002/chem.200900851.

(115) Balakrishnan, M.; Sacia, E. R.; Bell, A. T. Syntheses of Biodiesel Precursors: Sulfonic Acid Catalysts for Condensation of Biomass-Derived Platform Molecules. *ChemSusChem* **2014**, *7* (4), 1078–1085. https://doi.org/10.1002/cssc.201300931.

(116) Lauwaert, J.; Moschetta, E. G.; Van Der Voort, P.; Thybaut, J. W.; Jones, C. W.; Marin, G. B. Spatial Arrangement and Acid Strength Effects on Acid-Base Cooperatively Catalyzed Aldol Condensation on Aminosilica Materials. *J. Catal.* **2015**, *325*, 19–25. https://doi.org/10.1016/j.jcat.2015.02.011.

(117) Kandel, K.; Althaus, S. M.; Peeraphatdit, C.; Kobayashi, T.; Trewyn, B. G.; Pruski, M.; Slowing, I. I. Substrate Inhibition in the Heterogeneous Catalyzed Aldol Condensation: A Mechanistic Study of Supported Organocatalysts. *J. Catal.* **2012**, *291*, 63–68. https://doi.org/10.1016/j.jcat.2012.04.005.

(118) Elmekawy, A. A.; Sweeney, J. B.; Brown, D. R. Efficient Synthesis of Supported Proline Catalysts for Asymmetric Aldol Reactions. *Catal. Sci. Technol.* **2015**, *5* (2), 690–696. https://doi.org/10.1039/c4cy00970c.

(119) Motokura, K.; Tada, M.; Iwasawa, Y. Heterogeneous Organic Base-Catalyzed Reactions Enhanced by Acid Supports. *J. Am. Chem. Soc.* **2007**, *129* (31), 9540–9541. https://doi.org/10.1021/ja0704333.

(120) Collier, V. E.; Ellebracht, N. C.; Lindy, G. I.; Moschetta, E. G.; Jones, C. W. Kinetic and Mechanistic Examination of Acid-Base Bifunctional Aminosilica Catalysts in Aldol and Nitroaldol Condensations. *ACS Catal.* **2016**, *6* (1), 460–468. https://doi.org/10.1021/acscatal.5b02398.

(121) Brunelli, N. A.; Jones, C. W. Tuning Acid-Base Cooperativity to Create next Generation Silica-Supported Organocatalysts. *J. Catal.* **2013**, *308*, 60–72. https://doi.org/10.1016/j.jcat.2013.05.022.

(122) Kobayashi, T.; Singappuli-Arachchige, D.; Wang, Z.; Slowing, I. I.; Pruski, M. Spatial Distribution of Organic Functional Groups Supported on Mesoporous Silica Nanoparticles: A Study by Conventional and DNP-Enhanced ^{29}Si Solid-State NMR. *Phys. Chem. Chem. Phys.* **2017**, *19* (3), 1781–1789. https://doi.org/10.1039/C6CP07642D.

(123) Hicks, J. C.; Dabestani, R.; Buchanan, A. C.; Jones, C. W. Spacing and Site Isolation of Amine Groups in 3-Aminopropyl-Grafted Silica Materials: The Role of Protecting Groups. *Chem. Mater.* **2006**, *18* (21), 5022–5032. https://doi.org/10.1021/cm061382w.

(124) Anan, A.; Sharma, K. K.; Asefa, T. Selective, Efficient Nanoporous Catalysts for Nitroaldol Condensation: Co-Placement of Multiple Site-Isolated Functional Groups on Mesoporous Materials. *J. Mol. Catal. A Chem.* **2008**, *288* (1–2), 1–13. https://doi.org/10.1016/j.molcata.2008.03.027.

(125) Sharma, K. K.; Anan, A.; Buckley, R. P.; Ouellette, W.; Asefa, T. Toward Efficient Nanoporous Catalysts: Controlling Site-Isolation and Concentration of Grafted Catalytic Sites on Nanoporous Materials with Solvents and Colorimetric Elucidation of Their Site-Isolation. *J. Am. Chem. Soc.* **2008**, *130* (1), 218–228. https://doi.org/10.1021/ja074128t.

(126) Sharma, K. K.; Buckley, R. P.; Asefa, T. Optimizing Acid-Base Bifunctional Mesoporous Catalysts for the Henry Reaction: Effects of the Surface Density and Site Isolation of Functional Groups. *Langmuir* **2008**, *24* (24), 14306–14320. https://doi.org/10.1021/la8030107.

(127) Sharma, K. K.; Asefa, T. Efficient Bifunctional Nanocatalysts by Simple Postgrafting of Spatially Isolated Catalytic Groups on Mesoporous Materials. *Angew. Chem., Int. Ed.* **2007**, *46* (16), 2879–2882. https://doi.org/10.1002/anie.200604570.

(128) Lauwaert, J.; De Canck, E.; Esquivel, D.; Thybaut, J. W.; Van Der Voort, P.; Marin, G. B. Silanol-Assisted Aldol Condensation on Aminated Silica: Understanding the Arrangement of Functional Groups. *ChemCatChem* **2014**, *6* (1), 255–264. https://doi.org/10.1002/cctc.201300742.

(129) Sun, Q.; Dai, Z.; Meng, X.; Xiao, F. S. Porous Polymer Catalysts with Hierarchical Structures. *Chem. Soc. Rev.* **2015**, *44* (17), 6018–6034. https://doi.org/10.1039/c5cs00198f.

(130) Xing, R.; Liu, N.; Liu, Y.; Wu, H.; Jiang, Y.; Chen, L.; He, M.; Wu, P. Novel Solid Acid Catalysts: Sulfonic Acid Group-Functionalized Mesostructured Polymers. *Adv. Funct. Mater.* **2007**, *17* (14), 2455–2461. https://doi.org/10.1002/adfm.200600784.

(131) Hoyt, C. B.; Sarazen, M. L.; Jones, C. W. Hydroboration of Substituted Alkynes Using a Solid Polymeric Carboxylic Acid Catalyst. *J. Catal.* **2019**, *369*, 493–500. https://doi.org/10.1016/j.jcat.2018.11.021.

(132) Hoyt, C. B.; Lee, L. C.; Cohen, A. E.; Weck, M.; Jones, C. W. Bifunctional Polymer Architectures for Cooperative Catalysis: Tunable Acid–Base Polymers for Aldol Condensation. *ChemCatChem* **2017**, *9* (1), 137–143. https://doi.org/10.1002/cctc.201601104.

(133) Huber, G. W.; Iborra, S.; Corma, A. Synthesis of Transportation Fuels from Biomass: Chemistry, Catalysts, and Engineering. *Chem. Rev.* **2006**, *106* (9), 4044–4098. https://doi.org/10.1021/cr068360d.

(134) Luterbacher, J. S.; Martin Alonso, D.; Dumesic, J. A. Targeted Chemical Upgrading of Lignocellulosic Biomass to Platform Molecules. *Green Chem.* **2014**, *16* (12), 4816–4838. https://doi.org/10.1039/C4GC01160K.

(135) Shylesh, S.; Gokhale, A. A.; Ho, C. R.; Bell, A. T. Novel Strategies for the Production of Fuels, Lubricants, and Chemicals from Biomass. *Acc. Chem. Res.* **2017**, *50* (10), 2589–2597. https://doi.org/10.1021/acs.accounts.7b00354.

(136) Verma, S.; Baig, R. B. N.; Nadagouda, M. N.; Len, C.; Varma, R. S.; Gunawan, R.; Li, C. Z.; Yamauchi, Y.; Grainger, A.; Hannah, L.; et al. Sustainable Pathway to Furanics from Biomass via Heterogeneous Organo-Catalysis. *Green Chem.* **2017**, *19* (1), 164–168. https://doi.org/10.1039/C6GC02551J.

(137) Nelson, N. C.; Chaudhary, U.; Kandel, K.; Slowing, I. I. Heterogeneous Multicatalytic System for Single-Pot Oxidation and C-C Coupling Reaction Sequences. *Top. Catal.* **2014**, *57* (10–13), 1000–1006. https://doi.org/10.1007/s11244-014-0263-y.

(138) Ellebracht, N. C.; Jones, C. W. Amine Functionalization of Cellulose Nanocrystals for Acid–Base Organocatalysis: Surface Chemistry, Cross-Linking, and Solvent Effects. *Cellulose* **2018**, *25* (11), 6495–6512. https://doi.org/10.1007/s10570-018-2043-5.

(139) Nakayama, T.; Suzuki, H.; Nishino, T. Anthocyanin Acyltransferases: Specificities, Mechanism, Phylogenetics, and Applications. *J. Mol. Catal. B Enzym.* **2003**, *23* (2–6), 117–132. https://doi.org/10.1016/S1381-1177(03)00078-X.

(140) Pihko, P. M. Activation of Carbonyl Compounds by Double Hydrogen Bonding: An Emerging Tool in Asymmetric Catalysis. *Angew. Chem., Int. Ed.* **2004**, *43* (16), 2062–2064. https://doi.org/10.1002/anie.200301732.

(141) Shylesh, S.; Hanna, D.; Gomes, J.; Krishna, S.; Canlas, C. G.; Head-Gordon, M.; Bell, A. T. Tailoring the Cooperative Acid-Base Effects in Silica-Supported Amine Catalysts: Applications in the Continuous Gas-Phase Self-Condensation of n-Butanal. *ChemCatChem* **2014**, *6* (5), 1283–1290. https://doi.org/10.1002/cctc.201301087.

(142) Lauwaert, J.; De Canck, E.; Esquivel, D.; Van Der Voort, P.; Thybaut, J. W.; Marin, G. B. Effects of Amine Structure and Base Strength on Acid-Base Cooperative Aldol Condensation. *Catal. Today* **2015**, *246*, 35–45. https://doi.org/10.1016/j.cattod.2014.08.007.

(143) Brunelli, N. A.; Didas, S. A.; Venkatasubbaiah, K.; Jones, C. W. Tuning Cooperativity by Controlling the Linker Length of Silica-Supported Amines in Catalysis and CO_2 Capture. *J. Am. Chem. Soc.* **2012**, *134* (34), 13950–13953. https://doi.org/10.1021/ja305601g.

(144) Lu, P.; Hsieh, Y. Lo. Preparation and Properties of Cellulose Nanocrystals: Rods,

Spheres, and Network. *Carbohydr. Polym.* **2010**, *82* (2), 329–336. https://doi.org/10.1016/j.carbpol.2010.04.073.

(145) Lin, N.; Huang, J.; Dufresne, A. Preparation, Properties and Applications of Polysaccharide Nanocrystals in Advanced Functional Nanomaterials: A Review. *Nanoscale* **2012**, *4* (11), 3274–3294. https://doi.org/10.1039/c2nr30260h.

(146) Hubbe, M. A.; Rojas, O. J.; Lucia, L. A.; Sain, M. Cellulosic Nanocomposites: A Review. *BioResources* **2008**, *3* (3), 929–980.

(147) Isogai, A. Wood Nanocelluloses: Fundamentals and Applications as New Bio-Based Nanomaterials. *J. Wood Sci.* **2013**, *59* (6), 449–459. https://doi.org/10.1007/s10086-013-1365-z.

(148) Rebouillat, S.; Pla, F. State of the Art Manufacturing and Engineering of Nanocellulose: A Review of Available Data and Industrial Applications. *J. Biomater. Nanobiotechnol.* **2013**, *4* (April), 165–188. https://doi.org/10.4236/jbnb.2013.42022.

(149) Goussé, C.; Chanzy, H.; Excoffier, G.; Soubeyrand, L.; Fleury, E. Stable Suspensions of Partially Silylated Cellulose Whiskers Dispersed in Organic Solvents. *Polymer* **2002**, *43* (9), 2645–2651. https://doi.org/10.1016/S0032-3861(02)00051-4.

(150) Wu, X.; Lu, C.; Zhang, W.; Yuan, G.; Xiong, R.; Zhang, X. A Novel Reagentless Approach for Synthesizing Cellulose Nanocrystal-Supported Palladium Nanoparticles with Enhanced Catalytic Performance. *J. Mater. Chem. A* **2013**, *1* (30), 8645. https://doi.org/10.1039/c3ta11236e.

(151) Rezayat, M.; Blundell, R. K.; Camp, J. E.; Walsh, D. A.; Thielemans, W. Green One-Step Synthesis of Catalytically Active Palladium Nanoparticles Supported on Cellulose Nanocrystals. *ACS Sustain. Chem. Eng.* **2014**, *2* (5), 1241–1250. https://doi.org/10.1021/sc500079q.

(152) Andresen, M.; Stenstad, P.; Møretrø, T.; Langsrud, S.; Syverud, K.; Johansson, L. S.; Stenius, P. Nonleaching Antimicrobial Films Prepared from Surface-Modified Microfibrillated Cellulose. *Biomacromolecules* **2007**, *8*, 2149–2155. https://doi.org/10.1021/bm070304e.

(153) Liu, J.; Plog, A.; Groszewicz, P.; Zhao, L.; Xu, Y.; Breitzke, H.; Stark, A.; Hoffmann, R.; Gutmann, T.; Zhang, K.; et al. Design of a Heterogeneous Catalyst Based on Cellulose Nanocrystals for Cyclopropanation: Synthesis and Solid-State NMR Characterization. *Chem. - A Eur. J.* **2015**, *21* (35), 12414–12420. https://doi.org/10.1002/chem.201501151.

(154) Tsutsumi, Y.; Koga, H.; Qi, Z.-D.; Saito, T.; Isogai, A. Nanofibrillar Chitin Aerogels as Renewable Base Catalysts. *Biomacromolecules* **2014**, *15* (11), 4314–4319. https://doi.org/10.1021/bm501320b.

(155) de Nooy, A. E. J.; Besemer, A. C.; van Bekkum, H. Highly Selective Nitroxyl Radical-Mediated Oxidation of Primary Alcohol Groups in Water-Soluble Glucans. *Carbohydr. Res.* **1995**, *269* (1), 89–98. https://doi.org/10.1016/0008-6215(94)00343-E.

(156) Harrisson, S.; Drisko, G. L.; Malmström, E.; Hult, A.; Wooley, K. L. Hybrid Rigid/Soft and Biologic/Synthetic Materials: Polymers Grafted onto Cellulose Microcrystals. *Biomacromolecules* **2011**, *12* (4), 1214–1223. https://doi.org/10.1021/bm101506j.

(157) Filpponen, I.; Argyropoulos, D. S. Regular Linking of Cellulose Nanocrystals via Click Chemistry: Synthesis and Formation of Cellulose Nanoplatelet Gels. *Biomacromolecules* **2010**, *11* (4), 1060–1066. https://doi.org/10.1021/bm1000247.

(158) Habibi, Y.; Chanzy, H.; Vignon, M. R. TEMPO-Mediated Surface Oxidation of Cellulose Whiskers. *Cellulose* **2006**, *13* (6), 679–687. https://doi.org/10.1007/s10570-006-9075-y.

(159) Demicheli, G.; Maggi, R.; Mazzacani, A.; Righi, P.; Sartori, G.; Bigi, F. Supported Organic Catalysts: Synthesis of (E)-Nitrostyrenes from Nitroalkanes and Aromatic Aldehydes over Propylamine Supported on MCM-41 Silica as a Reusable Catalyst. *Tetrahedron Lett.* **2001**, *42* (12), 2401–2403. https://doi.org/10.1016/S0040-4039(01)00156-3.

(160) Gu, J.; Catchmark, J. M.; Kaiser, E. Q.; Archibald, D. D. Quantification of Cellulose Nanowhiskers Sulfate Esterification Levels. *Carbohydr. Polym.* **2013**, *92* (2), 1809–1816. https://doi.org/10.1016/j.carbpol.2012.10.078.

(161) Nishiyama, Y.; Sugiyama, J.; Chanzy, H.; Langan, P. Crystal Structure and Hydrogen Bonding System in Cellulose Iβ from Synchrotron X-Ray and Neutron Fiber Diffraction. *J. Am. Chem. Soc.* **2003**, *125*, 14300–14306. https://doi.org/10.1021/ja0257319.

(162) Kim, K. C.; Moschetta, E. G.; Jones, C. W.; Jang, S. S. Molecular Dynamics Simulations of Aldol Condensation Catalyzed by Alkylamine-Functionalized Crystalline Silica Surfaces. *J. Am. Chem. Soc.* **2016**, *138* (24), 7664–7672. https://doi.org/10.1021/jacs.6b03309.

(163) Kandel, K.; Althaus, S. M.; Peeraphatdit, C.; Kobayashi, T.; Trewyn, B. G.; Pruski, M.; Slowing, I. I. Solvent-Induced Reversal of Activities between Two Closely Related Heterogeneous Catalysts in the Aldol Reaction. *ACS Catal.* **2013**, *3* (2), 265–271. https://doi.org/10.1021/cs300748g.

(164) Pallewela, G. N.; Smith, P. E. Preferential Solvation in Binary and Ternary Mixtures. *J. Phys. Chem. B* **2015**, *119* (51), 15706–15717. https://doi.org/10.1021/acs.jpcb.5b10139.

(165) Bagno, A. Probing the Solvation Shell of Organic Molecules by Intermolecular 1H

NOESY. *J. Phys. Org. Chem.* **2002**, *15* (12), 790–795. https://doi.org/10.1002/poc.543.

(166) Timasheff, S. N. Protein-Solvent Preferential Interactions, Protein Hydration, and the Modulation of Biochemical Reactions by Solvent Components. *Proc. Natl. Acad. Sci.* **2002**, *99* (15), 9721–9726. https://doi.org/10.1073/pnas.122225399.

(167) Humeres, E.; Mascayano, C.; Riadi, G.; González-Nilo, F. Molecular Dynamics Simulation of the Aqueous Solvation Shell of Cellulose and Xanthate Ester Derivatives. *J. Phys. Org. Chem.* **2006**, *19* (12), 896–901. https://doi.org/10.1002/poc.1074.

(168) Laage, D.; Elsaesser, T.; Hynes, J. T. Water Dynamics in the Hydration Shells of Biomolecules. *Chem. Rev.* **2017**, *117* (16), 10694–10725. https://doi.org/10.1021/acs.chemrev.6b00765.

(169) Burkinshaw, S. M. Cellulosic Fibres. In *Physico-chemical Aspects of Textile Coloration*; John Wiley & Sons, Ltd: Chichester, UK, 2015; pp 249–357. https://doi.org/10.1002/9781118725658.ch7.

(170) Ellebracht, N. C.; Jones, C. W. Optimized Cellulose Nanocrystal Organocatalysts Outperform Silica-Supported Analogues: Cooperativity, Selectivity, and Bifunctionality in Acid–Base Aldol Condensation Reactions. *ACS Catal.* **2019**, *9* (4), 3266–3277. https://doi.org/10.1021/acscatal.8b05180.

(171) List, B.; Lerner, R. A.; Barbas, C. F. Proline-Catalyzed Direct Asymmetric Aldol Reactions. *J. Am. Chem. Soc.* **2000**, *122* (10), 2395–2396. https://doi.org/10.1021/ja994280y.

(172) Dalko, P. I.; Moisan, L. Enantioselective Organocatalysis. *Angew. Chem., Int. Ed.* **2001**, *40* (20), 3726–3748. https://doi.org/10.1002/1521-3773(20011015)40:20<3726::AID-ANIE3726>3.0.CO;2-D.

(173) Renzi, P.; Bella, M. Non-Asymmetric Organocatalysis. *Chem. Commun.* **2012**, *48* (55), 6881–6896. https://doi.org/10.1039/c2cc31599h.

(174) Shylesh, S.; Hanna, D.; Gomes, J.; Canlas, C. G.; Head-Gordon, M.; Bell, A. T. The Role of Hydroxyl Group Acidity on the Activity of Silica-Supported Secondary Amines for the Self-Condensation of n-Butanal. *ChemSusChem* **2015**, *8* (3), 466–472. https://doi.org/10.1002/cssc.201402443.

(175) Liu, H.; Xu, W.; Liu, X.; Guo, Y.; Guo, Y.; Lu, G.; Wang, Y. Aldol Condensation of Furfural and Acetone on Layered Double Hydroxides. *Kinet. Catal.* **2010**, *51* (1), 75–80. https://doi.org/10.1134/S0023158410010131.

(176) Xu, W.; Liu, X.; Ren, J.; Zhang, P.; Wang, Y.; Guo, Y.; Guo, Y.; Lu, G. A Novel Mesoporous Pd/Cobalt Aluminate Bifunctional Catalyst for Aldol Condensation and Following Hydrogenation. *Catal. Commun.* **2010**, *11* (8), 721–726.

https://doi.org/10.1016/j.catcom.2010.02.002.

(177) Kikhtyanin, O.; Kelbichová, V.; Vitvarová, D.; Kubů, M.; Kubička, D. Aldol Condensation of Furfural and Acetone on Zeolites. *Catal. Today* **2014**, *227*, 154–162. https://doi.org/10.1016/j.cattod.2013.10.059.

(178) Ramos, R.; Hidalgo, J. M.; Göpel, M.; Tišler, Z.; Bertella, F.; Martínez, A.; Kikhtyanin, O.; Kubička, D. Catalytic Conversion of Furfural-Acetone Condensation Products into Bio-Derived C8 Linear Alcohols over Ni–Cu/Al-SBA-15. *Catal. Commun.* **2018**, *114*, 42–45. https://doi.org/10.1016/j.catcom.2018.06.006.

(179) Bass, J. D.; Katz, A. Thermolytic Synthesis of Imprinted Amines in Bulk Silica. *Chem. Mater.* **2003**, *15* (14), 2757–2763. https://doi.org/10.1021/cm021822t.

(180) Bass, J. D.; Solovyov, A.; Pascall, A. J.; Katz, A. Acid-Base Bifunctional and Dielectric Outer-Sphere Effects in Heterogeneous Catalysis: A Comparative Investigation of Model Primary Amine Catalysts. *J. Am. Chem. Soc.* **2006**, *128* (11), 3737–3747. https://doi.org/10.1021/ja057395c.

(181) de Assis, C. A.; Iglesias, M. C.; Bilodeau, M.; Johnson, D.; Phillips, R.; Peresin, M. S.; Bilek, E. M. T.; Rojas, O. J.; Venditti, R.; Gonzalez, R. Cellulose Micro- and Nanofibrils (CMNF) Manufacturing - Financial and Risk Assessment. *Biofuels, Bioprod. Biorefining* **2018**, *12* (2), 251–264. https://doi.org/10.1002/bbb.1835.

(182) Lee, D. W.; Ha, H.; Lee, W. K. Selective Mono-BOC Protection of Diamines. *Synth. Commun.* **2007**, *37* (5), 737–742. https://doi.org/10.1080/00397910601131403.

(183) Gomes, T. C. F.; Skaf, M. S. Cellulose-Builder: A Toolkit for Building Crystalline Structures of Cellulose. *J. Comput. Chem.* **2012**, *33* (14), 1338–1346. https://doi.org/10.1002/jcc.22959.

(184) Abitbol, T.; Palermo, A.; Moran-Mirabal, J. M.; Cranston, E. D. Fluorescent Labeling and Characterization of Cellulose Nanocrystals with Varying Charge Contents. *Biomacromolecules* **2013**, *14* (9), 3278–3284. https://doi.org/10.1021/bm400879x.

(185) Luo, J.; Semenikhin, N.; Chang, H.; Moon, R. J.; Kumar, S. Post-Sulfonation of Cellulose Nanofibrils with a One-Step Reaction to Improve Dispersibility. *Carbohydr. Polym.* **2018**, *181*, 247–255. https://doi.org/10.1016/j.carbpol.2017.10.077.

(186) Robertson, J. *Protecting Group Chemistry*; Oxford chemistry primers; Oxford University Press, 2000.

(187) Yoo, C. J.; Lee, L. C.; Jones, C. W. Probing Intramolecular versus Intermolecular CO_2 Adsorption on Amine-Grafted SBA-15. *Langmuir* **2015**, *31* (49), 13350–13360. https://doi.org/10.1021/acs.langmuir.5b03657.

(188) De Vylder, A.; Lauwaert, J.; Esquivel, D.; Poelman, D.; De Clercq, J.; Van Der Voort, P.; Thybaut, J. W. The Role of Water in the Reusability of Aminated Silica Catalysts for Aldol Reactions. *J. Catal.* **2018**, *361*, 51–61. https://doi.org/10.1016/j.jcat.2018.02.016.

(189) Akimov, Y. K. Fields of Application of Aerogels (Review). *Instruments Exp. Tech.* **2003**, *46* (3), 287–299. https://doi.org/10.1023/A:1024401803057.

(190) Deville, S.; Saiz, E.; Tomsia, A. P. Freeze Casting of Hydroxyapatite Scaffolds for Bone Tissue Engineering. *Biomaterials* **2006**, *27* (32), 5480–5489. https://doi.org/10.1016/j.biomaterials.2006.06.028.

(191) Pääkkö, M.; Vapaavuori, J.; Silvennoinen, R.; Kosonen, H.; Ankerfors, M.; Lindström, T.; Berglund, L. a.; Ikkala, O. Long and Entangled Native Cellulose I Nanofibers Allow Flexible Aerogels and Hierarchically Porous Templates for Functionalities. *Soft Matter* **2008**, *4* (Mcc), 2492. https://doi.org/10.1039/b810371b.

(192) López-Iglesias, C.; Barros, J.; Ardao, I.; Monteiro, F. J.; Alvarez-Lorenzo, C.; Gómez-Amoza, J. L.; García-González, C. A. Vancomycin-Loaded Chitosan Aerogel Particles for Chronic Wound Applications. *Carbohydr. Polym.* **2019**, *204* (March 2018), 223–231. https://doi.org/10.1016/j.carbpol.2018.10.012.

(193) Yang, X.; Shi, K.; Zhitomirsky, I.; Cranston, E. D. Cellulose Nanocrystal Aerogels as Universal 3D Lightweight Substrates for Supercapacitor Materials. *Adv. Mater.* **2015**, *27* (40), 6104–6109. https://doi.org/10.1002/adma.201502284.

(194) Sehaqui, H.; Gálvez, M. E.; Becatinni, V.; Cheng Ng, Y.; Steinfeld, A.; Zimmermann, T.; Tingaut, P. Fast and Reversible Direct CO2 Capture from Air onto All-Polymer Nanofibrillated Cellulose-Polyethylenimine Foams. *Environ. Sci. Technol.* **2015**, *49* (5), 3167–3174. https://doi.org/10.1021/es504396v.

(195) Butylina, S.; Geng, S.; Oksman, K. Properties of As-Prepared and Freeze-Dried Hydrogels Made from Poly(Vinyl Alcohol) and Cellulose Nanocrystals Using Freeze-Thaw Technique. *Eur. Polym. J.* **2016**, *81*, 386–396. https://doi.org/10.1016/j.eurpolymj.2016.06.028.

(196) Jiang, F.; Hsieh, Y. Lo. Cellulose Nanofibril Aerogels: Synergistic Improvement of Hydrophobicity, Strength, and Thermal Stability via Cross-Linking with Diisocyanate. *ACS Appl. Mater. Interfaces* **2017**, *9* (3), 2825–2834. https://doi.org/10.1021/acsami.6b13577.

(197) Chang, C.; Lue, A.; Zhang, L. Effects of Crosslinking Methods on Structure and Properties of Cellulose/PVA Hydrogels. *Macromol. Chem. Phys.* **2008**, *209* (12), 1266–1273. https://doi.org/10.1002/macp.200800161.

(198) Surapolchai, W.; Schiraldi, D. A. The Effects of Physical and Chemical Interactions in the Formation of Cellulose Aerogels. *Polym. Bull.* **2010**, *65* (9), 951–960. https://doi.org/10.1007/s00289-010-0306-x.

(199) Zhao, F.; Repo, E.; Song, Y.; Yin, D.; Hammouda, S. Ben; Chen, L.; Kalliola, S.; Tang, J.; Tam, K. C.; Sillanpää, M. Polyethylenimine-Cross-Linked Cellulose Nanocrystals for Highly Efficient Recovery of Rare Earth Elements from Water and a Mechanism Study. *Green Chem.* **2017**, *19* (20), 4816–4828. https://doi.org/10.1039/c7gc01770g.

(200) Tripathi, A.; Parsons, G. N.; Rojas, O. J.; Khan, S. A. Featherlight, Mechanically Robust Cellulose Ester Aerogels for Environmental Remediation. *ACS Omega* **2017**, *2* (8), 4297–4305. https://doi.org/10.1021/acsomega.7b00571.

(201) Wojtków, D.; Czarnecki, M. A. Effect of Temperature and Concentration on the Structure of Sec-Butyl Alcohol and Isobutyl Alcohol/Water Mixtures: Near-Infrared Spectroscopic Study. *J. Phys. Chem. A* **2006**, *110* (36), 10552–10557. https://doi.org/10.1021/jp062307b.

(202) Yoshida, K.; Yamaguchi, T.; Kovalenko, A.; Hirata, F. Structure of Tert-Butyl Alcohol-Water Mixtures Studied by the RISM Theory. *J. Phys. Chem. B* **2002**, *106* (19), 5042–5049. https://doi.org/10.1021/jp013400x.

(203) Dong, S.; Wang, L.; Gao, X.; Zhu, W.; Wang, Z.; Ma, Z.; Gao, C. Freeze Casting of Novel Porous Silicate Cement Supports Using Tert-Butyl Alcohol-Water Binary Crystals as Template: Microstructure, Strength and Permeability. *J. Memb. Sci.* **2017**, *541* (April), 143–152. https://doi.org/10.1016/j.memsci.2017.06.067.

(204) Barrett, C. J.; Chheda, J. N.; Huber, G. W.; Dumesic, J. A. Single-Reactor Process for Sequential Aldol-Condensation and Hydrogenation of Biomass-Derived Compounds in Water. *Appl. Catal. B Environ.* **2006**, *66* (1–2), 111–118. https://doi.org/10.1016/j.apcatb.2006.03.001.

(205) West, R. M.; Liu, Z. Y.; Peter, M.; Dumesic, J. A. Liquid Alkanes with Targeted Molecular Weights from Biomass-Derived Carbohydrates. *ChemSusChem* **2008**, *1* (5), 417–424. https://doi.org/10.1002/cssc.200800001.

(206) Alonso, D. M.; Bond, J. Q.; Dumesic, J. A.; Chheda, J. N.; Huber, G. W.; Dumesic, J. A.; Climent, M. J.; Corma, A.; Iborra, S.; Domine, M. E.; et al. Production of Liquid Alkanes by Aqueous-Phase Processing of Biomass-Derived Carbohydrates. *Catal. Today* **2011**, *147* (2), 7164–7183. https://doi.org/10.1039/C3GC41492B.

(207) Bond, J. Q.; Alonso, D. M.; Wang, D.; West, R. M.; Dumesic, J. A. Integrated Catalytic Conversion of γ-Valerolactone to Liquid Alkenes for Transportation Fuels. *Science (80-.).* **2010**, *327* (5969), 1110–1114. https://doi.org/10.1126/science.1184362.

(208) Bond, J. Q.; Wang, D.; Alonso, D. M.; Dumesic, J. A. Interconversion between Gamma-Valerolactone and Pentenoic Acid Combined with Decarboxylation to Form Butene over Silica/Alumina. *J. Catal.* **2011**, *281* (2), 290–299. https://doi.org/10.1016/j.jcat.2011.05.011.

(209) Jackson, E.; Correa, S.; Betancor, L. Cellulose-Based Nanosupports for Enzyme Immobilization; Mondal, M. I. H., Ed.; Springer International Publishing: Cham, 2019; pp 1235–1253. https://doi.org/10.1007/978-3-319-77830-3_42.

(210) Teeri, T. T.; Linder, M. The Roles and Function of Cellulose-Binding Domains. *J. Biotechnol.* **1997**, *57*, 15–28.

(211) Ong, E. Enzyme Immobilization Using the Cellulose-Binding Domain of the Cellulomonas Fimi Exoglucanase. **1992**, *7* (June), 604–607.

(212) Jesionowski, T.; Zdarta, J.; Krajewska, B. Enzyme Immobilization by Adsorption: A Review. *Adsorption* **2014**, *20* (5–6), 801–821. https://doi.org/10.1007/s10450-014-9623-y.

(213) Krajewska, B. Application of Chitin- and Chitosan-Based Materials for Enzyme Immobilizations: A Review. *Enzyme Microb. Technol.* **2004**, *35* (2–3), 126–139. https://doi.org/10.1016/j.enzmictec.2003.12.013.

(214) Orsolini, P.; Antonini, C.; Stojanovic, A.; Malfait, W. J.; Caseri, W. R.; Zimmermann, T. Superhydrophobicity of Nanofibrillated Cellulose Materials through Polysiloxane Nanofilaments. *Cellulose* **2018**, *25* (2), 1127–1146. https://doi.org/10.1007/s10570-017-1636-8.

(215) Matsumoto, M.; Kitaoka, T. Ultraselective Gas Separation by Nanoporous Metal-Organic Frameworks Embedded in Gas-Barrier Nanocellulose Films. *Adv. Mater.* **2016**, *28* (9), 1765–1769. https://doi.org/10.1002/adma.201504784.

(216) Zhang, Y.; Feng, X.; Yuan, S.; Zhou, J.; Wang, B. Challenges and Recent Advances in MOF-Polymer Composite Membranes for Gas Separation. *Inorg. Chem. Front.* **2016**, *3* (7), 896–909. https://doi.org/10.1039/c6qi00042h.

(217) McDonald, T. M.; Lee, W. R.; Mason, J. A.; Wiers, B. M.; Hong, C. S.; Long, J. R. Capture of Carbon Dioxide from Air and Flue Gas in the Alkylamine-Appended Metal-Organic Framework Mmen-Mg 2(Dobpdc). *J. Am. Chem. Soc.* **2012**, *134* (16), 7056–7065. https://doi.org/10.1021/ja300034j.

(218) Darunte, L. A.; Terada, Y.; Murdock, C. R.; Walton, K. S.; Sholl, D. S.; Jones, C. W. Monolith-Supported Amine-Functionalized Mg2(Dobpdc) Adsorbents for CO2 Capture. *ACS Appl. Mater. Interfaces* **2017**, *9* (20), 17042–17050. https://doi.org/10.1021/acsami.7b02035.

(219) Ternan, M. The Diffusion of Liquids in Pores. *Can. J. Chem. Eng.* **1987**, *65* (2), 244–249. https://doi.org/10.1002/cjce.5450650208.

(220) Sievers, C.; Scott, S. L.; Noda, Y.; Qi, L.; Albuquerque, E. M.; Rioux, R. M. Phenomena Affecting Catalytic Reactions at Solid−Liquid Interfaces. *ACS Catal.* **2016**, *6* (12). https://doi.org/10.1021/acscatal.6b02532.